Recent advances in hot tearing during casting of aluminium alloys

Li, Yue; Li, Hongxiang; Katgerman, Laurens; Du, Qiang; Zhang, Jishan; Zhuang, Linzhong

DOI
10.1016/j.pmatsci.2020.100741

Publication date
2021

Document Version
Final published version

Published in
Progress in Materials Science

Citation (APA)
Li, Y., Li, H., Katgerman, L., Du, Q., Zhang, J., & Zhuang, L. (2021). Recent advances in hot tearing during casting of aluminium alloys. *Progress in Materials Science*, *117*, Article 100741. https://doi.org/10.1016/j.pmatsci.2020.100741

Progress in Materials Science 117 (2021) 100741

Contents lists available at ScienceDirect

Progress in Materials Science

journal homepage: www.elsevier.com/locate/pmatsci

Recent advances in hot tearing during casting of aluminium alloys

Yue Li [a], Hongxiang Li [a,*], Laurens Katgerman [b], Qiang Du [c,*], Jishan Zhang [a], Linzhong Zhuang [a,*]

[a] State Key Laboratory for Advanced Metals and Materials, University of Science and Technology Beijing, 100083 Beijing, China
[b] Department of Materials Science and Engineering, Delft University of Technology, Mekelweg 2, 2628CD Delft, the Netherlands
[c] SINTEF Industry, 0314 Oslo, Norway

ARTICLE INFO

Keywords:
Aluminium alloys
Hot tearing
Casting
Mushy zone
Compositions
Process parameters

ABSTRACT

Hot tearing is one of the most severe and irreversible casting defects for many metallic materials. In 2004, Eskin et al. published a review paper in which the development of hot tearing of aluminium alloys was evaluated (Eskin and Suyitno, 2004). Sixteen years have passed and this domain has undergone considerable development. Nevertheless, an updated systematic description of this field has not been presented. Therefore, this article presents the latest research status of the hot tearing during the casting of aluminium alloys. The first part explains the hot tearing phenomenon and its occurrence mechanism. The second part presents a detailed description and analysis of the characterisation methods of the mushy zone mechanical properties and hot tearing susceptibility. The third part presents considerable data pertaining to the mushy zone behaviour, including those of the linear contraction and load behaviour during solidification, semi-solid strength and ductility, and characteristic points related to hot tearing. The fourth part examines the effect of the composition and casting process parameters on the hot tearing susceptibility of aluminium alloys. The fifth part describes the hot tearing simulations and the associated criteria and mechanisms. Finally, recommendations for the further development of hot tearing research are presented.

1. Introduction

1.1. The casting of aluminium alloys

Aluminium alloys, as one of the most promising metallic materials second only to steel for modern societies, are being widely used in many applications such as food packaging, transportation, construction, aerospace, and aircraft owing to their abundance and unique material properties [1–3]. In recent decades, the production of aluminium alloys has increased considerably. From 2000 to 2019, the annual production of aluminium alloys worldwide increased steadily from approximately 25 to 65 million tons [4]. In general, aluminium alloys can be divided into cast and wrought aluminium alloys. The wrought aluminium alloys can be further subdivided into heat-treatable (such as the 2xxx, 6xxx, and 7xxx series) and non-heat-treatable aluminium alloys (such as the 1xxx, 3xxx, and 5xxx series), the mechanical properties of which can be enhanced by various heat-treatment processes and work hardening, respectively [5,6].

* Corresponding authors.
E-mail addresses: hongxiang_li@vip.163.com (H. Li), qiang.du@sintef.no (Q. Du), linzhongzhuang@yahoo.com (L. Zhuang).

https://doi.org/10.1016/j.pmatsci.2020.100741
Received 2 January 2020; Received in revised form 16 September 2020; Accepted 16 September 2020
Available online 22 September 2020

Nomenclature and Acronyms

2D	Two-dimensional
3D	Three-dimensional
AE	Acoustic emission
AM	Additive manufacturing
BTR	Brittle temperature range
CHT rig	Cast hot tearing rig
CRC mould	Constrained-rod casting mould
DC casting	Direct chill casting
HCS	Hot cracking susceptibility
HIP	Hot-isostatic-pressing
HTS	Hot tearing susceptibility
LFEC	Low-frequency electromagnetic casting
LVDT	Linear variable differential transformer
NES	Non-equilibrium solidus
OM	Optical microscope
RDG criterion	Rappaz-Drezet-Gremaud criterion
Ref./Refs.	Reference/References
SDAS	Secondary dendrite arm spacing
SEM	Scanning electron microscope
SKK criterion	Suyitno-Kool-Katgerman criterion
TCC	Thermal contraction coefficient
TEM	Transmission electron microscopy
UST	Ultrasonic treatment
UTS	Ultimate tensile strength
XRD	X-ray diffraction
ZDT	Zero ductility temperature
ZST	Zero strength temperature

The casting of aluminium alloys is generally carried out by shape casting methods or DC casting. The two casting technologies share many fundamental theories pertaining to solidification, macroscopic heat transfer, flow, deformation analysis, and furnace/casting equipment design and operations. Shape casting can be further divided into sand casting, permanent mould casting, die-casting, investment casting (lost-foam, lost-wax), and so on. DC casting, which is currently the main commercial technology to produce wrought

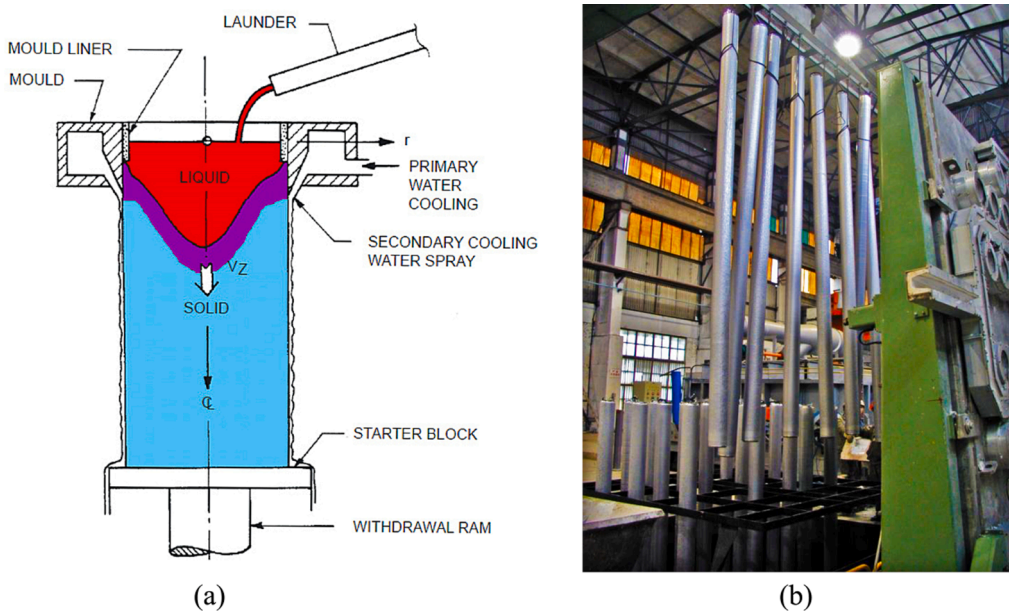

Fig. 1.1. Vertical DC casting process: (a) schematic of a DC caster [8] and (b) an example of DC-cast billets.

alloys in the form of extrusion billets and rolling slabs, can be classified into vertical and horizontal DC castings. At present, vertical DC casting has become the backbone to produce wrought aluminium alloys. The schematic of this process is shown in Fig. 1.1(a). First, raw materials are melted in a furnace. Subsequently, the melt is poured via a launder into a water-cooled mould (primary cooling) onto a starter block, which is initially at rest. When the mould is filled and a sufficiently strong solid shell is formed, the block is moved downwards at a certain casting speed, V_z. When the solidified metal exits the mould, it is directly sprayed and chilled by water jets, in a process known as secondary cooling. The process is continued until the desired sample length is achieved. Finally, the DC-cast billets are removed from the casting machine for subsequent processing, as shown in Fig. 1.1(b). The wide use of DC casting can be attributed to its high productivity and casting quality [7,8], and this technology has undergone rapid advancement with the widespread application of wrought aluminium alloys. In recent times, the AM technology specific to aluminium alloys has undergone rapid development to satisfy the industrial requirements, due to its unmatched capabilities [9]. The cooling rates associated with AM (10^4–10^6 K/s as reported in Ref. [10]) are considerably steeper than those related to casting, and thus, solidification defects such as porosities/hot tears/distortion are often generated in the AM process, especially when printing wrought aluminium alloys [11–13]. Nevertheless, certain basic concepts of solidification and hot tearing for AM and casting processes are consistent, and thus, the authors discuss several state-of-the-art studies pertaining to the hot tearing related to AM in the later sections.

1.2. Solidification behaviour

Different from pure metals, in which solidification occurs at one temperature, alloys exhibit certain solidification ranges depending on the alloy compositions and processing parameters. In other words, over a certain temperature interval, the solid and liquid phases co-exist (in a form known as a semi-solid state). As shown in Fig. 1.2, a semi-solid material generally undergoes a transition from the slurry to mush during solidification. In the slurry zone, several floating solidified particles/phases exist in the liquid phases. At this time, continuous solid skeletons have not been generated yet, and liquid feeding occurs without any resistance. During the subsequent solidification, the solid grains start to contact each other, and the corresponding temperature is termed as the coherency point (25–40% solid). Subsequently, a continuous solid network, which can transfer forces, is gradually generated, and liquid feeding becomes more and more difficult. This material has a mushy structure. The transition point is known as the rigidity point [14,15]. The rigidity point can be regarded as the upper boundary of the “effective solidification range” or “vulnerable part of the solidification interval” [14]. The lower boundary is the equilibrium or non-equilibrium solidus depending on the solidification conditions.

The slurry and mushy structures exhibit significantly different thermomechanical behaviours. The slurry structure is generally represented by viscosity-based constitutive models [16,17], derived through fluid dynamics concepts and modified to consider the suspending solid particles. In comparison, describing the constitutive behaviour of the mushy structure is more challenging. Various models have been proposed to this end, including modified creep law models [18,19], elastic-viscoplastic models [20,21], and three-phase microstructure model [22], as discussed in Section 5.1.1.

According to the permeability of the solid network, the solidification process can be divided into four phases [7,15,23–25]. The initial phase is known as “*mass feeding*”, in which the formed dendrites do not contact one another and the rigidity point has not been reached. The semi-solid material is considered to have a slurry structure. The subsequent phase is known as “*interdendritic feeding*”. As the mushy structure is established, a rigidity network begins to form through which the liquid flows. At this time, the permeability of the mushy structure is sufficient to prevent the formation of pores. During further solidification, the dendrite arms connect, and the

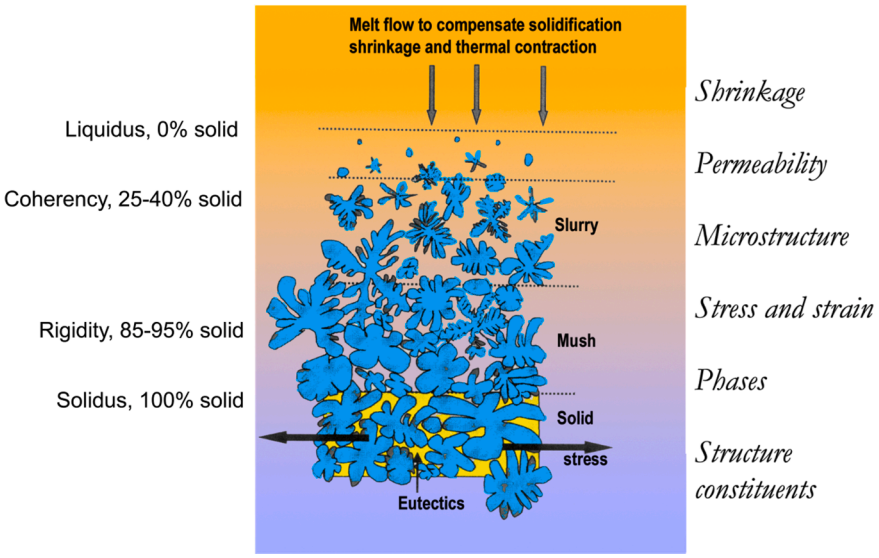

Fig. 1.2. Solidification behaviour: characteristic points in the solidification range (left) and critical factors related to hot tearing (right) (the original sketch comes from Ref. [23]).

liquid phases are entrapped or immobilised through surface tension. This phase is known as "*interdendritic separation*". At this point, the permeability of the mushy structure is extremely low, and micro-pores or hot tears may occur if the solidification shrinkage and thermal stresses are sufficiently large. Finally, the "*interdendritic bridging or solid feeding*" phase occurs in which only the entrapped liquid phases exist and the semi-solid material exhibits a considerable strength and certain ductility. In this stage, solid phase creep is the only mechanism to accommodate the solidification shrinkage and thermal stresses. In the first two stages, the semi-solid material exhibits a sufficient feeding ability to avoid the generation of pores or hot tears. Consequently, it is crucial to focus on the latter two stages in which micro-pores and hot tears can likely be generated, as discussed in Section 5.2.2.

1.3. Hot tearing

During solidification, various defects may occur due to several internal and external factors. One of the most severe and unrecoverable defects is hot tearing (also known as hot cracking or hot shortness). Hot tears are generated above the solidus or NES depending on the solidification conditions and propagate along the grain boundaries. Consequently, an uneven fracture surface is generated, covered with a layer of liquid (Fig. 1.3(a)), or, in certain cases, with solid bridges connecting the two sides of the hot tears (Fig. 1.3(b)) [26,27]. The type of fracture surface is closely related to the alloying contents [7,27]. As shown in Fig. 1.3, the Al-1 wt% Cu alloy exhibits a certain eutectic characteristic, and its surface is dominated by the fractured solid bridges; in contrast, the Al-3 wt% Cu alloy exhibits notable eutectic characteristics and its fracture surface is completely covered with the solidified eutectic liquid. Therefore, the complex fracture behaviour must be considered in an ideal hot tearing criterion, as described in Section 5.

The main factors pertaining to the occurrence of hot tearing are presented in Fig. 1.2. First, the permeability of the solid network decreases as solidification proceeds; in this scenario, the liquid feeding is not sufficient to realise the healing of micro-pores, which later transform into cracks. In general, the distribution of liquid films relies on the dihedral wetting angle, θ [15]. At a low angle, the liquid films spread and cover the grain boundaries as much as possible. In contrast, at a high wetting angle, the liquid films are concentrated on the triple grain boundary points and solid bridges may occur. The occurrence of solidification shrinkage and thermal contraction due to the uneven thermal gradients can impose stresses and strains on the semi-solid network, which is another key factor for the occurrence of hot tearing. Finally, the microstructure development and precipitation of secondary phases during solidification can influence the hot tearing susceptibility of the material [28,29].

So far, many studies have been performed to investigate hot tearing behaviour, which has been reviewed by Novikov [30], Sigworth [31], Lin [32,33], Eskin et al. [7,15], and Li et al. [31]. However, sixteen years have passed since the last detailed review on hot tearing was published by Eskin et al. [15]. Therefore, it is necessary to review the state-of-the-art pertaining to the hot tearing of aluminium alloys during casting. The first notable development corresponds to the improvement of the hot tearing devices and characterisation techniques to measure the hot tearing susceptibility. The mechanical behaviour of the mushy zone related to hot tearing has been better quantified and the internal mechanism of the initiation and propagation of hot tearing has been explored. Second, over these years, considerable mechanical data of the mushy zone related to hot tearing have been obtained, such as those pertaining to the linear solidification contraction, load behaviour during solidification, and semi-solid strength and ductility of various

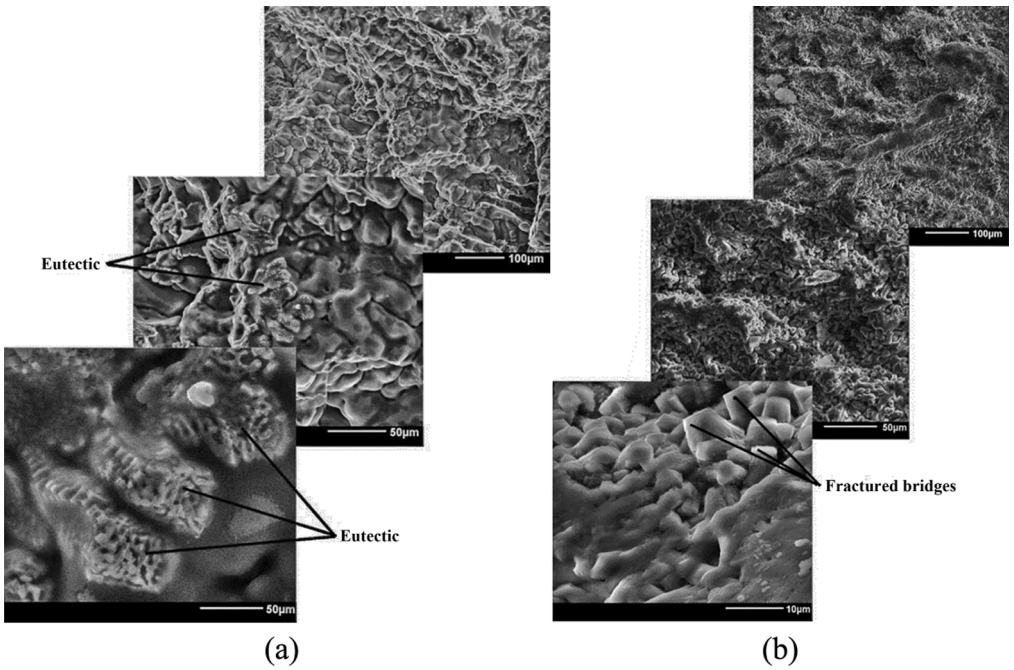

Fig. 1.3. Fracture surfaces in DC-casting (a) Al-3 wt% Cu and (b) Al-1 wt% Cu alloys [27].

aluminium alloys. Third, the effect of the composition and process parameters on the hot tearing susceptibility of aluminium alloys during different casting processes must be further summarised and analysed based on the review paper published by Eskin et al. [15] in 2004. Fourth, the research front on hot tearing simulations and hot tearing criteria have been pushed forward, and thus a corresponding review on these aspects is necessary. In particular, the future research directions pertaining to hot tearing must be specified based on the latest developments on hot tearing and the state-of-the-art materials informatics.

2. Methods to characterise the mechanical properties of the mushy zone and hot tearing susceptibility

2.1. Methods to characterise the mechanical properties of the mushy zone

The mechanical properties of the mushy zone refer to the ability to retain shape and transfer forces, which are critical to build the constitutive equations of semi-solid materials and investigate hot tearing. It is accepted that the solidified grains are surrounded by liquid films during the late stage of solidification, and consequently, the semi-solid materials exhibit quite low strength and ductility. As a result, conventional mechanical testing machines cannot be directly applied to measure these properties. In recent decades, there have been numerous attempts to measure the mushy zone mechanical properties of metallic alloys. Essentially, three types of mechanical tests have been developed: tension, compression, and shear. Among the three types of tests, tensile testing is the most widely used approach in the context of hot tearing. The history and development of semi-solid tensile tests before 2004 have been reviewed by Eskin et al. [15]. Here we primarily focus on the developments after 2004. The semi-solid tensile tests can be divided into two categories: tensile tests upon reheating and upon solidification [15,34]. Fig. 2.1 provides an outline of these testing techniques highlighting the associated capabilities and limitations, as discussed in Sections 2.1.1 and 2.1.2.

2.1.1. Tensile tests upon reheating

In general, the UTS (or maximum stresses) and elongation to fracture (or diametric change) are two major focuses for semi-solid tensile tests. To date, several types of tensile testers, e.g., Gleeble series thermo-mechanical simulators (1500, 3500, or 3800) and Instron series tensile test machines have been applied to measure the semi-solid mechanical properties of aluminium alloys [8,20,21,34–43]. A typical Gleeble series tester is shown in Fig. 2.2. The advantages of the Gleeble series simulator are the use of the Joule heat to rapid melt the sample and the use of advanced stress-strain and temperature acquisition and control systems [15]. The

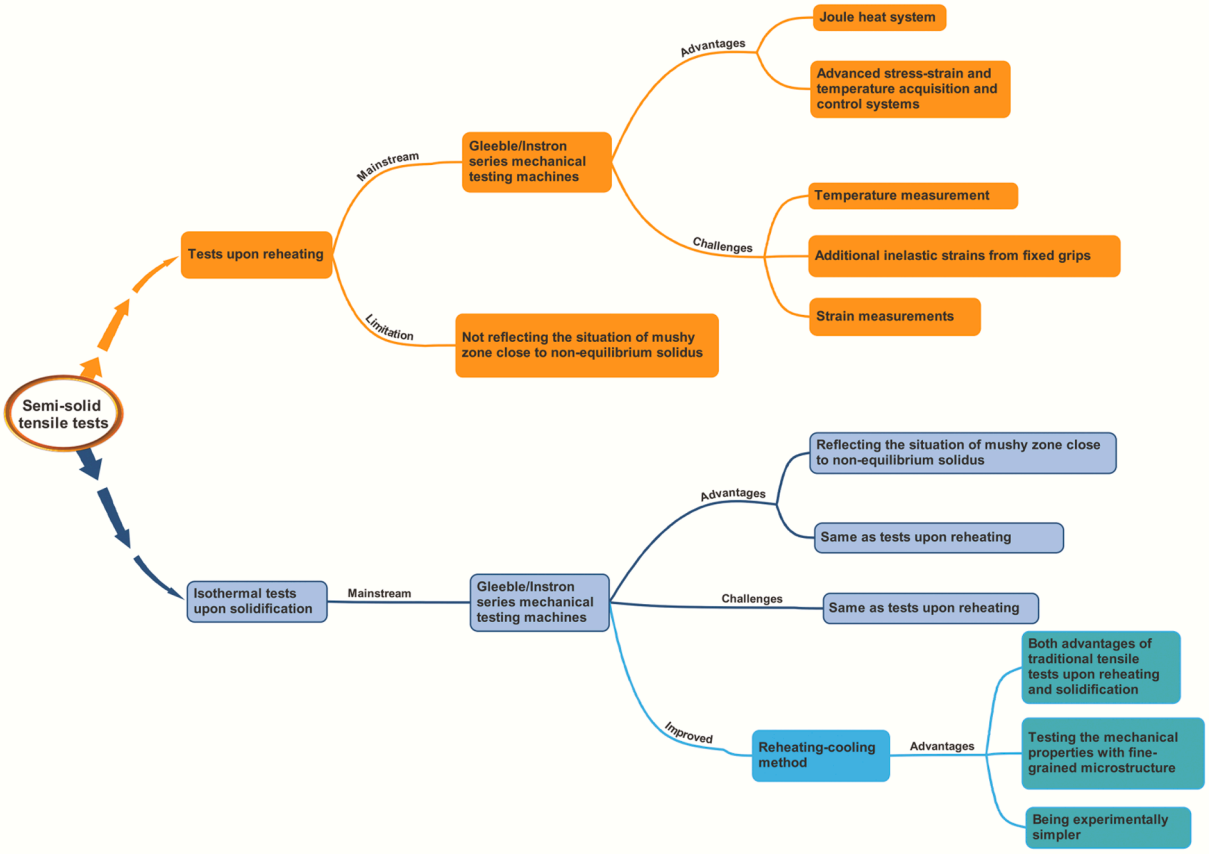

Fig. 2.1. An outline of semi-solid tensile tests.

general testing procedure is as follows [34,36,41]: first, the central part of the sample is heated to the desired temperature according to the scheduled thermal cycle and maintained at this temperature for a certain duration. Subsequently, a constant strain rate is applied. After the specimen fractures completely, the two halves of the specimen are allowed to cool to room temperature and the fracture surfaces are examined.

To conduct reliable semi-solid tensile tests, several problems should be addressed, as shown in Fig. 2.1. First, a suitable thermal control must be realised, as small changes in the temperature or solid fraction can considerably influence the mechanical properties. The radial temperature gradient in the testing zone can often be eliminated by reducing the cross-section of the samples, while it is impossible for the axial gradient which needs to be controlled to make it symmetric and as low as possible [34,36,41,42]. Surface-welded thermocouples are often used because embedded thermocouples can induce defects and affect the measured properties [40,42]. In certain cases, the weld between the thermocouple and specimen may fail at high liquid fractions. Second, the employed fixed steel grips (Fig. 2.2(b)) may generate compressive stresses due to the thermal expansion during heating. This will result in an accumulation of the inelastic strains [40,42]. Third, because the temperature gradient along the axial direction cannot be eliminated, the use of the longitudinal strain measurements may lead to a certain elongation, which is the average value based on a range of temperatures instead of a specific value at a specific temperature. Therefore, instead of the longitudinal strain characterisations [34,41,44], it is preferable to obtain diametric strain measurements [18,39,40,42] to characterise the semi-solid ductility. The diametric strain ε can be expressed as follows [18,42]:

$$\varepsilon = -2\ln(D/D_0) \tag{2.1}$$

where D_0 is the initial diameter of the specimen and D is the instantaneous diameter. Note that a dilatometer cannot be used because the compressive stress caused by the dilatometer jaws may be larger than the compressive strength of the material, thereby generating inelastic strains. A failure to address one or more of these challenges can lead to reproducibility problems. For example, at a strain rate of 10^{-4}, the UTS of semi-solid AA5182 was measured to be 9 MPa at 560 °C by Colley et al. [42]; the corresponding value measured by van Haaften et al. [18] at a similar strain rate was 3 MPa.

To address the first challenge, a methodology called the "2TC technique" is often employed [40,43,45,46]. In this approach, thermal control is realised using two thermocouples, as shown in Fig. 2.3. The process flow is as follows. In the first stage, the specimen is rapidly heated until the reading of the first thermocouple (TC#1, in the centre of the gauge region) is 400 °C. In the second stage, the temperature of the sample is controlled using the second thermocouple (TC#2, just outside the gauge region) and increases gradually. The difference in the temperature indicated by the two thermocouples, ΔT, is constantly recorded during the second stage. A linear relationship for ΔT as a function of the temperature at TC#2 is established and continually refined until TC#1 does not work. The temperature of the sample is increased until $T_{TC\#2} + \Delta T$is equal to the testing temperature. In this manner, the first problem can be overcome. Another approach is to use a high-temperature adhesive to avoid the detachment of the thermocouple from the sample [37,41,42]. The measurement approach to address the second issue is shown in Fig. 2.3 [40]. The deformation control can be improved by adjusting the fixed grip carefully to offset the thermal expansion. After a 30 s hold at the test temperature to ensure thermal stability, the fixed grip is displaced at a rate of 50 μm/s, in increments of 25 μm. After each increment, the force is recorded. If the force is 15 N or larger, it is considered that the fixed grip is aligned with the end of the sample. In this manner, the second problem can be overcome. To address the third challenge, a laser dilatometer or a high-resolution digital video camera can be used to measure the diametric change [39,40,42]. The real semi-solid ductility may be underestimated because the use of a diameter measurement for strain does not consider the occurrence of internal defects, which could have accumulated within the sample. Phillion et al. [47] highlighted that this internal damage could be as large as 50% for a sample at very high solid fractions. The internal damage can be imaged and measured using the synchrotron X-ray micro tomography technique (Section 2.2.2).

The reheating method is reasonably reliable when the mushy zone is close to the equilibrium state; however, the method exhibits

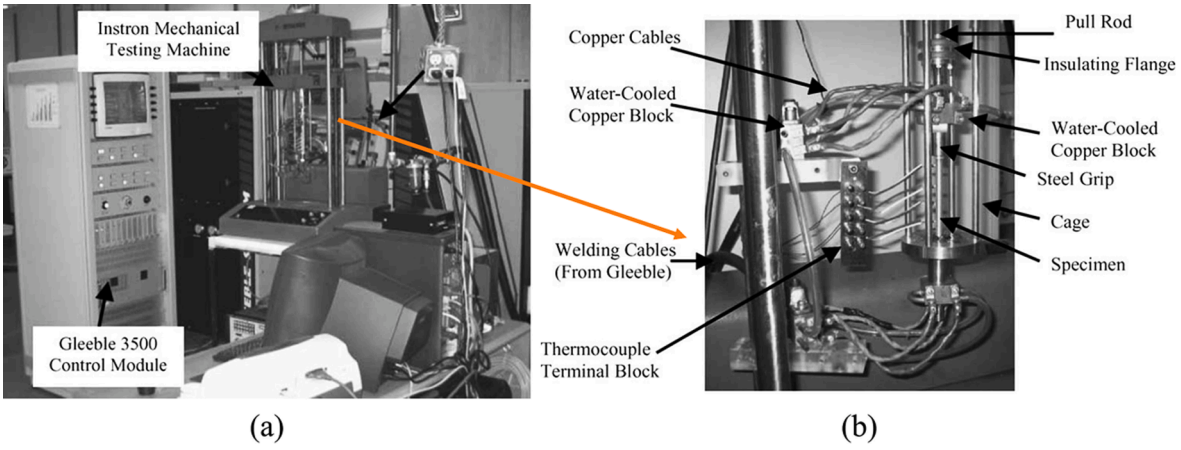

Fig. 2.2. (a) Example of a Gleeble 3500 thermo-mechanical testing machine for semi-solid tensile tests; (b) details of the tensile unit [42].

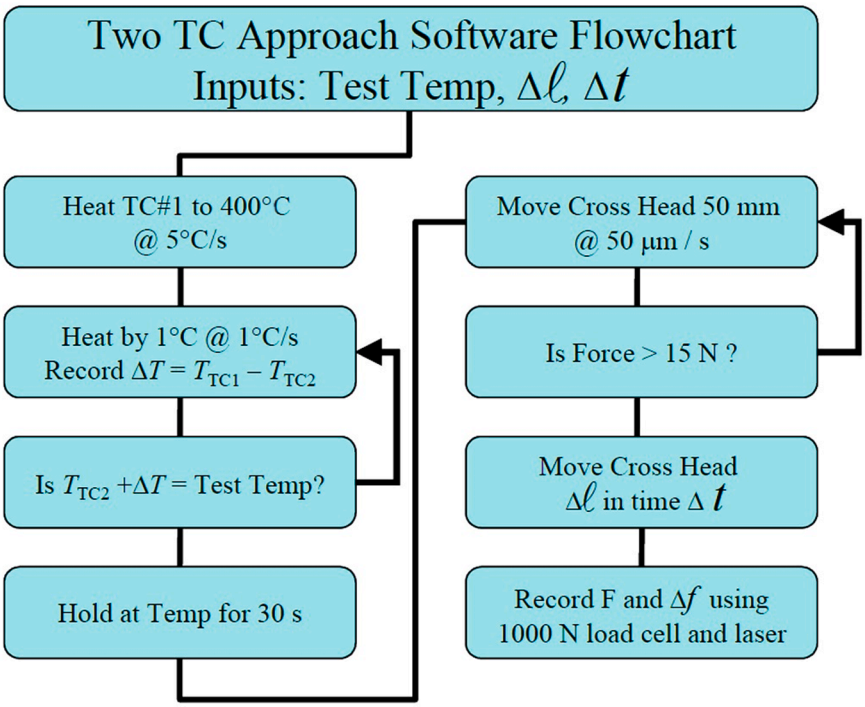

Fig. 2.3. Flowchart outlining the "2TC technique" for performing the semi-solid tensile test in the Gleeble 3500 thermo-mechanical simulator [40].

certain limitations when the mushy zone is in a non-equilibrium state and the solid fraction of the mushy zone is high. At high temperatures, the solid-state diffusion is fast close to the non-equilibrium solidus and the homogenization could dissolve the non-equilibrium phases, resulting in a decrease in the liquid fraction [42]. Unfortunately, the mushy zone in an alloy is often not in equilibrium as in the case of DC casting, and hot tearing occurs at high solid fractions (more than 0.9). During the heating and holding stages, the liquid fraction of the mushy zone in the sample decreases with time due to the back diffusion into the solid phase [43]. The liquid may completely vanish in the case of a small amount of liquid and a sufficiently large heating and holding time. Moreover, the grain size and morphology may change significantly at high temperatures. These variations in the semi-solid microstructure will make the measured mechanical properties far deviate from the real values of DC-cast samples. Thus, the reheating method is not sufficiently reliable to investigate the mechanical properties of semi-solid alloys with respect to DC casting. To be representative, the tensile test must be performed upon solidification.

2.1.2. Tensile tests upon solidification

Great efforts have been made by scientists to develop the isothermal tensile testing technique upon solidification of aluminium alloys [15]. Currently, the most common way to conduct isothermal tensile tests upon solidification is to use the modified Instron mechanical testing machine connected to a Gleeble series thermo-mechanical simulator (Fig. 2.2) due to the same advantages as the tests upon reheating (Fig. 2.1). In contrast to the tests upon reheating, this method involves cooling a specimen from the liquid state to a certain temperature above the non-equilibrium solidus at a certain cooling rate. The general procedure is as follows [8,20,21,34,41,43]: the sample is heated at a certain heating rate until the centre of the sample is completely melted in a mould, which is coated to avoid the flow of liquid. Subsequently, the melt is cooled at a certain cooling rate until the desired testing temperature is reached. After being maintained at this temperature for a short time to establish a homogeneous temperature field in the melted part, a tensile test is conducted at a certain strain rate. Stress-strain curves are recorded by the module of the Gleeble device. Note that the same three issues encountered in the tensile tests upon reheating also occur in the isothermal tensile tests upon solidification (Fig. 2.1) and the above-mentioned solutions are equally applicable.

The isothermal tensile tests upon solidification can measure the mechanical properties of the samples in a non-equilibrium state, but the measurement accuracy is affected by the interactions between the sample and mould and the non-uniform temperature distribution in the sample. Although the measurement accuracy can be increased by slowly solidifying the melt to the testing temperature, coarse grains may be formed in this process. This type of testing may lead to the underestimation of the mechanical properties of a DC-casting-produced sample with a fine-grained microstructure. Han et al. [43] proposed a reheating-cooling method to overcome this problem. It consists of a reheating stage where the alloy is heated above the equilibrium solidus to partially remelt (the heating rate is high enough to minimise the back diffusion in the solid phase), and a cooling stage where the grains grow back to their original size and even recover the solute redistribution produced during solidification. This method has both the advantages of the traditional tensile tests upon reheating and solidification and is suitable to test the mushy-zone mechanical properties of fine-grained castings, such as

those produced by DC casting. Compared to the traditional tensile tests upon solidification, this method is experimentally easier to be performed. All these advantages demonstrate the potential of this approach to measure the mushy-zone mechanical properties with respect to DC casting.

Nevertheless, the determination of the mushy-zone mechanical properties of AM aluminium alloys has not been extensively investigated until now. When performing semi-solid tensile tests for AM, a high cooling rate (10^4-10^6 K/s [10]) must be simulated owing to its potential significant influence on the measured semi-solid mechanical properties (Section 3.3.1.3). Moreover, the material state (such as powder form) and complex thermal history must also be considered. Fabrègue et al. [41] reported a tensile test upon solidification with a cooling rate of 70 K/s satisfied during welding. However, this cooling rate is considerably smaller than that required in AM and more efforts should be made to develop suitable semi-solid tensile testing methods for AM processes.

Considering Fig. 2.1, it can be concluded that tensile tests upon solidification, especially the reheating-cooling method, can reproduce the situations of the mushy zone close to the non-equilibrium solidus, and are more suitable for determining the mushy zone mechanical properties of DC-cast aluminium alloys compared to those upon reheating. The latter is more suitable for a casting process that involves near-equilibrium solidification, such as sand casting. Using the improved testing technique based on the Gleeble or Instron series mechanical measurements, a considerable amount of experimental data has been attained through the two tensile testing methods. This information is valuable in developing the constitutive models of semi-solid materials and hot tearing predictions and is summarised in Section 3.3. It should be emphasized that such data must be used with careful consideration of the type of casting method; otherwise, incorrect hot tearing predictions may be generated.

2.2. *Methods to characterise the hot tearing susceptibility*

Apart from measuring the pure mechanical properties of semi-solid materials, various sophisticated devices have been designed to evaluate the hot tearing susceptibility of different aluminium alloys with the final goal to determine whether a hot tear will occur or not. The initial research activities, which were focused on rating the hot tearing susceptibility of aluminium alloys, were conducted primarily using shape mould methods. Many of the designed approaches, regardless of their complexity, were developed considering that the locations of occurrence of hot tearing were similar to those in real shape-mould casting applications. Such approaches included the ring mould test [48], CRC mould test [49–53], cylindrical bar casting test [32], ball-bar casting test [32], and “U” shape casting test [32]. These post-mortem tests for shape casting have been reviewed by Lin [32], Eskin et al. [15], and Li et al. [31], and the interested readers may refer to these references for details. With the progress of the DC casting technology, the prevention of hot tearing during DC casting has become increasingly crucial in commercial aluminium alloys, especially for 2XXX and 7XXX alloys. Indeed, industrial trials or small-scale DC casting experiments are the most direct methods to evaluate the hot tearing behaviour [54,55]. However, such methods are time-consuming and costly. In contrast, the use of dedicated hot tearing testing devices can save considerable time and effort, and each influencing factor can be isolated to be investigated. The existing post-mortem tests in shape casting deviated from the DC casting conditions, and the obtained data could not be applied to the DC casting practices (see Section 4.1). Therefore, in recent

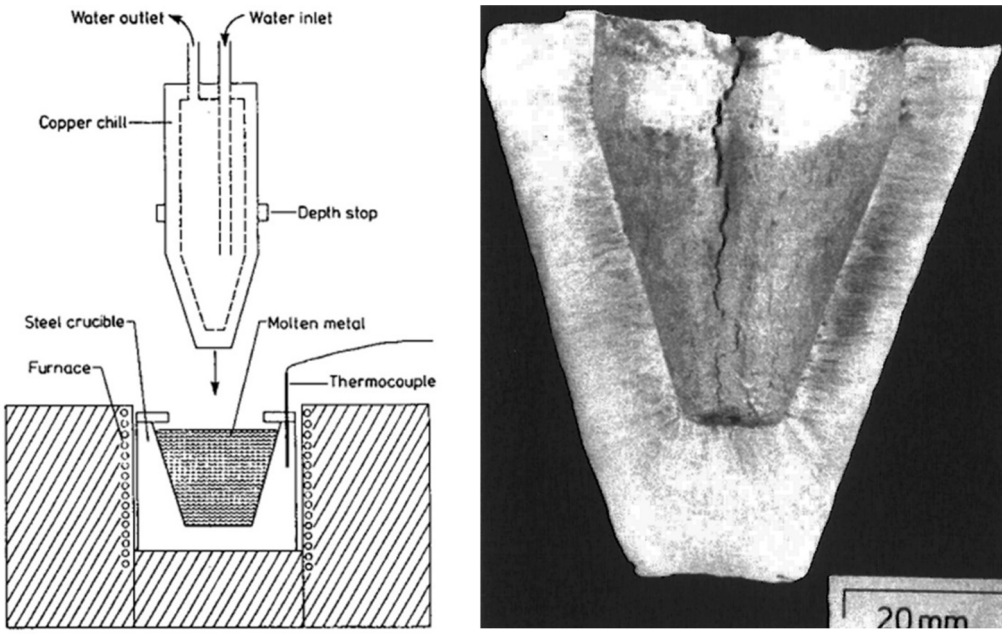

Fig. 2.4. Schematic of a “cold finger” mould and the corresponding casting [56,57].

years, a series of devices simulating the DC casting conditions were designed to evaluate the hot tearing susceptibility of different aluminium alloys.

2.2.1. Dedicated hot tearing tests simulating DC casting

Warrington and McCartney [56,57] designed a "cold finger" mould to study the hot tearing problem in the shell zone during DC casting. This device consists of a water-cooled tapered copper chill and a tapered steel crucible placed in an open furnace (Fig. 2.4(a)). The taper angle of both the copper chill and steel crucible is 17.5°. The diameters of the copper chill and steel crucible are chosen such that the solidified sample has a thickness of 10 mm. The test procedure is as follows: the melt is kept in the crucible and held at a certain temperature. Subsequently, the copper chill (cold finger) is inserted into the crucible to the desired depth. Solidification occurs along a direction perpendicular to the surface of the copper chill. As shown in Fig. 2.4(b), a hot tear is first generated at the top of the casting since it has the largest diameter, which stands the highest tensile stress. At this instance, the hot tear develops downward and finally stops. When the casting completely solidifies, the sample is removed, and the crack length is measured. The hot tearing susceptibility is rated according to the maximum length of the hot tears. The advantages and disadvantages of this device are summarised in Fig. 2.5. First, this technique can be used for both low and high hot-tearing-susceptible alloys, such as Al-Cu (0.5–2.0 wt%) [56], AA7010 and AA7050 alloys with columnar or equiaxed structures [57]. Using the device, the temperatures of the copper chill and the aluminium melt can be controlled with a high precision, which allows the realisation of a controllable cooling rate. However, the development of hot tears cannot be visualised, and the quantitative load/displacement information is not provided.

Subsequently, a dog-bone-shaped rectangular mould was designed to simulate the situation of DC-cast billets, as shown in Fig. 2.6 (a) [58]. In this mould, a hot spot was generated at the centre of the casting, and the axial contraction was constrained. The stresses developed at the hot spot likely resulted in hot tearing. The two ends of the mould were cooled using water or air, and the mould could be preheated to a certain temperature to allow the establishment of different thermal stress fields. A liquid feeder was applied to reproduce more realistic DC casting conditions (Fig. 2.6(b)). The casting was examined after complete solidification. Usually, the visible surface crack length was considered as a measurement for the hot tearing susceptibility [49,59]; however, this approach was not effective because the presence of subsurface cracks was not considered. Clyne and Davies [60] combined the mould with an electrical resistance method to more accurately evaluate the hot tearing severity of Al-Mg alloys. The measurement details for this approach are described in Section 2.2.3. To obtain more quantitative information, the mould was recently combined with in situ neutron diffraction [61] and in situ XRD [58] to measure the stress/strain evolutions in the solidifying alloys, as discussed in Section 2.2.3. As shown in Fig. 2.5, this apparatus inherits the advantages of the "cold finger" mould. In addition, this approach simulates the effect of the liquid feeding occurring in DC casting and makes the hot tear measurement visible and quantitative.

To measure the strength development and strain accommodation during solidification, Instone et al. [62] developed a CHT rig based on an Instron tensile testing machine to mimic the solidification conditions encountered in DC casting. A schematic of the device is shown in Fig. 2.7(a). A feeder situated at the centre enabled liquid filling. Two test bars were used, one to record the load or

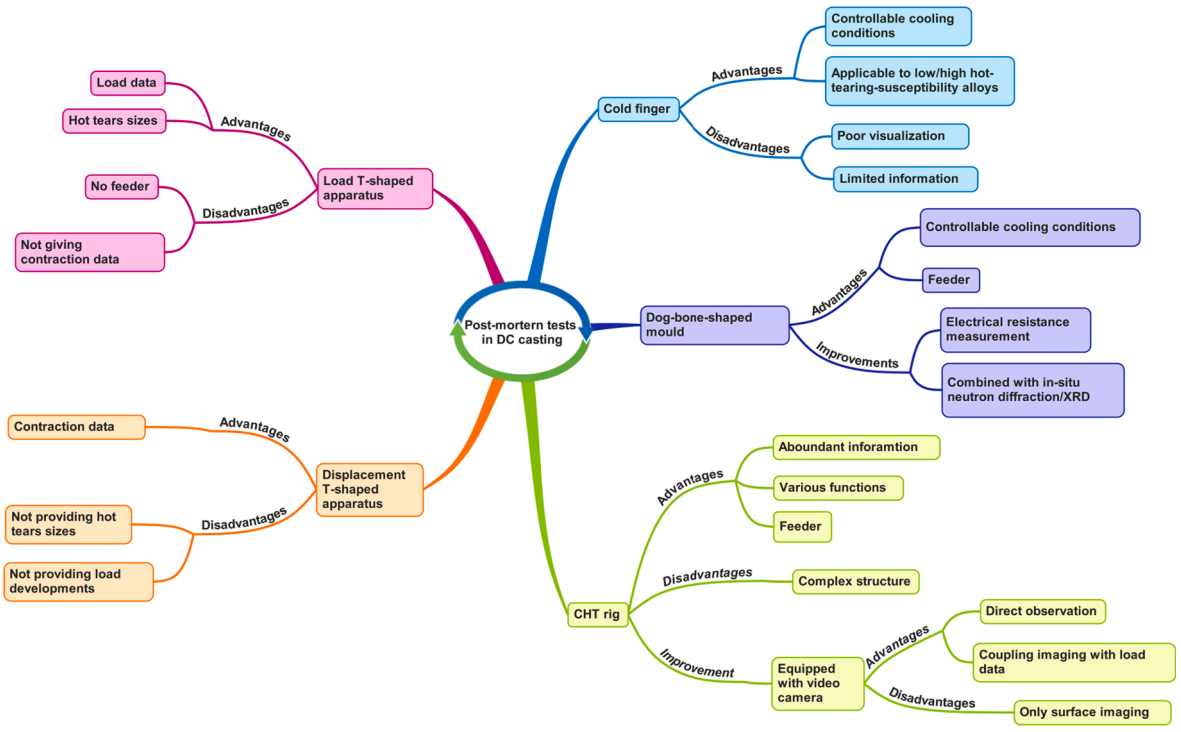

Fig. 2.5. An outline of the post-mortem tests simulating DC casting.

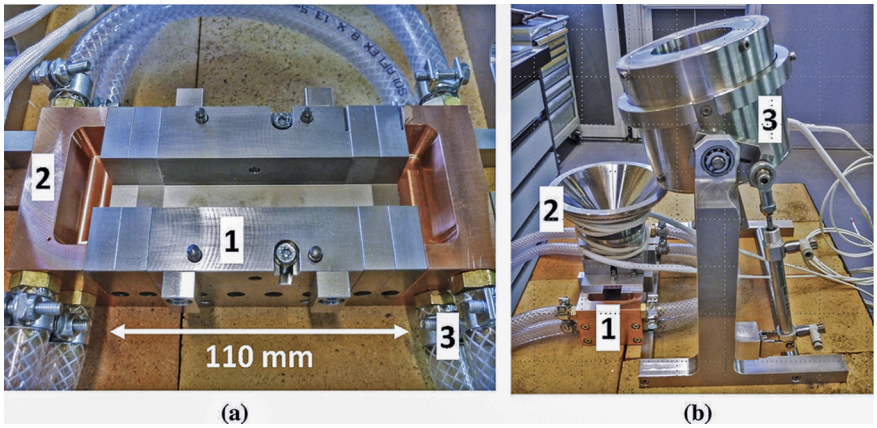

Fig. 2.6. (a) Dog-bone-shaped mould: 1, steel mould; 2, water-cooled copper mould; and 3, water pipe; (b) experimental device including 1, dog-bone-shaped mould; 2, feeder; and 3, rotating pouring system [58].

displacement development, and the other to measure the cracks. Ceramic fibre insulation was applied to the centre of each bar to form a directional solidification pattern where two solidification fronts meet at the centre of the bar, with approximately uniform temperature fields in the cross-section direction. In the initial state, several thermocouples were installed in the right bar, as shown in Fig. 2.7(a), to measure the temperature evolution. However, the introduction of these external bodies influenced the size of the hot tears. To overcome this difficulty, the thermocouples were installed in the left bar, as shown in Fig. 2.7(a) [63]. Three kinds of experiments can be carried out using this device: (1) testing without constraining the movable end to measure the linear contraction [62]; (2) testing by constraining the two ends without moving the crosshead of the tensile testing machine [29,54,62,64–68]; and (3) testing by constraining the two ends and moving the crosshead of the tensile testing machine at a constant displacement rate [69]. The CHT test can provide considerable information pertaining to the linear contraction [62], load evolution during solidification [29,54,62,64–68], semi-solid mechanical properties [69], and hot tearing susceptibility [29,54,62,64–68]. Thus, the device has been widely applied to different alloying systems, such as relatively pure Al [62], Al-Cu [63,68], 3xxx [65], 6xxx [29,54,64–66], and 7xxx [62,65] alloys. To capture the formation and propagation of the hot tears in situ, the CHT rig was further improved by installing an observation system (Fig. 2.7(b) and (c)) [70], as described in Section 2.2.2. As shown in Fig. 2.5, the CHT rig can provide fruitful quantitative information related to hot tearing through the various functional components. These aspects are the reasons for the popularity of this system in hot tearing research in recent years.

Eskin et al. [14,71] developed an unconstrained T-shaped device simulating the DC casting process of billets to measure the linear contraction during solidification. As shown in Fig. 2.8(a), it consists of a K-type thermocouple (A), a T-shaped graphite mould (C) with one sliding wall (D), a water-cooled bronze base (E) that can yield similar cooling rates (5–10 K/s) as those employed in DC casting, an LVDT (F), and a computer-based data acquisition system. The cross-section of the T-shape cavity is thinner than that of the main cavity, which allows the melt to solidify more rapidly. Therefore, the solidifying sample is fixed on this side. On the opposite side, a metallic rod is fixed in the moving wall to attach the solidifying metal, to ensure the position of the moving wall can be detected by the LVDT. The thermocouple is placed vertically in the centre of the sample (B), 1.5 mm from the mould bottom. During the experiment, the displacement of the sliding wall and temperatures are recorded simultaneously. Refractory materials are applied in the centre of the mould to reduce the central cross-section temperature gradients and ensure that the solidification fronts encounter each other in the zone in which the temperature is monitored. This device has been widely applied to measure the linear contraction behaviour of different alloying systems, including binary [14,72–74] and commercial [14,26,71,75,76] aluminium alloys (see Section 3.1), although this approach cannot provide information regarding the size of the hot tears and load development during solidification, as shown in Fig. 2.5.

Li et al. [77] modified this T-shaped device to measure the size of the hot tears and load development of DC-cast billets. As shown in Fig. 2.8(b), it consists of the following main parts: a T-shaped graphite mould (A) with a graphite block (B), water-cooled bronze base (C), load cell (E), specific setup (D) to fasten the load cell, and data acquisition system. The load cell and fastening setup are used to constrain the casting during solidification. A K-type thermocouple is inserted from the centre of the mould bottom to lower its adverse effect on the measurement results. Thermal insulation materials are applied at the centre of the mould to ensure that the central cross-section temperature gradients are as uniform as possible; in this manner, the measured load development can reflect the stress development in the hot spot zone. Two groups of tests are conducted, i.e., with and without a thermocouple. In the test group involving a thermocouple, the load and temperature developments are recorded. In the test group not involving a thermocouple, the crack width is determined by avoiding the cracking initiated by the thermocouple. The advantages and limitations of this device are summarised in Fig. 2.5. Importantly, this device provides information on the hot tearing susceptibility and load developments, and it has been applied to different AA7xxx alloys [26,76–78]. Recently, Pan et al. [79] replaced the T-shaped graphite mould with a bronze mould to obtain higher cooling rates ranging from 11 to 24 K/s to further simulate the solidification during fusion welding. Compared with the CHT rig, this T-shaped device does not contain a feeder to provide good liquid feeding to the critical region during solidification, and this aspect

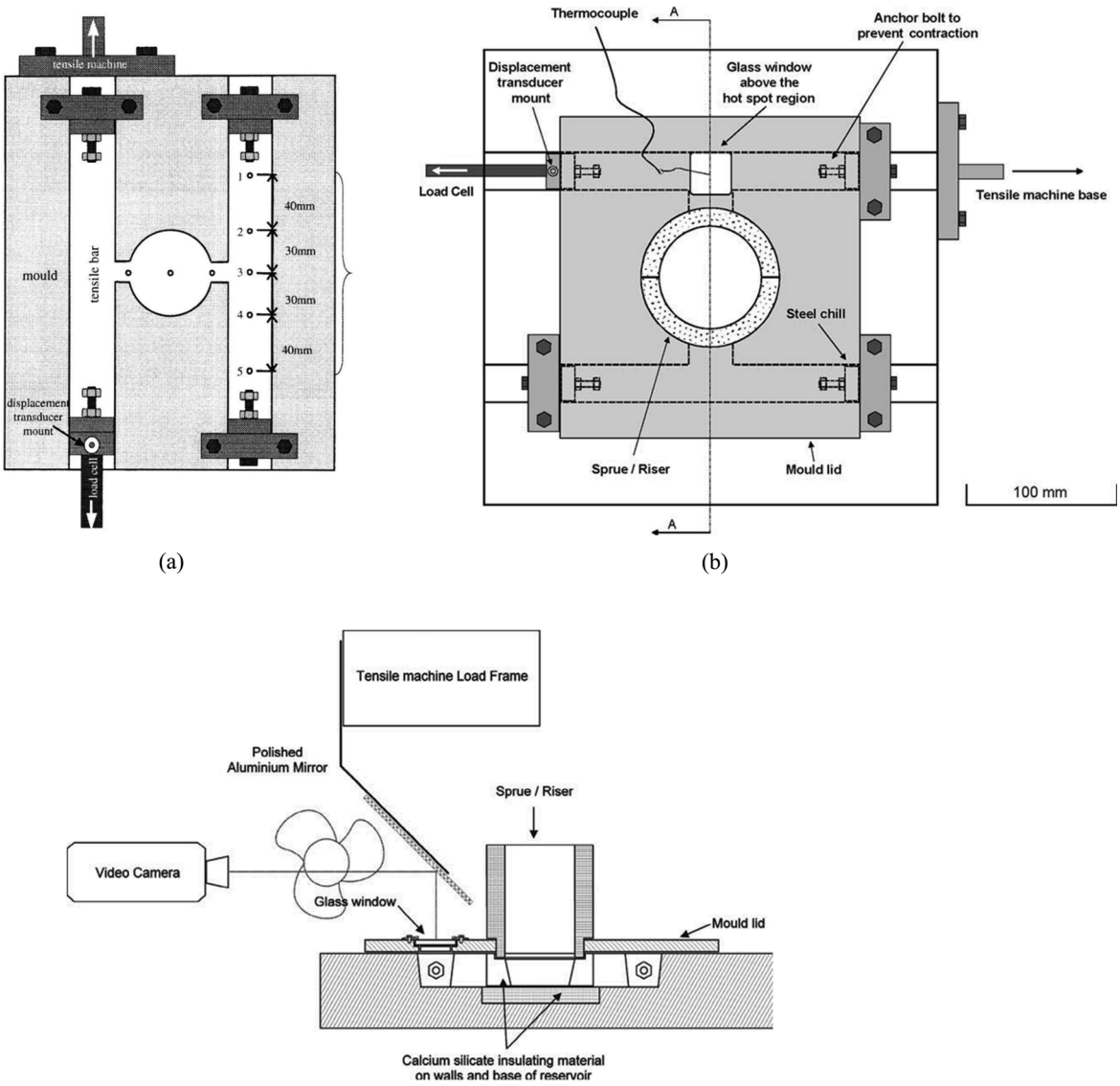

Fig. 2.7. (a) Schematic of the CHT rig developed by Instone et al. [62], (b) improved CHT rig with an observation system, and (c) cross-section of the improved rig through section A-A in (b) [70].

can be improved in future work. Furthermore, the thermal contraction data can be easily achieved by replacing the load sensor with a displacement sensor and removing the fastening setup. Note that the obtained load development from the CHT rig and load T-shaped devices can be used to determine the rigidity point as an input for certain hot tearing criteria (Section 3.2).

The above-mentioned dedicated hot tearing tests simulating the DC casting are summarised in Fig. 2.5 to highlight their capabilities and limitations. Many researchers have attempted to design a testing device to better simulate the process of DC casting and obtain reliable measurements of hot tearing, for instance, by adding a feeder and controlling the cooling conditions. Additionally, a large amount of quantitative data can be obtained through in situ load/displacement/temperature measurements, such as that of the rigidity temperature, amount of linear contraction, and hot tear initiation temperature, which can help investigate the hot tearing phenomenon. These data are summarised in Section 3. Note that these methods can be classified only as refined technological probe techniques instead of pure mechanical tests because they provide only the tensile force at a certain temperature, and not the UTS. Nevertheless, these approaches are valuable as the associated setup is considerably simpler than that of semi-solid tensile testing devices. Furthermore, the CHT rig and load T-shape apparatus have been widely applied to different commercial aluminium alloys series, and certain results have demonstrated a reasonable agreement with the DC casting practice. Thus, these approaches can be further optimised for future hot tearing research. Although various casting parameters can be studied based on these devices, the casting speed has not been considered due to the limited size of the testing device. In this context, developing a small trial DC casting machine can allow

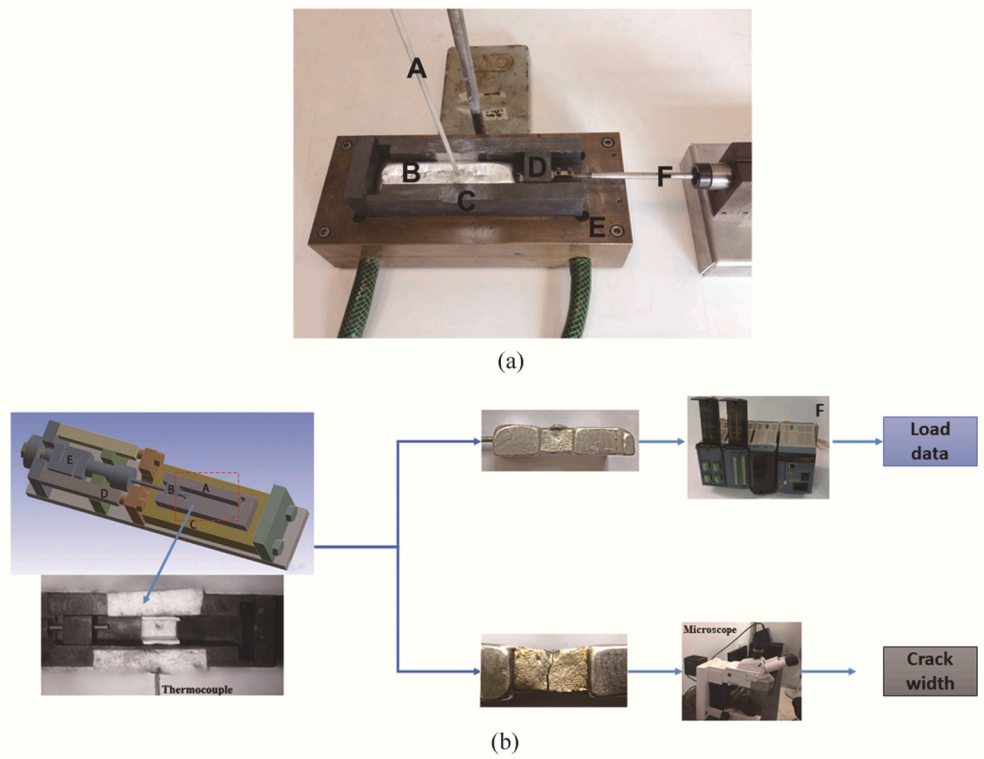

Fig. 2.8. (a) T-shaped displacement testing device developed by Eskin et al. [71] and (b) modified by Li et al. with a load cell [77].

more casting parameters to be studied and bridge the gap between the dedicated hot tearing tests and industrial practice. In general, a trial casting machine should be equipped with several functional components, such as load/displacement sensors, to obtain more quantitative data. Finally, ensuring the precise melting and controlling the pouring procedures are key to ensure the reproducibility of the experimental results.

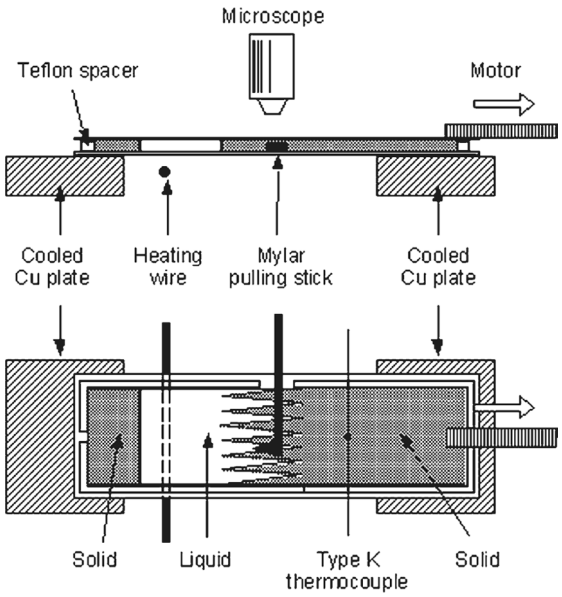

Fig. 2.9. Schematic of the experimental setup used by Farup et al. [80].

2.2.2. In situ observations

Traditionally, the castings in which hot tears occur are often examined or observed after complete solidification, i.e., post-mortem or ex situ. However, in this scenario, the real-time solidification microstructure and defect evolution information, such as that of the formation and propagation of pores and hot tears, may be lost. At present, the development of characterisation techniques has facilitated in situ observation during casting and solidification. High-resolution digital cameras and the synchrotron X-ray micro tomography technique have been employed to investigate hot tearing, thereby providing a deeper understanding of the mechanisms behind hot tearing.

Farup et al. [80] used succinonitrile-acetone to study the initiation and propagation of hot tears. This material is highly similar to aluminium alloys in terms of the solidification shrinkage, solidification morphology and creep behaviour close to and below the solidus. The basic idea is to form a stable mushy zone, which only has one layer of forming dendrites to allow direct observation of the initiation and propagation of hot tears and liquid feeding. As shown in Fig. 2.9, two glass layers are separated by a Teflon spacer, and a K-type thermocouple and pulling stick are plugged in the cell together. The hot tearing is observed by a video camera connected to a microscope. When the solidification fronts contact each other, the puller is moved to ensure that it does not move across a grain boundary. The puller is pulled when it is surrounded by solids and the liquid forms continuous films only at the grain boundaries or drops between the coalesced dendrite arms. This technique has enabled researchers to gain insight into several hot tearing mechanisms such as hot tearing initiation and propagation. However, as shown in Fig. 2.10, these mechanisms are not fully applicable to aluminium alloys due to the differences in the organic and aluminium alloys (for example, in the context of the formation of the last eutectics in aluminium alloys).

To observe the hot tear nucleation and propagation in aluminium alloys, Davidson et al. [70] improved the CHT rig by implementing an observation system. Fig. 2.7(b) shows a plan view of the modified mould and Fig. 2.7(c) shows the associated cross-section taken through section A-A. To allow direct observation, a new glass window is installed above the hot spot zone. A mirror inclined at 45° is placed above the glass window. Two K-type thermocouples are inserted into the mould through a hole and placed at the centre of

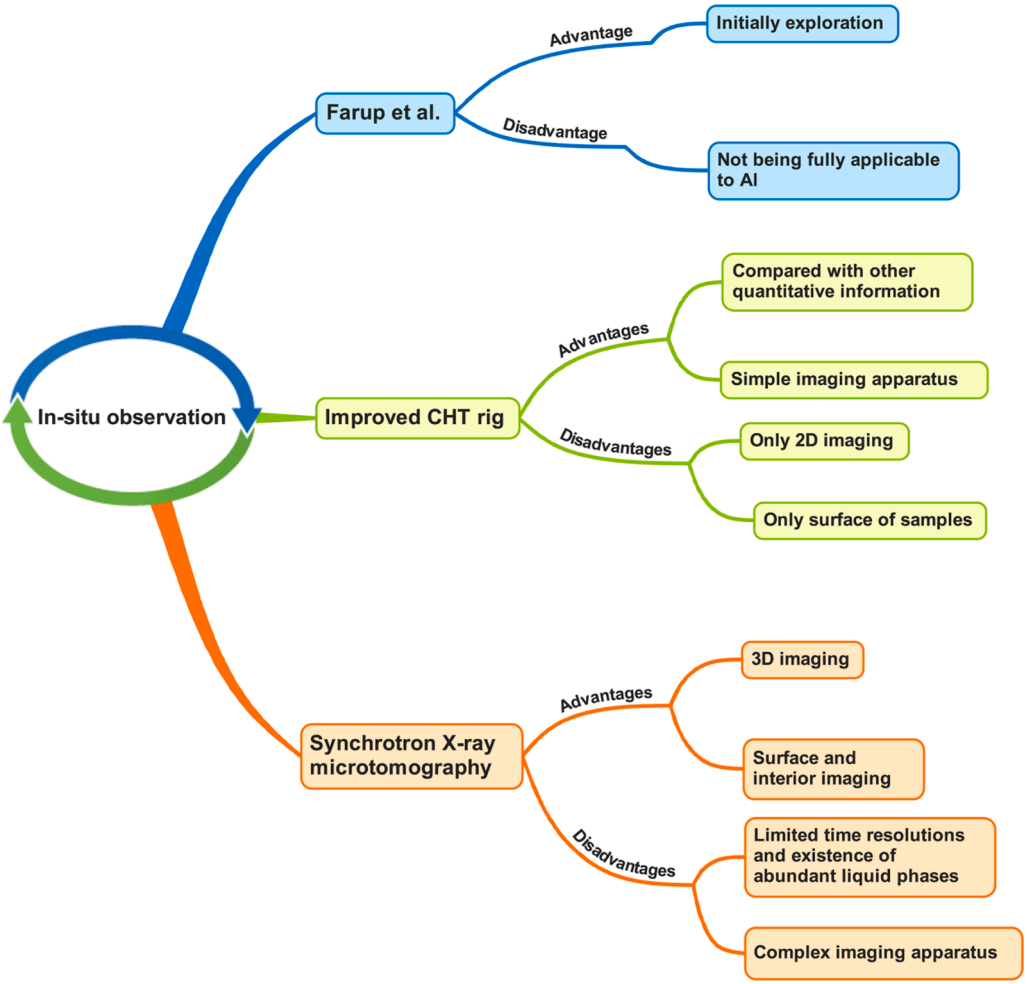

Fig. 2.10. In situ observation tests outline.

the hot spot zone and in the ingate. A video camera is employed to record the imaging information in the hot spot zone upon solidification. The advantages and limitations of this improved device are summarised in Fig. 2.10. Firstly, the imaging system is simple and can be easily extended to other hot tearing tests. Moreover, combining the visual observation with the load-temperature-time data can enhance the understanding of the nucleation and propagation of hot tears. Mitchell et al. [67] further analysed the images by using a digital image software to measure the displacement and strain by tracking the movement of the discrete points of the casting's surface, which can be correlated with the process of hot tear formation. However, this technique can only examine the casting surfaces, and internal 3D images cannot be obtained.

In recent times, the synchrotron X-ray micro tomography technique has been considerably improved and applied to the research of

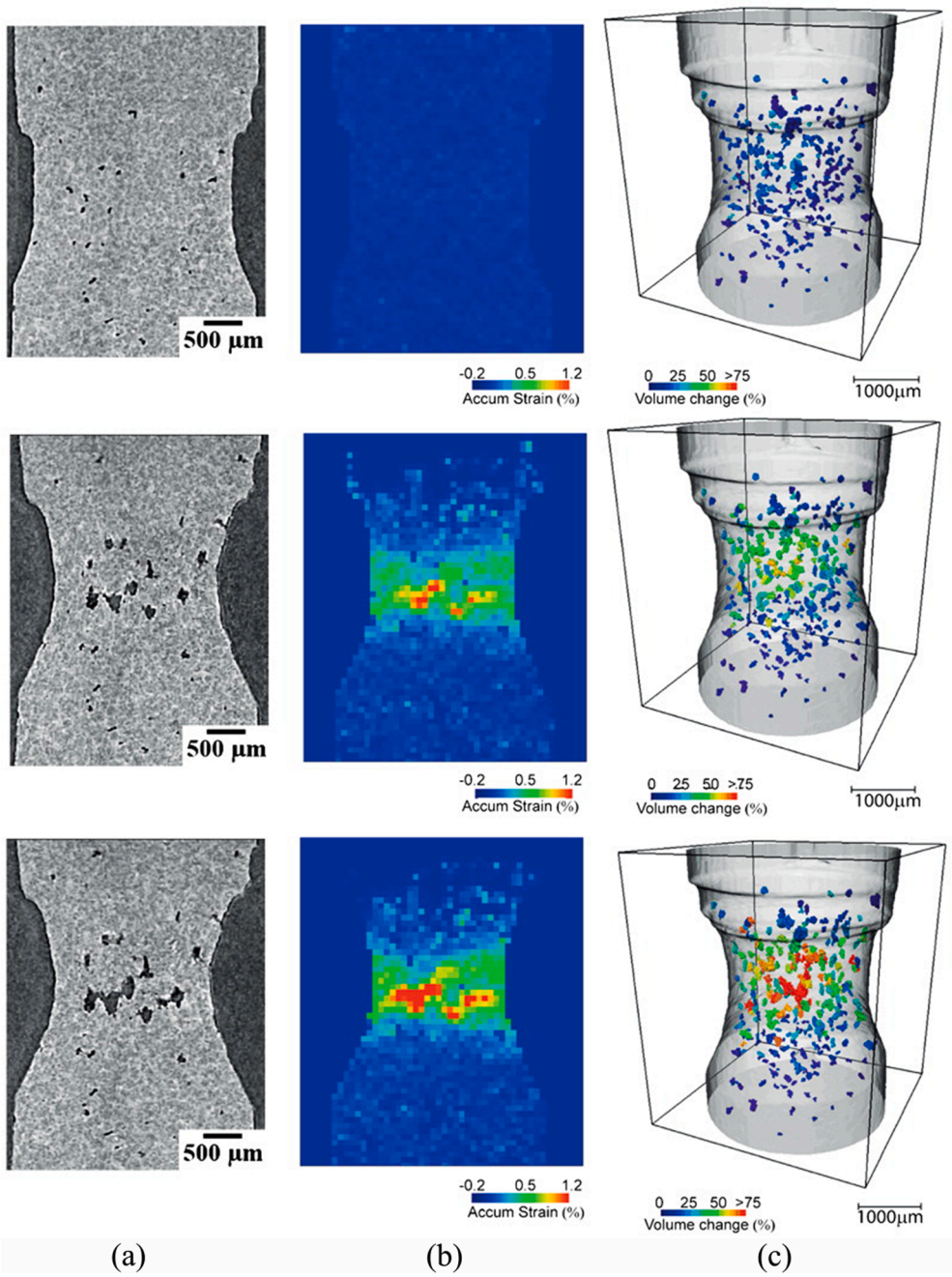

Fig. 2.11. 3D images obtained by semi-solid tensile testing in an Al-Cu alloy: (a) longitudinal sections of typical 3D damage evolutions during the hot tearing, (b) the local strain field measured by digital volume correlation between continuous photos, and (c) the variation of void volume corresponding to the original volume at the initial stage of hot tearing [86].

hot tearing using fast imaging [8,81–85]. Specifically, a semi-solid tester was developed based on this technique to realise the in situ observation of the hot tearing of aluminium alloys [85–87]. The specimen was heated to a specific temperature and maintained at this temperature for a certain time. Subsequently, tensile testing was conducted isothermally, with the desired strain rate. During the deformation, the sample was continuously rotated, and a complete 3D volume was obtained after a pre-specified time step. A sequence of 3D volumes was recorded, from the non-deformed state to the complete rapture state to allow direct tracking of the initiation and propagation of the hot tears. As shown in Fig. 2.11, the development of hot tears can be observed directly, related to the local variation in the strain obtained by the digital volume correlation between continuous images and related to the variation of the void volume corresponding to the original volume at the initial stage of the hot tearing. This 3D visualisation technique can be used to measure the size distribution of hot tears to evaluate the hot tearing susceptibility by predefining the critical size of the pores to enable the generation of hot tears. Moreover, the technique can be used to quantise the evolutions of the liquid distribution and grain bridging/coalescence with solid fractions [88]. In situ studies have suggested that the observation of the development of the semi-solid microstructure by the 3D synchrotron X-ray micro tomography technique is considerably different from that using traditional quenching methods. Because the microstructure is considerably modified upon quenching, the results obtained by characterizing the samples at room temperature may often be misleading [88].

The characteristics of these tests pertaining to in situ observations are summarised in Fig. 2.10 to provide a clear overview of these techniques. In situ observations of the hot tearing phenomena by using a video camera is a simple and useful method. However, this technique involves a major limitation that it can only observe the 2D phenomena occurred in the upper surface of the samples. The synchrotron X-ray micro tomography approach can overcome this limitation, as it can generate 3D images in which the sample interior is visible. This approach is also applicable to realise the in situ observation of the nucleation of hot tearing occurring in the welding and AM processes, which can help optimise the corresponding process parameters [89,90]. The key limitation of this type of in situ observation is that the sample is tested in isothermal conditions and not during continuous cooling. Owing to the limited time resolution and presence of abundant liquid phases, the sample cannot be rotated to acquire the 3D images during continuous cooling [58,61,89], and this aspect must be considered in future work. The details of this advanced synchrotron X-ray micro tomography technique can be found in Refs. [91,92], which can guide its improvement and application in hot tearing research. In the future, the improved in situ observation technique can be combined with sophisticated hot tearing devices to enable the comparison of the visual observations with other quantitative data, such as the load-temperature-time curves.

2.2.3. *Measurement of physical properties*

In addition to the combination of advanced visualisation techniques with hot tearing devices, certain physical methods can be used to study the hot tearing behaviour. For example, the electrical resistance method [15,60] can be used to obtain the total crack area on the surface and subsurface, a part of which cannot be directly observed through visual methods. The acoustic emission [48] technology

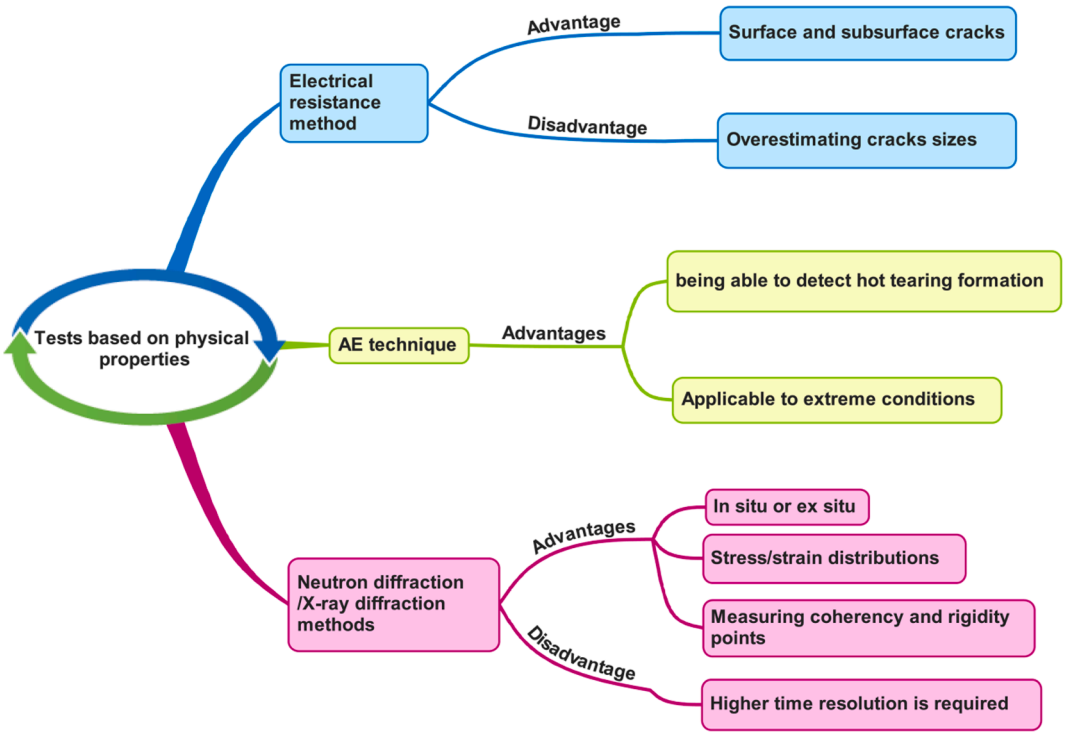

Fig. 2.12. Physical properties measuring tests.

can be used to accurately detect hot tearing initiation and propagation. Moreover, the X-ray diffraction [58,93] and neutron diffraction [61,94–96] techniques can determine the distribution of the stresses and/or strains of the castings. Fig. 2.12 presents an outline of these tests including their capabilities and limitations. These special techniques are discussed in detail in the following text.

As shown in Fig. 2.12, the electrical resistance method can be used to measure the total crack area on the surface and subsurface by determining the electrical resistance through different locations of a specimen. Clyne and Davies [60] applied this technique to the dog-bone-shaped mould (Fig. 2.6). The electrical resistance setup is shown in Fig. 2.13. The reduction in the cross-section area from the original value to the final value because of the hot tearing expressed as the effective area fraction of hot tearing, X_{cr}, is related to the measured resistance. It is given by

$$X_{cr} = 1 - \frac{R_{40}^{av}}{2(R_{100}^{av} - 2R_{40}^{av})} \tag{2.2}$$

where R_{100}^{av} and R_{40}^{av} are the average resistance reading for 100 mm and 40 mm lengths, respectively. $X_{cr} = 0$ is given for the section without hot tearing and $X_{cr} = 1$ is given for the completely broken section. The electrical measurement can be regarded to be a sensitive indicator of the hot tearing susceptibility. However, this technique will overestimate the overall crack area (Fig. 2.12) as certain voids below the critical size corresponding to the hot tearing initiation are included. As mentioned above, the synchrotron X-ray micro tomography technique can overcome this problem by predefining the critical size of the pore for the formation of hot tears.

Another relevant method is the AE technique, where transient elastic waves (AE signals) are generated by a rapid release of stored energy. These waves, which can be correlated with hot tearing or cold cracking, are detected using an AE sensor [48]. Pekguleryuz et al. [48] used this technique to perform an in situ study of the crack formation in an AA1050 alloy. A typical result obtained from their investigation is shown in Fig. 2.14. At the last stage of solidification (region II), two peaks with an AE energy of 1311 energy units (ea.) and an average frequency of 136 kHz could be observed, attributed to the occurrence of hot tearing. An inverse relationship was found between the HTS based on the criterion of Clyne and Davies [15] and the AE energy (E_{total}), i.e., HTS $\cong 167(E_{\text{total}})^{-0.8}$. The two peaks in region III (below the solidus) were attributed to cold cracking. Note that the technique was sensitive even at high cooling rates, and thus, it could be applied to investigate the welding [97,98] and AM [99,100] processes (Fig. 2.12).

It is crucial to know the distribution of the strains and/or stresses, although in situ measurements are considerably difficult to perform because of the high temperatures. Recently, neutron diffraction techniques [94–96] and 2D XRD methods [93] have been used to measure the distribution of the residual strains or stresses of castings. These were performed once solidification was finished and the samples were removed from the mould, i.e., the actual measurement is ex situ. For example, D'Elia et al. [94] employed the neutron diffraction technique to quantify the residual strain associated with hot tearing in a B206 Al-Cu alloy. A neutron beam from a nuclear reactor is directed to a specific location within a stressed specimen. The angle of diffraction $2\theta_{\text{hkl}}$ is obtained by measuring the Debye-Scherrer ring spacings. The interplanar spacing d_{hkl} is determined by the following equation:

$$n\lambda = 2d_{\text{hkl}}\sin\theta_{\text{hkl}} \tag{2.3}$$

where λ is the wavelength, and n is the order of diffraction. The residual strain ε_{hkl} can be calculated using the equation:

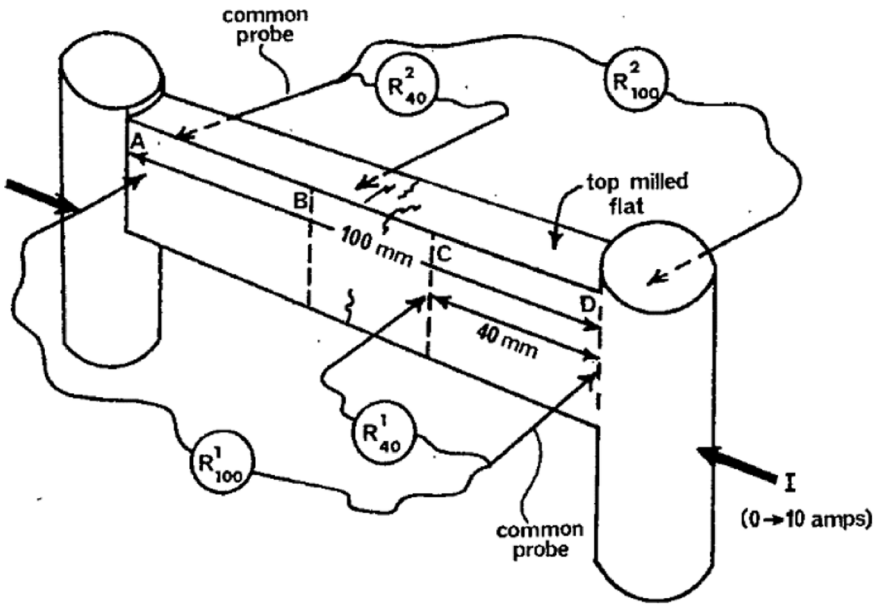

Fig. 2.13. The setup of the measurement of electrical resistance [60].

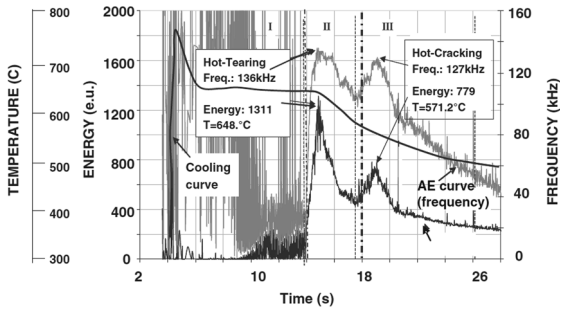

Fig. 2.14. AE average frequency and energy vs time plotted with the cooling curve [48].

$$\varepsilon_{hkl} = \frac{d_{hkl} - d_{o-hkl}}{d_{o-hkl}} \tag{2.4}$$

where d_{o-hkl} is the interplanar spacing of the unstressed specimen. When a material is subjected to a tensile load, d_{hkl} increases in the tensile direction with respect to its stress-free value d_{o-hkl}, and ε_{hkl} is a positive value. Similarly, d_{hkl} decreases for compressive loads and ε_{hkl} is negative. Saito et al. [93] employed the 2D X-ray diffraction method to measure the residual stress tensor around the cracks in Al-Sn alloys. In this approach, because the penetration depth of a single-direction X-ray is limited, tri-axial stress tensors are measured. The measurement of the strain is similar to that when applying the neutron diffraction strain mapping. The stress of the sample can be calculated using Poisson's ratio and Young's modulus based on Hooke's Law. Note that the penetration of neutrons is higher than that of single-direction X-rays.

Furthermore, the in situ measurement of the stress/strain evolution in solidifying metals has a higher significance than the measurement of residual stresses in as-cast samples. Drezet et al. [61] applied the in situ neutron diffraction technique in a dog-bone-shaped mould (Fig. 2.6) to investigate the effect of the cooling rates on the coherency and rigidity points in grain-refined Al-13 wt % Cu alloys. It was found that at high cooling rates the rigidity point was reached when eutectics formed and the grains did not sufficiently coalesce. However, the time resolution was extremely small (11 s), requiring further improvement. Drezet et al. [58] further applied the in situ XRD technique in a similar mould to investigate the effect of the cooling rates on the coalescence onset point and micro-pores/hot tear formation in Al-6.2 wt% Zn alloys with a higher time resolution of 0.5 s. The hot spot zone was detected using X-rays. The small deviations of the lattice parameter evolution at high solid fractions were attributed to the release of the accumulated stresses/strains caused by the formation of the micro-pores or hot tears. Additionally, it was considered that the coalescence onset temperature corresponded to the point where the decrease in the lattice parameter began to deviate from its linear relationship. In the future, the in situ XRD technique should be applied to a higher variety of commercial aluminium alloys for faster cooling configurations at higher time resolutions (Fig. 2.12). The measurement in an unconstrained casting should be carried out to in situ determine the lattice parameter of the unstressed specimen. Subsequently, the strain can be determined according to Eq. (2.4).

Although the above-mentioned methods can help enhance the understanding of hot tearing, the results from different devices cannot be easily compared. Unlike the shape casting process, which involves different production technologies (Section 1.1), a standard testing framework should be developed for DC casting. In this configuration, the researchers can collaboratively investigate the hot tearing phenomenon occurring in DC casting. The testing framework to simulate the DC casting conditions must be able to collect representative quantitative data, such as the load/thermal contraction-temperature-time curves combined with the real-time 3D morphology of the voids and hot tears. These data can later be applied to clarify the hot tearing mechanisms of aluminium alloys and as an input to hot tearing simulations. The effect of the alloy compositions and process parameters should be evaluated using this method including the grain refiners, melt temperatures, water flow rates, casting dimensions, and casting speeds. A detailed description of this testing framework is presented in Section 6.2.

3. Mushy zone behaviour related to hot tearing

With the development of the above-mentioned hot tearing characterisation methods, the mushy zone behaviour related to hot tearing, including thermal contraction, load development, and semi-solid mechanical properties, has been systematically investigated. The aspects summarised in the following section are the essential inputs for the hot tearing criteria and constitutive equations.

3.1. Linear contraction behaviour during solidification

Three factors are often used to characterise the overall shrinkage: solidification shrinkage, thermal contraction, and linear contraction [14]. A schematic of the three types of shrinkages is shown in Fig. 3.1. The solidification shrinkage is the volumetric shrinkage resulting from the liquid-solid phase transformation. The amount of solidification shrinkage in aluminium alloys is about 6–8 vol%. The thermal contraction is the volumetric contraction of the solid phase because of the temperature dependence of the solid density. The linear contraction is the horizontal variation in the linear dimension of the casting upon solidification. The amount of linear contraction often changes from one thousandth to one percent. Before the onset of the linear contraction, a continuous dendrite

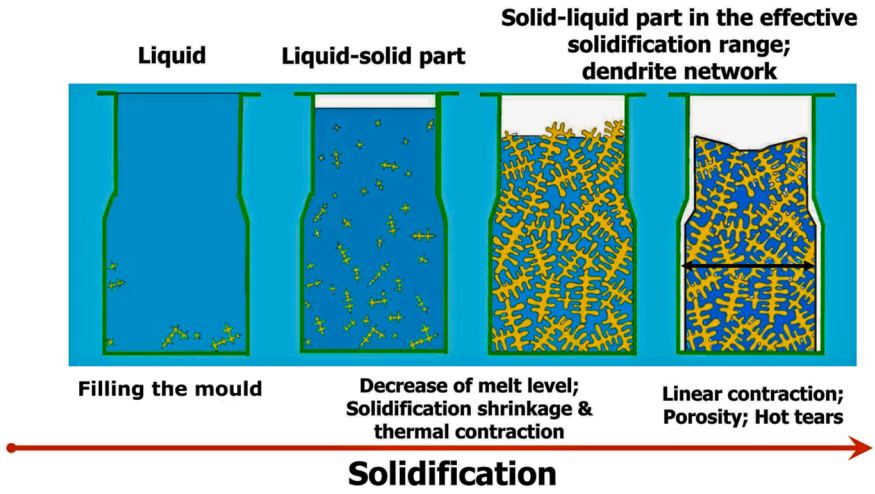

Fig. 3.1. Schematic of the development of solidification shrinkage, thermal contraction, and linear contraction during solidification [7].

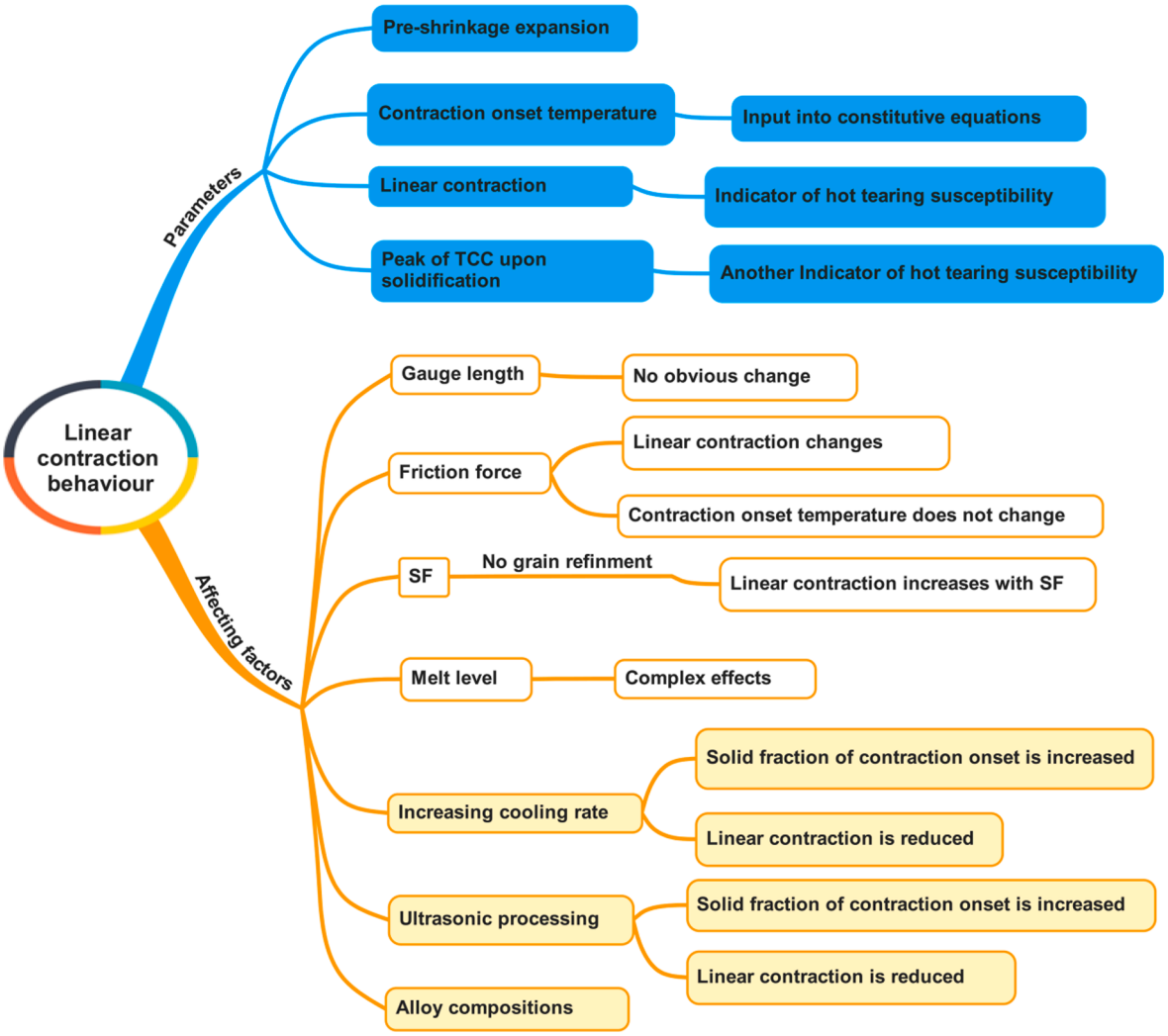

Fig. 3.2. An outline of the linear contraction behaviour, including the quantitative data obtained from the contraction curve during solidification.

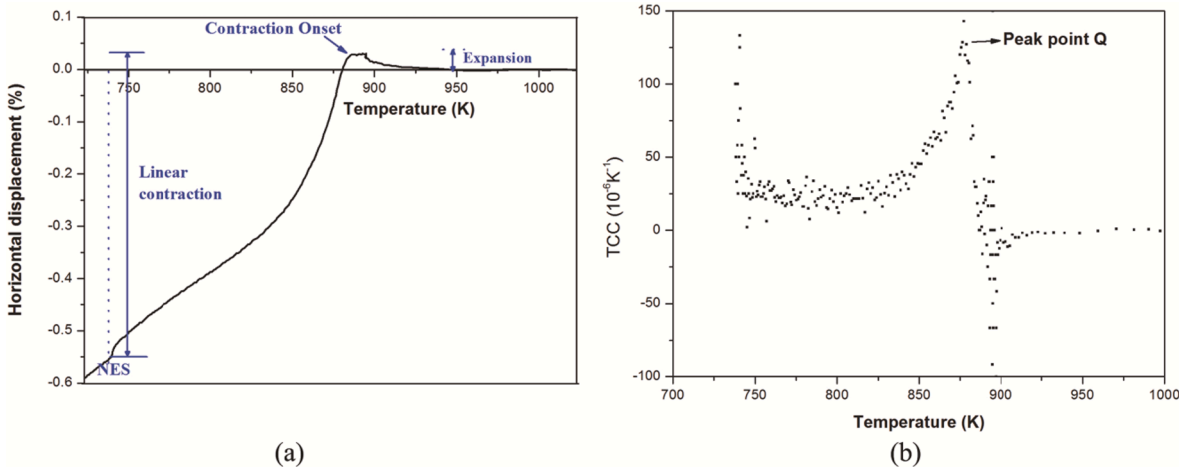

Fig. 3.3. (a) Example of the contraction curve upon solidification of AA7050 alloy; (b) the corresponding thermal contraction coefficient (TCC) curve during solidification [26].

skeleton is not present. The solidification shrinkage and thermal contraction manifest as a decrease in the height of the melt in a shape mould casting. This phenomenon cannot be observed during DC casting due to the continuous feeding of the liquid. When linear contraction starts, continuous dendrite skeletons are formed and start to transfer tensile stresses. Those volumetric variations manifest themselves as horizontal linear contractions. The temperature where linear contraction starts is identified as the rigidity temperature. An outline of the linear contraction behaviour is presented in Fig. 3.2, and certain factors influencing the contraction behaviour are clarified.

The technique to measure the linear solidification contraction is illustrated in Fig. 2.8(a). Fig. 3.3 shows an example of a contraction curve during the solidification of an AA7050 alloy [26]. The pre-shrinkage expansion (Fig. 3.3(a)), which is mainly caused by the release of gas (usually hydrogen) and the pressure drop over the mushy zone, occurs initially, and the expansion relies on the alloy system and casting conditions. When the contraction onset temperature is reached, a skeleton of the solid phases is formed, which allows the alloy to retain its shape, and the contraction initiation manifests the horizontal change in the linear dimension of the casting. The linear contraction (ε_s) is determined as follows [14]:

$$\varepsilon_s = \frac{l_0 + \Delta l_{exp} - l_f}{l_0} \times 100\% \tag{3.1}$$

where l_0 is the original length of the cavity;Δl_{exp} is the pre-shrinkage expansion, and l_f is the length of the casting at the NES. The linear TCC upon solidification is calculated as [26]:

$$TCC = \frac{l_{T_2} - l_{T_1}}{l_0(T_2 - T_1)} \tag{3.2}$$

where T_2 and T_1 are the temperatures ($T_2 > T_1$) during solidification; l_{T_2} and l_{T_1} are the positions of the LVDT at T_2 and T_1, respectively. Fig. 3.3(b) shows an example of the TCC curve during solidification. The TCC rises rapidly to a peak value Q. Subsequently, the TCC value decreases gradually. As shown in Fig. 3.2, these parameters can be used to reflect the hot tearing susceptibility, as described in a later section.

Several factors affecting the linear contraction behaviour have been studied [14,72], as shown in Fig. 3.2. First, the gauge length does not affect the contraction behaviour. Second, the linear contraction decreases as the friction force increases, as shown in Fig. 3.4. The contraction onset temperature remains unchanged. Third, a structure factor SF is defined as[1]

$$SF = V_c^{-0.33}/D_{gr} \tag{3.3}$$

where V_c is the cooling rate and D_{gr} is the grain size. The SF is adjusted by changing the cooling rate and melt temperature. Note that grain refinement is not used in this study. It is found from Fig. 3.4 that the amount of linear contraction increases with the increase in theSF, i.e., the smaller the grain and the coarser the dendrite arm, the larger the linear solidification contraction. This trend changes when grain refiners are added, as shown in Figs. 3.8–3.10. This is because adding grain refiners has a significant effect on grain size but little effect on SDAS. Finally, the melt level in the mould influences the linear contraction behaviour, owing to the combined effect of the thermal gradients, dimensionality of the solidifying sample (plane or 3D casting), and mechanical and rheological properties of the mushy zone [14].

[1] Actually Eq. 3–3 can be read as SF= SDAS/D_{gr}

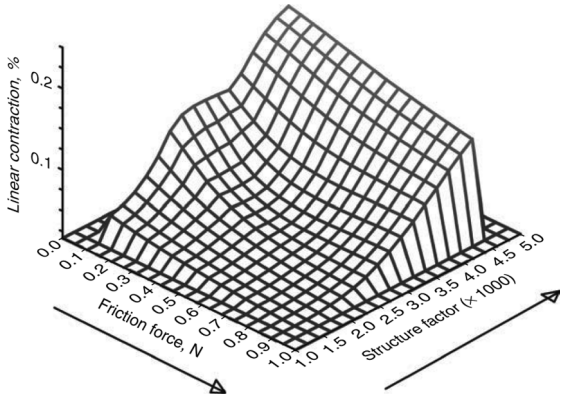

Fig. 3.4. Effect of friction force and structure factor on the linear contraction of Al–4 wt% Cu alloys [72].

Particular melt processing methods can alter the thermal contraction behaviour. Zhang [71] investigated the effect of the addition of Zr and Ti on the thermal contraction behaviour of Al-Cu alloys under ultrasonic processing conditions (Fig. 3.5). In this case, the pre-shrinkage expansion is not affected by the processing. This is different from that observed in AA7050 alloys (25 mm-height sample) where a smaller pre-expansion was observed for ultrasonic processing [73]. The unaffected pre-shrinkage expansion in Al-Cu alloys is attributed to the lower hydrogen liquid solubility and smaller sample height (12 mm). Fig. 3.5(a) shows the contraction onset temperature of different Al-Cu alloys. The application of ultrasonic processing decreases the onset temperature and increases the corresponding solid fraction. In addition, ultrasonic processing decreases the amount of linear solidification contraction, as shown in Fig. 3.5(b). The decreased amount of linear contraction for ultrasonic processing decreases the hot tearing susceptibility, which has been demonstrated for an AA7050 alloy [101]. The changes in the contraction onset and the amount of linear contraction are closely related to the columnar-equiaxed transition under ultrasonic processing conditions.

Some binary and commercial aluminium alloys have been tested and an outline of their linear contraction behaviour is given in Fig. 3.6. The details are as follows.

- Binary alloys

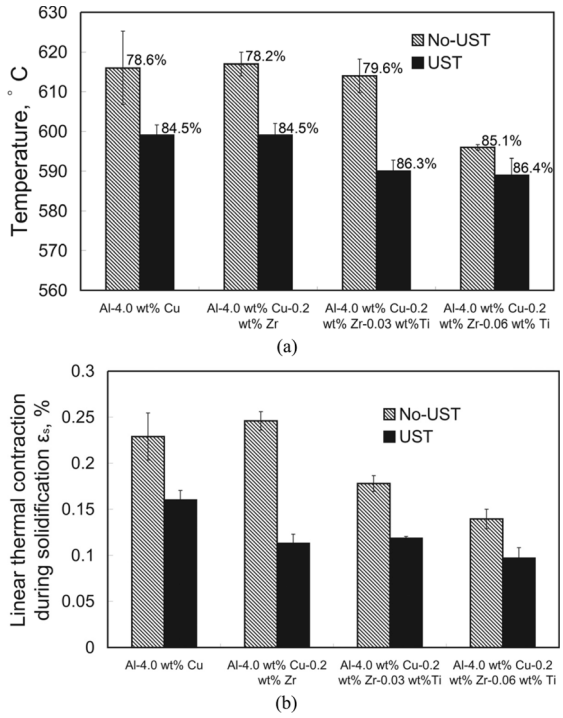

Fig. 3.5. (a) The contraction onset temperature and corresponding solid fraction and (b) amount of linear solidification contraction of different Al-Cu alloys without and with ultrasonic processing [71].

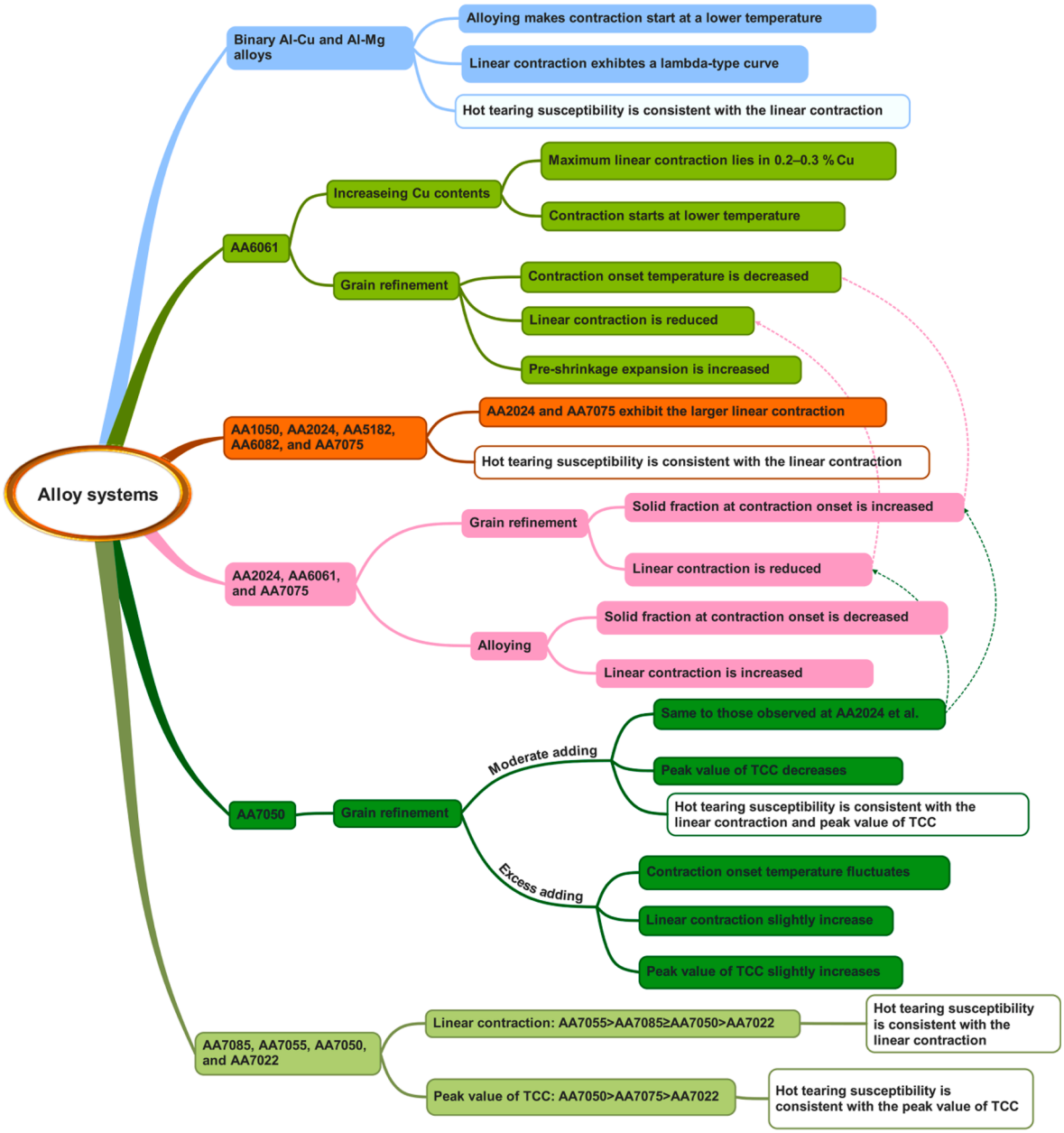

Fig. 3.6. An outline of the linear contraction behaviour of some binary and commercial aluminium alloys. Dotted lines mean that there are similarities between the chosen items.

Fig. 3.7 shows the contraction onset temperature and the amount of linear contraction (ε_s) of Al–Cu and Al–Mg alloys [14], which are superimposed on their phase diagrams. The linear contraction onset point starts at a low temperature, close to or even less than the equilibrium solidus. The amount of linear contraction during solidification, i.e., contraction to the NES, exhibits a strong compositional dependence. For binary Al-Cu and Al-Mg alloys all the variation tendencies of the linear contraction, non-equilibrium solidification range, and hot tearing susceptibility exhibit similar λ-type curves with the similar compositional range corresponding to the maximum values. This maximum linear contraction is attributed to the largest interval between the contraction onset temperature and NES.

The solid fraction corresponding to the linear contraction onset temperature changes with the alloy composition and cooling rate, and its value generally ranges from 0.8 to 0.9. For example, its magnitude varies from 0.95 at 0.3 wt% Cu to 0.8 at 4 wt% Cu at a cooling rate of 3–4 K/s, [74]. When the cooling rate is increased to 8–15 K/s, the solid fraction is up to 0.9 at 4 wt% Cu [72,74].

The analysis of the contraction behaviour upon solidification is straightforward for binary alloys when the phase diagram is considered. Nevertheless, the situation becomes more complex when investigating commercial multi-component alloys, because minor composition changes can dramatically affect the solidification kinetics. Furthermore, grain refinement affects the contraction

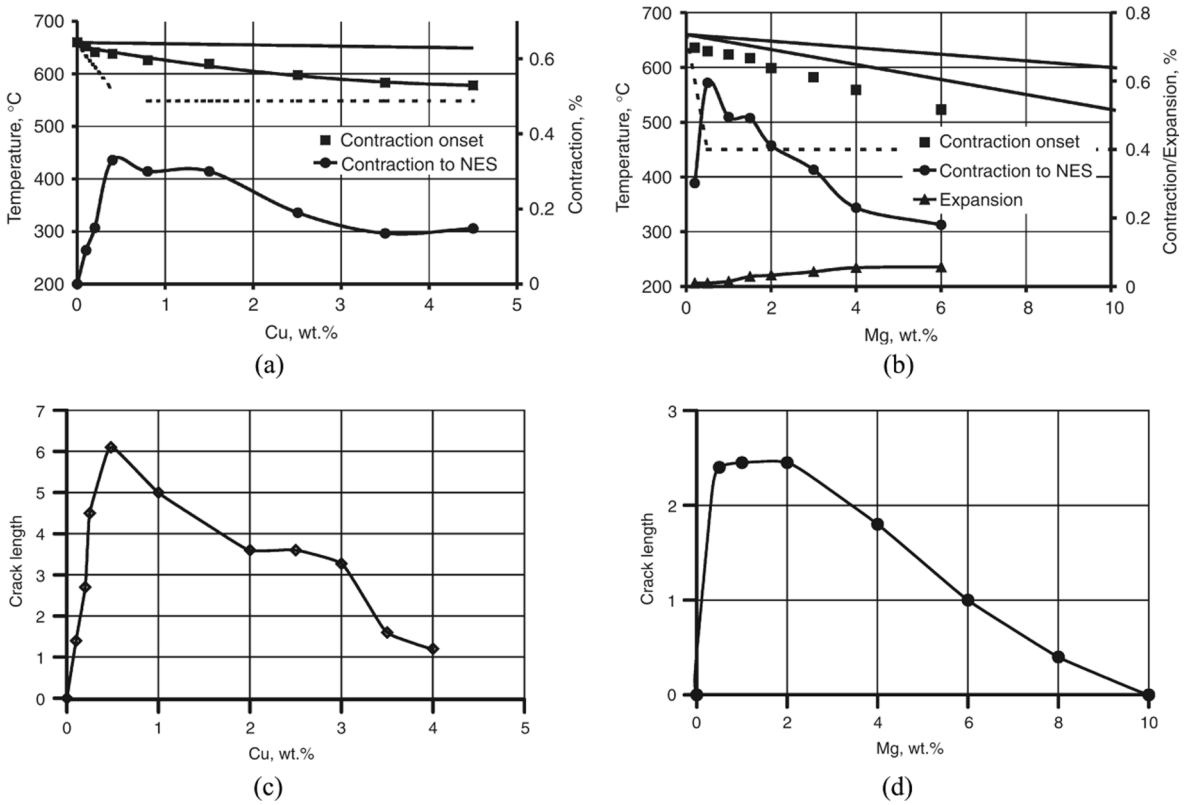

Fig. 3.7. Compositional dependences of (a) and (b) contraction behaviour, and (c) and (d) crack length of Al-Cu and Al-Mg alloys. Note that the dotted line represents the NES [14].

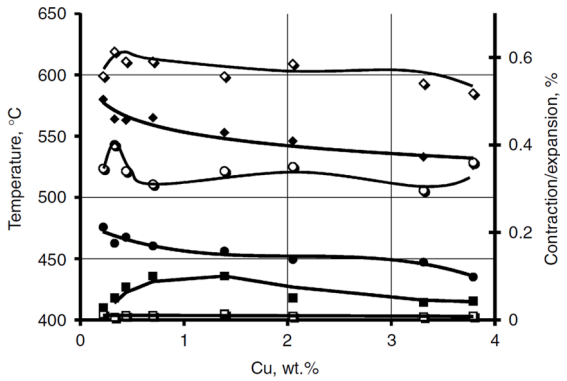

Fig. 3.8. Effect of Cu contents and grain refinement on the expansion/contraction behaviour of 6061-type alloys [14]: ◇, ◆ = contraction onset temperature; ○, ● = contraction to NES (assuming to be 500 °C), %; and □, ■ = pre-shrinkage expansion. Open symbols correspond to non-grain-refined alloys and solid symbols correspond to grain-refined alloys.

behaviour of such alloys.

- Commercial multi-component alloys

The contraction behaviour of 6061-type alloys with different amounts of copper is illustrated in Fig. 3.8 [14] and the corresponding results are summarised in Fig. 3.6. In this study, the effect of grain refinement was examined, and several tendencies are observed. First, the maximum amounts of linear contraction lie between 0.2 and 0.3 wt% Cu. Second, the addition of Cu to non-refined 6061 alloys (increase in the Cu content from 0.2 to 3.8 wt%) decreases the contraction onset temperature from about 605 °C to 585 °C. Third, adding grain refiners reduces the contraction onset temperature and the amount of linear contraction. Finally, grain refinement leads

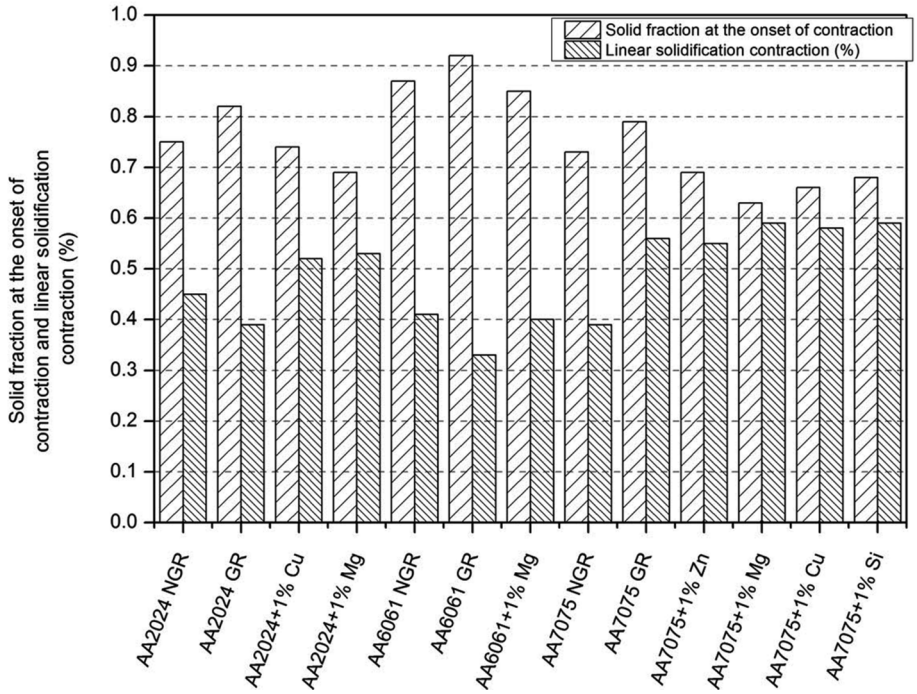

Fig. 3.9. Effect of grain refinement (GR) and alloying on the solid fraction at the onset of contraction and total linear solidification contraction for some commercial aluminium alloys. NGR is the non-grain-refined alloys [72,75].

to a larger pre-shrinkage expansion, which partly compensates for the following linear contraction. The much larger pre-shrinkage expansion for grain-refined alloys can be explained as follows. Grain-refined alloys consist of fine, equiaxed grains, which tend to bridge at a relatively high solid fraction, i.e., they have a low linear contraction onset temperature. Consequently, more time is taken before the linear contraction begins, which leads to higher expansion. Additionally, gas precipitates with relative ease from the melt since small grains have a larger interfacial area. The larger pre-shrinkage expansion often corresponds to a larger porosity. Moreover, the alloy that exhibits a smaller linear contraction during solidification often exhibits a larger interdendritic porosity [74].

Table 1 shows the contraction behaviour of different series of commercial aluminium alloys [72]. Thermal contraction does not occur in the case of AA1050, which is expected owing to its extremely narrow solidification range. The AA5182 and AA6082 alloys exhibit negligible contraction, which only starts at temperatures below the equilibrium solidus. The AA2024 and AA7075 alloys, which are more prone to hot tearing, demonstrate the larger linear contractions during solidification.

Similar investigations have been performed to study the effect of grain refinement and alloying on the contraction behaviour of several commercial alloys [72,75]. The results are shown in Fig. 3.9. Note that the solid fraction at the contraction onset and amount of linear contraction is smaller and larger, respectively, than the corresponding results in Table 1. This is attributed to the effect of different cooling rates (2–5.5 K/s in Fig. 3.9 and 12–18 K/s in Table 1). As can be seen from Figs. 3.6 and 3.9, grain refinement increases and decreases the solid fraction corresponding to the linear contraction onset and the amount of linear solidification contraction, respectively, except for the AA7075 alloy. This unusual phenomenon for the AA7075 alloy has also been observed in the case of the addition of a small amount of Zr and/or Mn to Al-Zn-Mg alloys [75]. One possible explanation is due to the measurement errors. Further investigations are needed, especially since this alloy is highly sensitive to hot tearing [7].

The effect of grain refinement on the contraction behaviour of an AA7050 alloy and its hot tearing susceptibility was systematically studied by Li et al. [26], as shown in Figs. 3.10 and 3.6. With moderate additions of the Al-5Ti-1B master alloys, the microstructure becomes finer and more equiaxed, which notably decreases the temperature corresponding to the onset of the linear contraction. In addition, the amount of linear contraction, and hot tearing susceptibility of the alloy decrease with the addition of the grain refiner. Excess addition of the Al-5Ti-1B master alloys will make the temperature of the contraction onset fluctuate, increase the linear contraction slightly, and affect the hot tearing resistance detrimentally because of the agglomeration of the secondary phase particles from the Al-5Ti-1B master alloys [26]. Zhang et al. [73] surveyed the effect of grain refinement on the contraction behaviour of AA7050 alloys. In contrast from Ref. [26], the grain refiners used in this study were Al-Ti master alloys with no boron. It was observed that grain refinement decreased the temperature corresponding to the linear contraction onset and the amount of linear contraction, while the negative influence of the excess addition of grain refiners did not occur as no agglomeration of the inoculant particles occurred.

Bai et al. [76] reported that the amount of linear contraction well corresponds to the hot tearing susceptibility in four commercial 7XXX alloys. It was found that AA7055 has the highest hot tearing susceptibility and the largest linear contraction. As shown in Fig. 3.6, the orders of the hot tearing susceptibility and amount of linear contraction of four commercial alloys are the same, as follows:

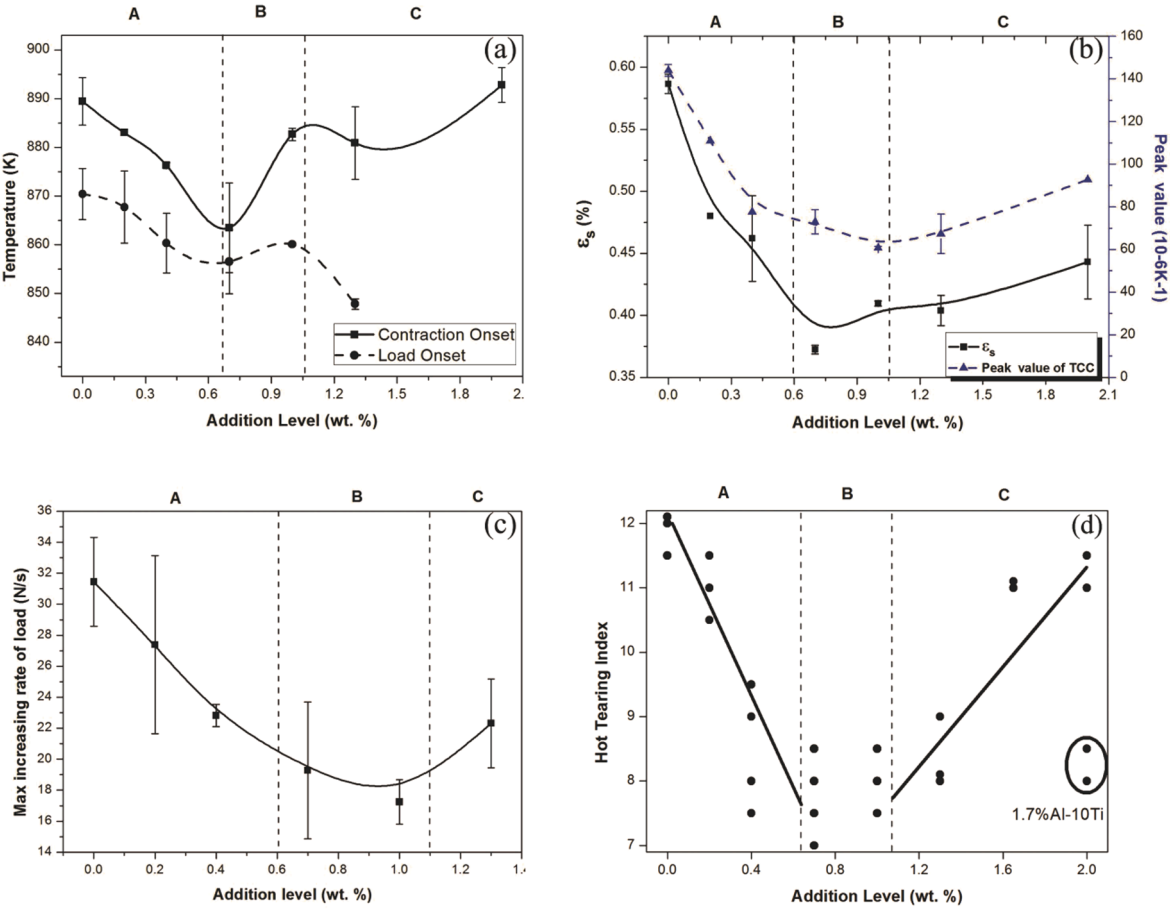

Fig. 3.10. Effect of the addition of Al-5Ti-1B on the contraction, load behaviour, and hot tearing susceptibility of AA7050 alloy: (a) the temperature corresponding to the contraction and load onset; (b) the linear contraction (ε_s) and the peak value of the TCC; (c) the maximum increasing rate of load; (d) the hot tearing susceptibility [26].

Table 1
Linear contraction onset temperature (T^{th}), corresponding solid fraction (f_s^{th}), pre-shrinkage expansion (Δl_{exp}), and linear contraction during solidification (ε_{th}) for the five commercial aluminium alloys (the casting temperature is 720–730 °C, and cooling rate is 12–18 K/s) [72].

Alloy	T^{th}/°C (f_s^{th})	Δl_{exp}/%	ε_{th}/%
1050	657 (0.38)	0	0.03
2024	515 (0.875)	0.035	0.2
5182	528 (0.93)	0.08	0
6082	563 (0.95)	0.025	0.02
7075	525 (0.87)	0.03	0.27

AA7055 > AA7085 ≥ AA7050 > AA7022.

Nagaumi et al. [102] and Li et al. [26] surveyed the relationship between the peak value of the TCC and the hot tearing susceptibility of some commercial 7XXX alloys, as shown in Fig. 3.6. Li et al. [26] found that the moderate additions of Al-5Ti-1B master alloys decreased the peak value of the TCC and the hot tearing susceptibility of AA7050 alloys, while excess additions slightly increased the peak value of the TCC but seriously harm the hot tearing resistance (Fig. 3.10(b) and (d)). Nagaumi et al. [102] found that AA7050 has the largest peak value of the TCC, followed by AA7075 and AA7022. This ranking is consistent with the hot tearing rating from industrial DC casting practice.

As indicated in Fig. 3.6, many binary and commercial aluminium alloys have been investigated using the T-shaped displacement testing device shown in Fig. 2.8(a). Thus, these data can be compared with one another. However, there is a lack of data on the effect of minor elements on the linear contraction behaviour of different commercial aluminium alloys, like Fe and Si elements in AA7050 alloys. These minor elements primarily affect the morphology, distribution, and types of secondary phases precipitating at the late

stage of solidification. This could change the development of solid bridges and thus the linear contraction behaviour. In the future, the existence of an inverse relationship between the amount of linear contraction and hot tearing susceptibility must be examined.

The investigation of the linear contraction behaviour provides us three important parameters for a particular alloy, i.e., the amount of linear contraction, peak value of the TCC, and contraction onset temperature (solid fraction). The former two parameters can be used to rate the hot tearing susceptibility. As can be seen from Fig. 3.6, strong correlations exist between the two parameters and the hot tearing susceptibility for various binary and commercial aluminium alloys.

The third parameter enables the establishment of a constitutive equation pertaining to the thermal strain development upon solidification [74,75] to be included in a hot tearing criterion [63]. The constitutive equation, relating the macroscopic thermal strain rate $\dot{\varepsilon}_{th}$ to the solid fraction f_s and temperature T, is expressed as [74]:

$$\dot{\varepsilon}_{th} = \frac{1}{3}\psi(f_s)\beta_T \dot{T} I, \text{ with} \tag{3.4}$$

$$\psi(f_s) = \begin{cases} 0 & \text{for } f_s \le f_s^{th}, \\ \left(\dfrac{f_s - f_s^{th}}{1 - f_s^{th}}\right)^n & \text{for } f_s > f_s^{th} \end{cases}$$

where β_T is the volumetric thermal expansion coefficient, I is the identity tensor, $\dot{T}$ is the cooling rate, and n is a material parameter. The function $\psi(f_s)$ shows that no thermal strain is present above the contraction onset temperature. Below this critical temperature, the macroscopic thermal strain tends towards the thermal strain in a fully solid state as the solid fraction approaches unity. Furthermore, the value of n is determined as zero for most commercial aluminium alloys with the help of computer simulations of their thermal contraction behaviour [74,75]. This value indicates that the semi-solid materials exhibit complete solid behaviour as soon as the contraction onset point is reached. However, the value of n changes with an increase in the cooling rates or grain refinement for binary alloys [74,75]. The higher cooling rates and grain refinement in the case of Al–4 wt% Cu alloys are expected to decrease the contraction onset temperature and render the transition from the viscous (liquid) to elasto-plastic (solid) mechanical behaviour more gradual, as shown in Fig. 3.11.

3.2. Load behaviour during solidification

Using the devices shown in Figs. 2.7(a) and 2.8(b), the profiles of load vs time and temperature vs time can be obtained, and an example is shown in Fig. 3.12 [78]. Initially, no load response is observed because of the predominant presence of the liquid. With the evolution of solidification, the dendrite arms start to impinge. With further solidification, more dendrites appear close to one another so that the semi-solid materials achieves certain strength to transfer tensile stresses, which was confirmed by in situ observation by the improved CHT rig [70]. This load onset point is marked in Fig. 3.12. When solidification is completed, the load at the NES can be measured. In fact, a force drop is often observed in the obtained curve during solidification [26], which is attributed to the occurrence of hot tearing.

As shown in Fig. 3.13, the study on the load development behaviour generates two key parameters, i.e., the load onset temperature (solid fraction) and the load value at the NES. The load onset point can be applied to some hot tearing criteria [49,78]. The point is closely related to alloy compositions, grain size and grain morphology. For example, Li et al. [77,78] found that the load onset temperatures and corresponding solid fractions of non-grain-refined and grain-refined Al-xZn-2 Mg-2Cu alloys vary with the change in the Zn contents, as shown in Fig. 3.14(b). In addition, it was found that grain refinement notably decreases the load onset temperature for the AA6061 (Fig. 3.15) [66] and AA7050 alloys (Fig. 3.10(a)) [26]. Grain-refined alloys consist of finer and more equiaxed grains in which continuous dendritic networks are more difficult to form sufficient strength compared to that of non-refined alloys. Note that the measured load onset temperature is always lower than the linear contraction onset temperature using the same apparatus for the alloy having the same grain refiner level [26,103]. This is possible because the LVDT can move freely in the horizontal direction and can

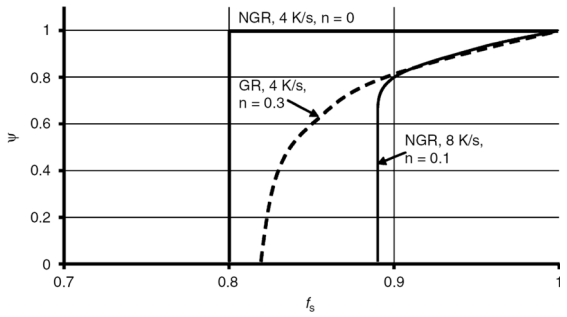

Fig. 3.11. Function $\psi(f_s)$ in Eq. (3.4) for Al–4 wt% Cu alloys. NGR = without grain refinement; GR = with grain refinement; cooling rates and the material parameter n are shown [7].

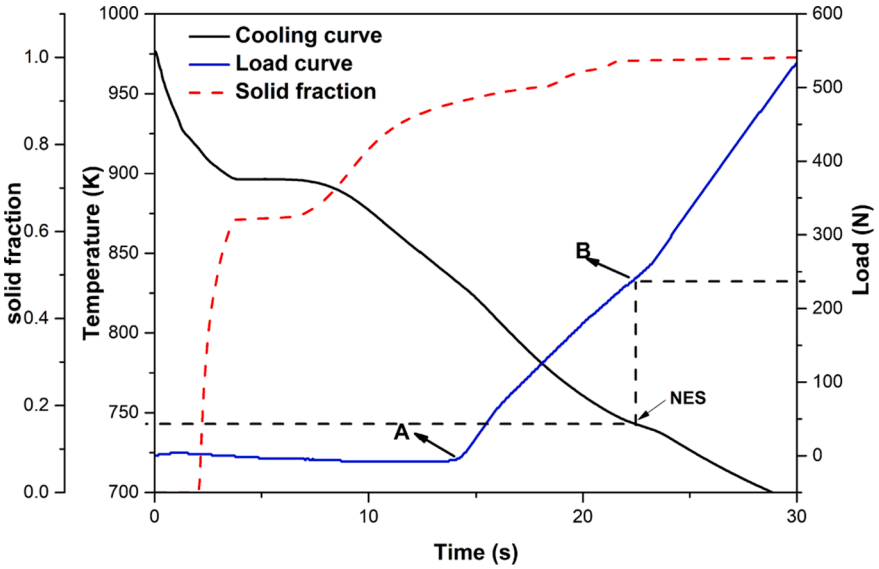

Fig. 3.12. Load evolution curve of grain-refined Al-2Zn-2 Mg-2Cu alloys [77]. The corresponding cooling and solid fraction curves are given. "A": load onset. "B": load value at the NES.

detect the start of movement due to shrinkage; nevertheless, the solid coalesced network, which can transfer tensile forces, is more difficult to form. This phenomenon has been observed for AA7050 (Fig. 3.10(a)) [26] and Al-Cu alloys [103].

Another key parameter, the load value at the NES, can be used to evaluate the hot tearing susceptibility, as shown in Fig. 3.13. If the load value at the NES is high, the hot tearing susceptibility is also high. This has been observed in Al-Cu [63], Al-Mg-Si [64,66], and Al-Zn-Mg-Cu (Fig. 3.14(a), (c), (e), and (g)) [77,78]. As mentioned previously, the hot tearing tendency relates to the linear contraction during solidification, and similarly the hot tearing susceptibility increases when the applied load increases. Li et al. [77] explained that a higher load value at the NES results in a smaller critical pore size above which hot tears will occur, resulting in a higher hot tearing susceptibility. The same explanation can be applied to the relationship between the linear contraction during solidification and hot tearing susceptibility. However, a contradicting conclusion was reported by Li et al. using a CRC mould [59,103]. It was found that the alloy having a higher hot tearing susceptibility exhibits a much lower load value at the NES [59,103]. It is thought that the occurrence of large hot tears releases more load, which leads to a lower load value at the NES in Refs. [59,103], while the occurrence of minor hot cracks does not release a notable load, as indicated in Refs. [63,64,66,78]. It is concluded that the higher load values at the NES indicate a higher hot tearing susceptibility in the absence of serious hot tears.

One special example is that in Al-0.52 Mg-0.34Si-xFe alloys [29], as shown in Fig. 3.13, the reduction in the hot tearing susceptibility with the addition of Fe content corresponds to a decrease in the solid fraction of load onset and an increase in the load at the NES, although no serious hot tears occur. This is explained as follows: a three-dimensional network of Fe-based intermetallics is generated at a higher Fe content, accelerating the earlier formation of the coherency and coalescence points, and leading to the higher load values at the NES and lower hot tearing susceptibilities at higher Fe contents. In Li et al.'s work on the addition of Si elements to Al-9Zn-2 Mg-2Cu-xSi alloys exhibits, a similar phenomenon was observed [104]. It was speculated that the addition of Si could promote the formation of solid bridges and coalescence of grains and thus lead to higher load values at the NES and lower hot tearing susceptibilities. However, the above-mentioned explanation lacks more reliable in situ observations and quantitative bridging development data. These can be realised by the 3D synchrotron X-ray micro tomography approach (Section 2.2.2) to directly observe the development of grain bridges or by the tensile tests upon solidification to indirectly determine the amount of grain boundary area covered by the liquid.

Furthermore, the load development can reflect the hot tearing susceptibility. Cao et al. [105] reported that the load dropping in an alloy with a low solute concentration corresponds to severe hot tearing. The occurrence of hot tears leads to the release of tensile stresses and thus the drop of the measured load. In contrast, for an alloy with a high solute concentration, the increase in the load is smooth, and no obvious drop can be observed, thereby indicating that hot tearing does not occur. This rating method has been used in other studies, such as Refs. [26,103,106].

The load behaviour characteristics during solidification are summarised in Fig. 3.13. Unlike the linear contraction behaviour shown in Fig. 3.6, the effects of minor elements have been investigated, although more efforts are needed. However, these load data were often obtained from different load testing devices so that they cannot be directly compared with one another. Thus, the development of a unified load testing device is recommended. Due to the functionality and simplicity of the linear contraction and load testing devices, such devices have been widely applied since 2004 and used to investigate the effect of the compositions (Figs. 3.6 and 3.13). However, the effect of different process parameters has not been studied due to the limited structure and configuration of these testing devices. A potential breakthrough is to develop a larger trial DC displacement/load testing machine to investigate more influencing factors and more closely mimic actual industrial conditions.

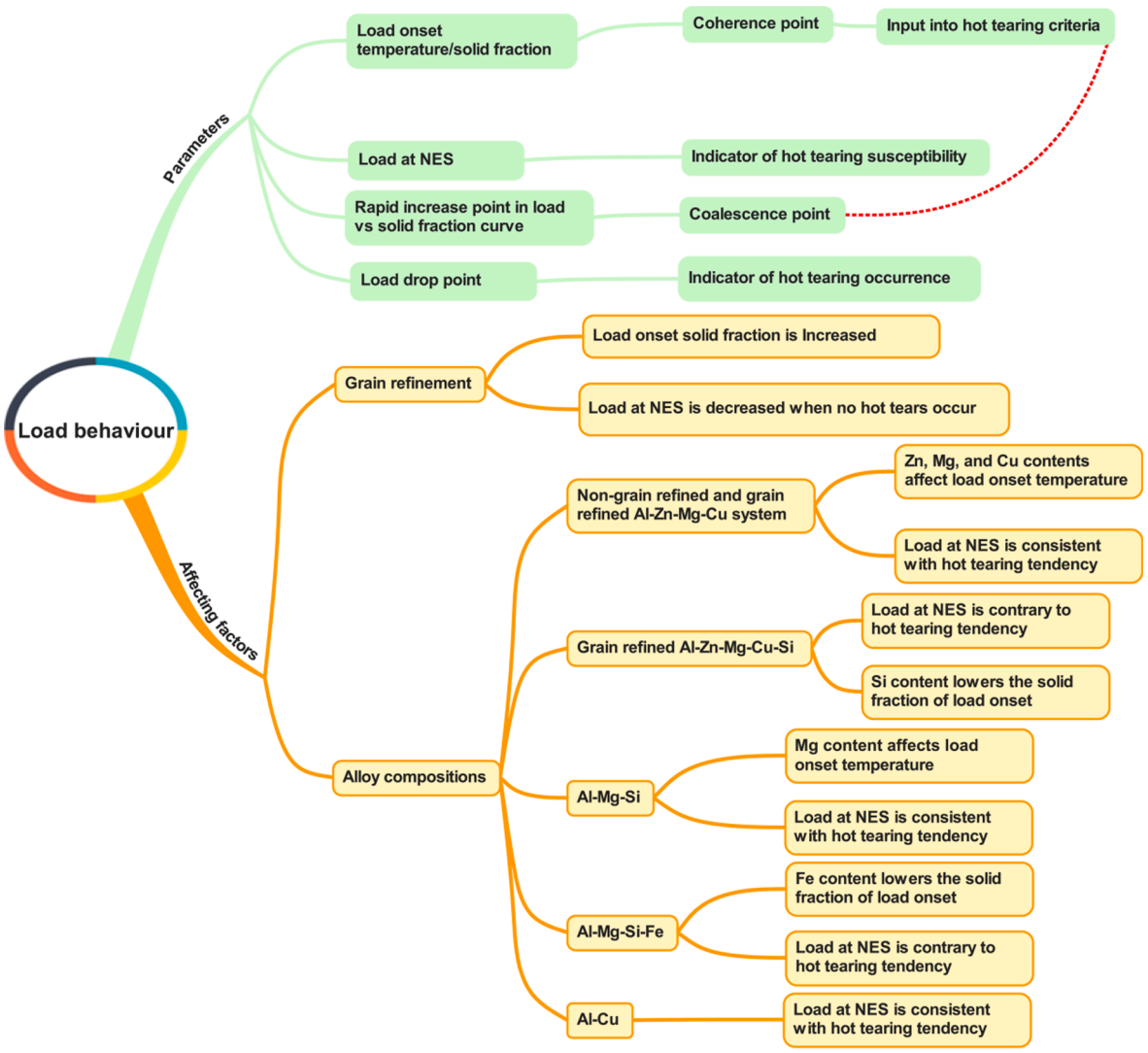

Fig. 3.13. An outline of the load behaviour during solidification, including the quantitative data obtained from the load curve during solidification and influence factors on the load behaviour.

The thermal contraction and load development upon solidification due to non-uniform cooling induce thermo-mechanical conditions that may promote the formation of hot tears. The mechanical strength of a semi-solid material may be sufficient to prevent failure. These physical properties, which are summarised in the following section, considerably influence the accuracy and ultimate success of the semi-solid constitutive models [18,20,21,41] and hot tearing criteria [15,23]. As mentioned in Section 2.1, the mushy zone mechanical properties obtained using different tensile testing methods must be distinguished when simulating different casting processes. Most relevant is to assess whether near-equilibrium solidification occurs during the investigated casting process. The isothermal tensile test upon solidification is preferred for non-equilibrium solidification such as the DC casting process.

3.3. Mushy zone mechanical properties of aluminium alloys

For the semi-solid materials, strength means the resistance of the mushy zone to deformation or fracture. Fig. 3.16(a) exhibits a typical semi-solid tensile curve, which describes the relationship between the UTS (i.e., the maximum stresses to fracture) and solid fraction. The UTS initiates from a low solid fraction or high temperature termed as the ZST and develops gradually upon solidification. In contrast, the ductility represents the amount of deformation that the mushy zone can undertake before complete fracture. The curve of the semi-solid ductility versus the temperature/solid fraction has a typical U-shape like Fig. 3.16(b) with a specific temperature or solid fraction range where the ductility is considerably lower than its neighbours [15,34,41]. This can be considered as a ductile-brittle-ductile transition. This range is defined as the BTR. At low solid fractions, a large amount of liquid exists to prevent the formation of hot tears and the ductility is large. This mechanism has been observed by in situ 3D X-ray micro tomography [83]. At high

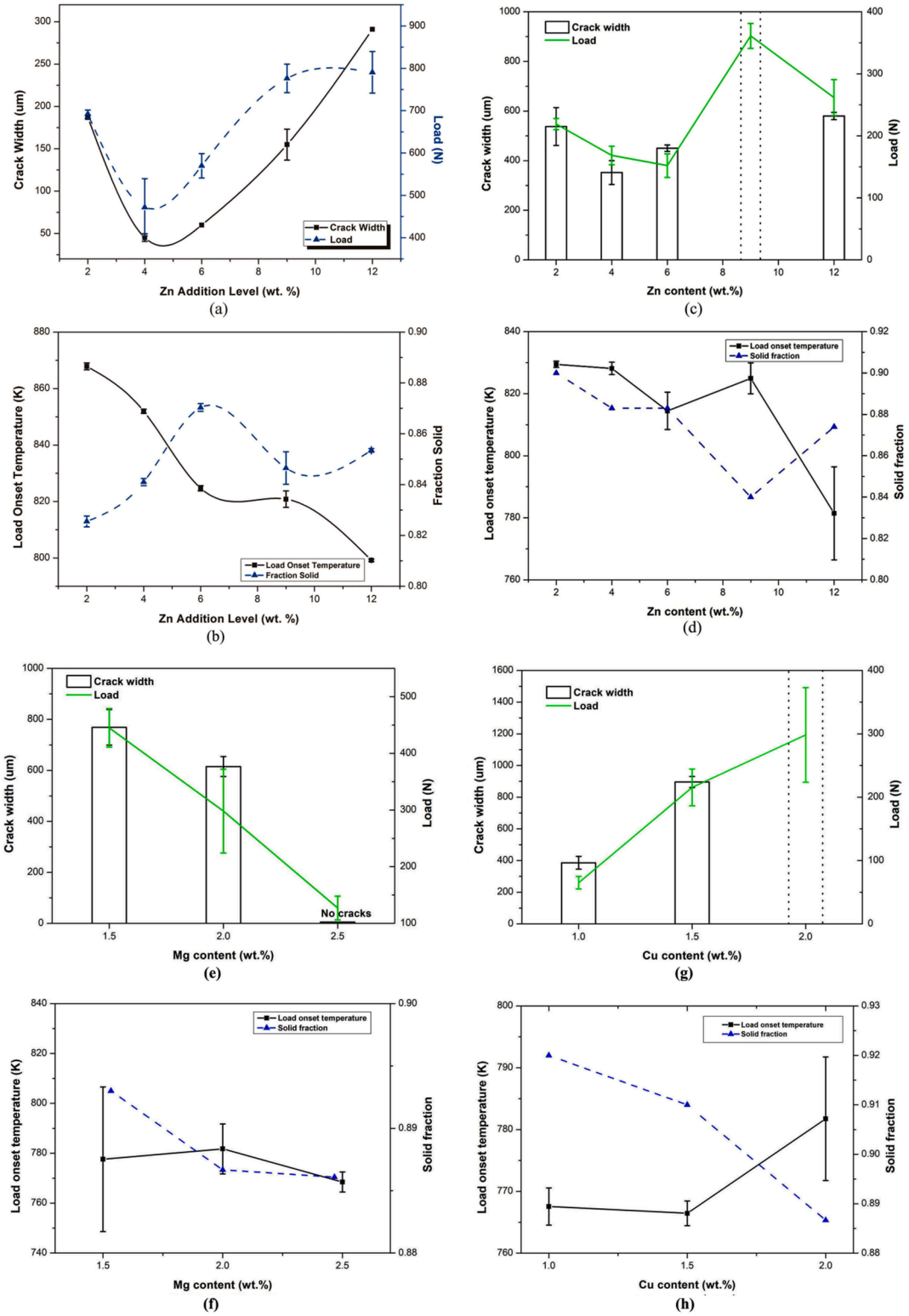

Fig. 3.14. Load behaviour during solidification of non-grain-refined Al-xZn-2 Mg-2Cu alloys (a, b) as well as grain refined Al-xZn-2 Mg-2Cu alloys (c, d), Al-9Zn-yMg-2Cu alloys (e, f), and Al-9Zn-2 Mg-zCu alloys (g, h): (a, c, e, and g) maximum crack width and load measured at the NES; (b, d, f, and h) load onset temperatures and the corresponding solid fractions [77,78].

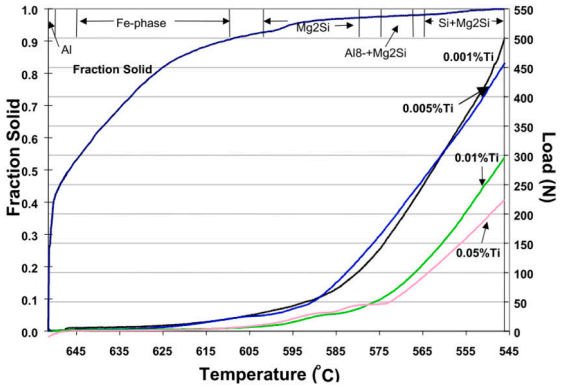

Fig. 3.15. Load development of AA6061 alloys during solidification with different Ti contents. Corresponding solid fraction curve and phase formations as a function of temperature are given [66].

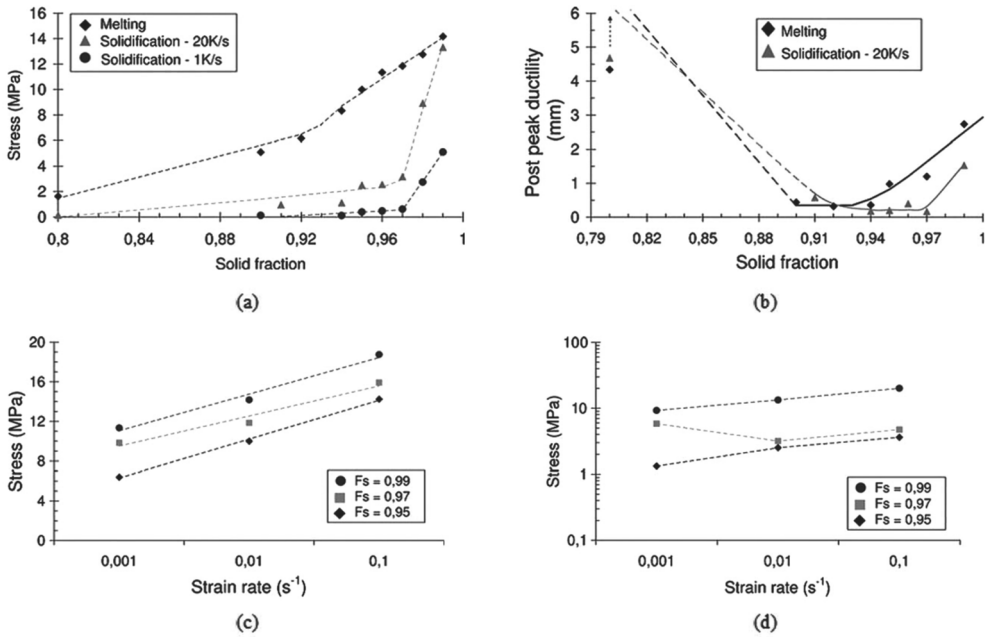

Fig. 3.16. Variations of (a) peak stress (i.e., UTS) and (b) post peak ductility (post peak ductility is the displacement from peak stress to fracture) of AA6061 alloy versus solid fraction under different testing methods; variations of peak stress versus strain rate under (c) melting and (d) solidification conditions [34].

solid fractions, the mushy zone behaves similar to a solid and exhibits a large ductility. In the BTR, the solid bridges have not been formed sufficiently to prevent crack propagation and the remaining liquid phases are limited to heal cracks. In Refs. [36,39,42,45,107,108], a shape like Fig. 3.17(b) with a ZDT was reported. It is believed that the ZDT point should correspond to the lower boundary of the BTR. The disappearance of the upper boundary is because the insufficient liquid is present to accommodate the deformation in the tensile testing cases [41].

The strength and ductility of semi-solid aluminium alloys are mainly influenced by the grain size and morphology, cooling rate, strain rate, initial state, and alloy composition. The reported studies on these factors are summarised sequentially in the following text. Unless indicated explicitly, the testing device is a Gleeble or Instron series tensile tester.

3.3.1. Factors influencing the strength and ductility of semi-solid aluminium alloys

3.3.1.1. Effect of the testing method on the strength and ductility of semi-solid aluminium alloys. First, it should be reiterated that the semi-solid mechanical properties of the same alloy are often different under the reheating and solidification conditions. For example, Giraud et al. [34] measured the semi-solid tensile strength and ductility of AA6061 alloy under the melting (i.e., reheating) and solidification conditions as shown in Fig. 3.16. A transition point, where the peak stress increases rapidly under the melting condition, is observed at

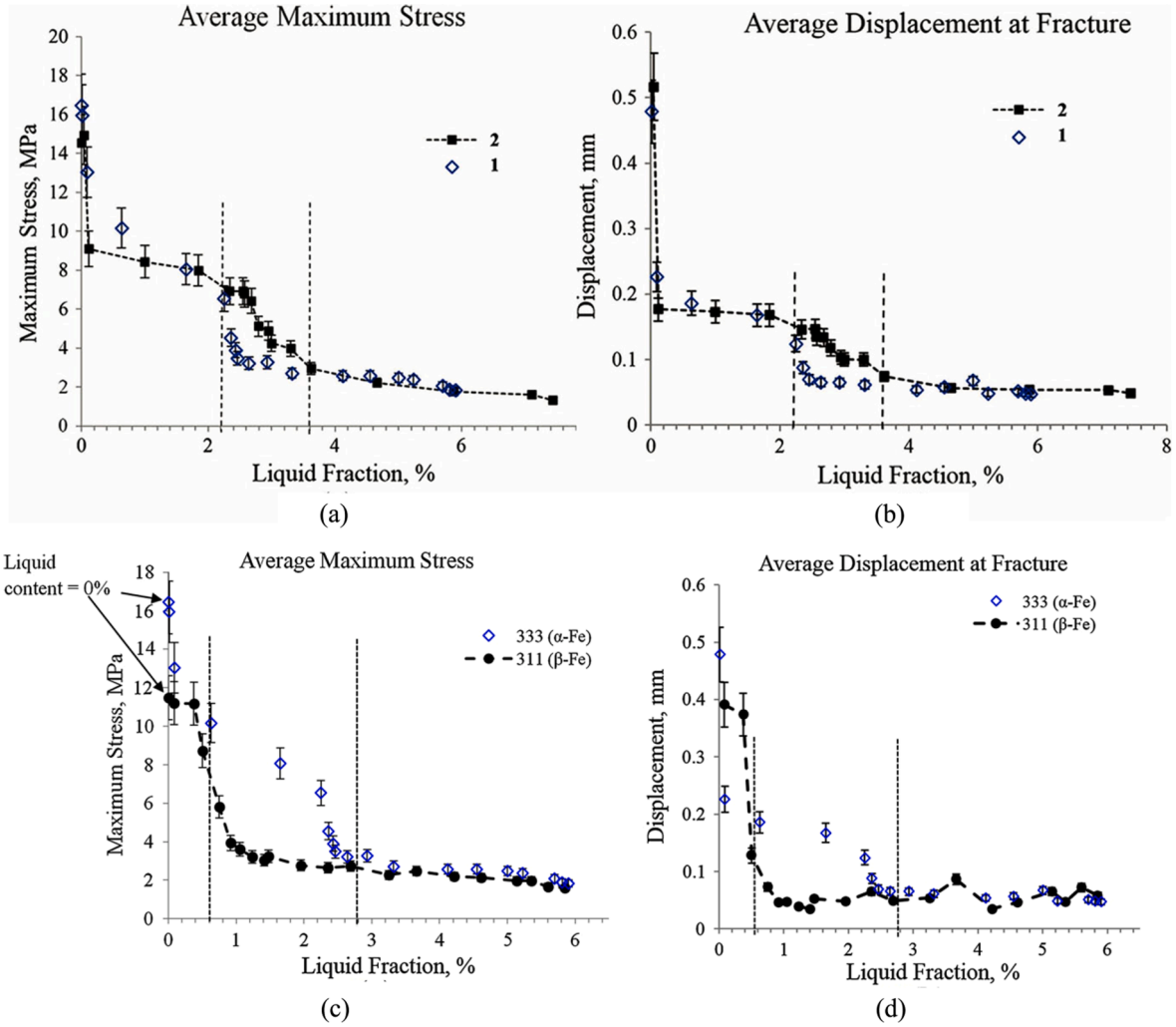

Fig. 3.17. (a) Maximum stress (i.e., UTS) and (b) displacement at fracture of Al-Cu 206 cast alloys containing 0.3 wt% Si and 0.3 wt% Mn ("Alloy 333") versus liquid fraction (1, no refiners; 2, adding 0.4 wt% Al-5Ti-1B alloys); comparison of (c) maximum stress and (d) displacement at fracture of "Alloy 333" and "Alloys 311" (Al-Cu 206 cast alloys containing 0.1 wt% Si and 0.1 wt% Mn) versus liquid fraction [36]. The tests were performed upon reheating.

the solid fraction of 0.93 in Fig. 3.16(a). This transition point is delayed to 0.97 under the solidification condition and the corresponding peak stress values are smaller. It is believed that the point corresponds to the transition between discontinuous (pockets) and continuous (films) liquid distributions. Above the transition point, only liquid pockets are present and numerous solid bridges begin to form, which leads to the rapid increase in the mushy zone strength. Under the melting condition, the liquid phases spread along grain boundaries only when solid bridges begin to re-melt. Under the solidification condition, the liquid films initially exist along grain boundaries and only vanish with the formation of solid bridges. Obviously at the same solid fraction more liquid films are present in partially solidified materials than in partially remelted materials. Hence, the transition solid fraction is higher under the solidification condition. The transition points where the strength rapidly increases for various commercial aluminium alloys are listed in Table 2. They are closely related to the grain bridging/coalescence phenomenon, which are the essential input for hot tearing simulations and hot tearing criteria. It has been pointed out that the value of the coalescence point significantly affects the final hot tearing predictions [64,78].

Additionally, the peak stresses are always larger under the melting condition than under the solidification condition for the same solid fraction (Fig. 3.16(a)), as also reported by Fabregue et al. [41]. This can be attributed to the shift of the transition point from 0.93 (melting) to 0.97 (solidification), which suggests that solid bridges occur earlier under the melting condition [34,41]. In terms of the ductility (Fig. 3.16(b)), the BTR is delayed from between 0.9 and 0.94 under the reheating condition to between 0.94 and 0.97 under the solidification condition because continuous liquid films last for a shorter period and solid bridges occur earlier under the reheating condition.

In summary, a reliable semi-solid mechanical property testing method must able to reproduce the microstructure evolutions

Table 2
Tensile properties of some commercial aluminium alloys.

Alloy	Zero strength temperature and/or solid fraction	Zero ductility temperature and/or solid fraction	Point where strength rapidly increases	Ref.
2XXX				
2618	610 °C	–	~545 °C	[15]
2024	$f_s = 0.76$	–	–	[15]
2024	–	495 °C (as-cast) 530 °C (deformed)	–	[15]
Al-Cu-Li				
Al-6 wt% Cu-1.2 wt % Li	610 °C	–	~530 °C	[15]
3XXX				
3004	$f_s = 0.81(0.003\ s^{-1})$	–	–	[15]
3104	600 °C ($f_s = 0.93$)	–	–	[18]
3104	615 °C ($f_s = 0.95$) (~10^{-4} s^{-1}); 620 °C (~10^{-3} s^{-1});	615 °C ($f_s = 0.95$) (~10^{-4} s^{-1}); 610 °C (~10^{-3} s^{-1})	–	[39]
CA31218	630 °C ($f_s = 0.88$) (10^{-4} and $10^{-3}s^{-1}$)	630 °C ($f_s = 0.88$) (~10^{-4} s^{-1}); 610 °C (~10^{-3} s^{-1})	–	[39]
5XXX				
5456	570 °C(as-cast and deformed)	–	–	[15]
5182	580 °C ($f_s = 0.93$) (~10^{-4} s^{-1}); 575 °C ($f_s = 0.94$) (~10^{-2} s^{-1})	570 °C ($f_s = 0.94$) (~10^{-4} s^{-1}) to 562 °C ($f_s = 0.97$) (~10^{-2} s^{-1})	575–570 °C ($f_s \approx 0.95$)	[42]
5182	580 °C ($f_s = 0.93$) (~10^{-4} and 10^{-3} s^{-1})	–	–	[18]
5182	570 °C (as-cast) 570 °C (HIP) ($10^{-3}s^{-1}$)	548 °C (as-cast) 565 °C (HIP) ($10^{-3}s^{-1}$)	–	[40]
5182	570 °C (0.02 mm s^{-1})	–	548 °C ($f_s = 0.94$)	[20]
6XXX				
6111	580 °C ($f_s = 0.98$) (10^{-4} and $10^{-3}s^{-1}$)	560 °C ($f_s = 0.985$) (~10^{-4} s^{-1}); 530 °C (~$10 - 3$ s^{-1})	–	[39]
6061	$f_s = 0.8$, 20 K/s $f_s = 0.9$, 1 K/s	–	$f_s = 0.97$(1 and 20 K/s) $f_s = 0.93$ (reheating)	[34]
HS50	620 °C ($f_s = 0.7$)	612 °C ($f_s = 0.77$)	–	[107]
HS60	620 °C ($f_s = 0.69$)	610 °C ($f_s = 0.77$)	557 °C ($f_s = 0.9$)	[45]
7XXX				
7075	$f_s = 0.92$	–	$f_s = 0.95$	[15]
7075	570 °C	–	480–500 °C	[15]
7075 (extruded state)	550 °C ($f_s = 0.98$)	519 °C ($f_s = 0.997$)	–	[37]
7064	545 °C	–	470 °C	[15]
7039	600 °C	–	–	[15]
7005	630 °C (L) (reheating)	610 °C (L) (reheating)	–	[15]
7475	600 (ST)-610 (L) °C (reheating) 535 (L)-550 (ST) °C (solidification)	530 (ST)-550 (L) °C (reheating)	–	[15]
7050	550 °C ($f_s = 0.85$) (0.2–2.0 mm/min)	475 °C ($f_s = 0.94$) (0.2–2.0 mm/min)	475 °C ($f_s = 0.94$) (0.2–2.0 mm/min)	[38]

occurring at the last stage of solidification as much as possible, especially in terms of the grain size and morphology, liquid distributions at the last stage of solidification, as well as the grain bridging/coalescence. Thus, different data from different tensile testing methods cannot be applied to different casting processes.

3.3.1.2. Effect of the grain refinement on the strength and ductility of semi-solid aluminium alloys. Adding grain refiners is mostly used to achieve fine equiaxed grains while it has little effect on the SDAS [109]. Generally, adding grain refiners increases the strength and ductility of semi-solid aluminium alloys. The increased strength is attributed to the increasing numbers of solid bridges between fine grains, while the improved ductility occurs mainly due to the easier intergranular slide and grain rotation among fine grains. For example, Bolouri et al. [36] studied the effect of grain refinement on the strength and ductility of semi-solid Al-Cu 206 cast alloys upon reheating. As shown in Fig. 3.17, grain refinement notably improved the UTS and displacement at the liquid fractions between 2.2% and 3.6%. The positive effect of grain refinement on the UTS was also observed in Al-10 wt% Mg and low-copper (Al-1.5 wt% Cu) alloys (Fig. 3.18(a) and (b)) [15]. However, a contrasting tendency was observed at high-copper alloys (Al-7 wt% Cu), as shown in Fig. 3.18(c) [15]. A convincing explanation is that continuous liquid films exist at grain boundaries in high Cu contents, and the grain-refined alloys having more grain boundaries will form a weaker solid skeleton to withstand tensile forces compared to that in the case of non-refined alloys, i.e., the formation of grain bridging/coalescence is delayed. In other words, grain refinement is beneficial in

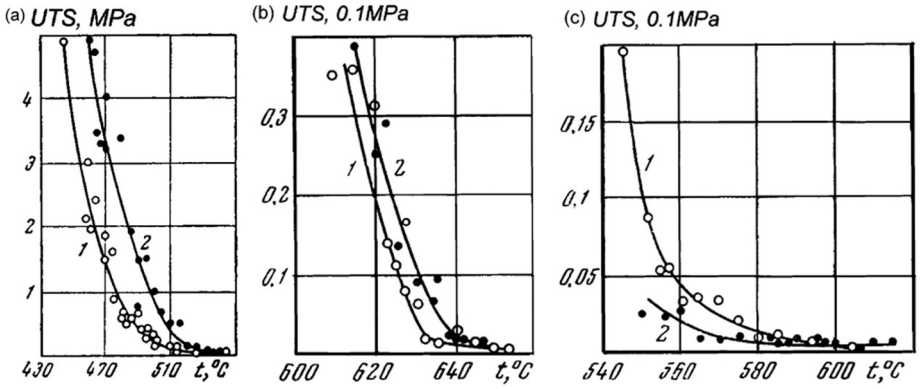

Fig. 3.18. Variance of UTS with temperature of (a) Al-10 wt% Mg alloys (1, no refiners; 2, adding 0.1 wt% Ti, 0.1 wt% Be, and 0.1 wt% Zr), (b) Al-1.5 wt% Cu alloys (1, no refiners; 2, adding 0.1 wt% Ti), and (c) Al-7 wt% Cu alloys (1, no refiners; 2, adding 0.3 wt% Mn and 0.1 wt% Ti) [15]. Note that a tensile testing device in Fig. 1a from Ref. [15] was used under the reheating condition.

improving the mushy zone tensile strength for most aluminium alloys, although the opposite phenomenon may occur when large amounts of liquid film exist at grain boundaries for some specific aluminium alloys.

Grain refinement has little effect on the ZST (Figs. 3.17(a) and 3.18), while the change of grain morphology and grain size affects the boundaries of the BTR and ZDT. A columnar structure or coarse grains have a higher upper boundary temperature in Al-Cu alloys (Fig. 3.19). By comparison, the change of the lower boundary and ZDT is complex. Mostly, columnar or coarse grains shift this boundary to higher temperatures (Fig. 3.19(c)) because an intergranular fracture occurs with a higher resistance in this kind of

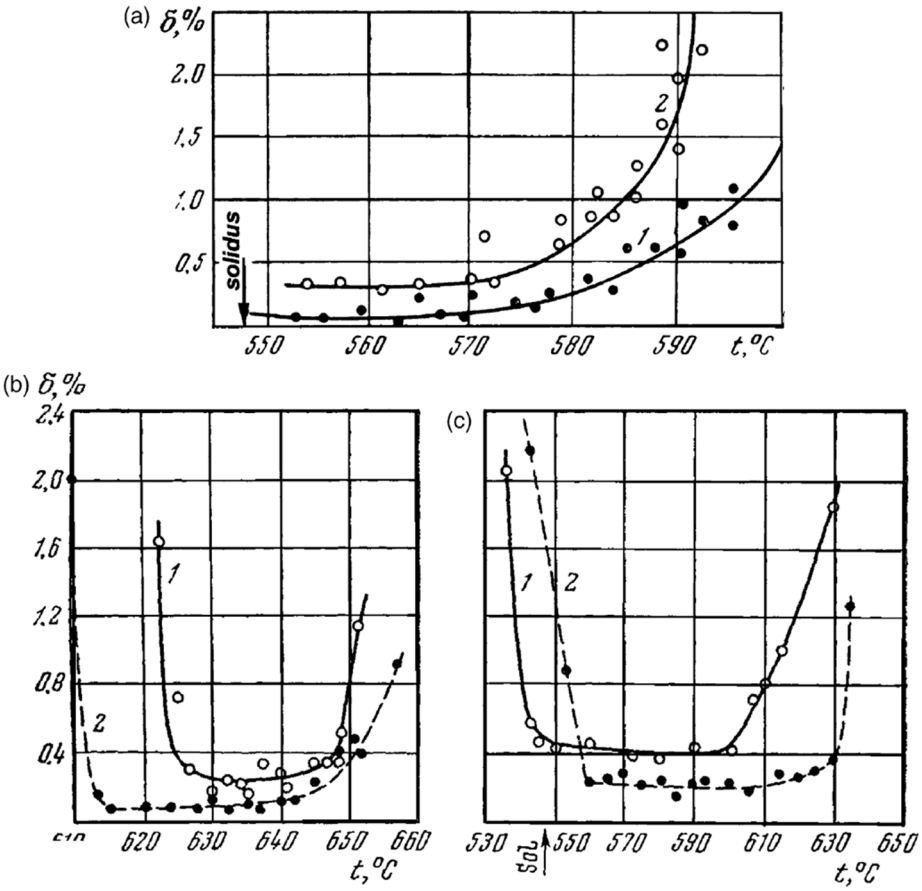

Fig. 3.19. Effect of grain size and morphology on semi-solid elongation (δ) of (a) Al–4 wt% Cu (1, coarse grains; 2, fine grains), (b) Al–1.5 wt% Cu and (c) Al–5 wt% Cu (1, equiaxed grains; 2, columnar grains) alloys [15]. The testing method is the same as that used in Fig. 3.18.

structure. Nevertheless, a contrasting tendency is observed when the surface of the columnar or coarse grains is smooth (Figs. 3.17(b) and 3.19(b)).

In the future, attention should be focused on investigating the effect of fine granular grains on the strength and ductility of semi-solid materials. It is worth investigating whether the fine grain sizes and smooth surfaces will delay the formation of bridging/coalescence and thus harm the material's semi-solid tensile strength. The aggregation of inoculant particles due to excess additions of grain refiners needs to be noticed particularly in this survey.

3.3.1.3. Effect of the cooling rate on the strength and ductility of semi-solid aluminium alloys. Tensile tests must be performed upon solidification to investigate the effect of the cooling rate. Giraud et al. [34] measured the semi-solid tensile strength of AA6061 alloy at cooling rates of 1 and 20 K/s. As shown in Fig. 3.16(a), the higher the cooling rate, the larger the UTS. Moreover, the solid fraction corresponding to the ZST is shifted to a lower value, while the cooling rate does not influence the solid fraction point where the ZST starts to increase rapidly (Table 2). Generally speaking, increasing the cooling rate will refine grains and decrease SDAS [110]. The higher the cooling rate, the finer the grain size, and thus there are more grain boundaries to form a stronger solid skeleton. Moreover, the SDAS becomes finer at higher cooling rate. Thus, the distribution of the liquid films becomes more homogenous and thinner between grains, favouring the development of strength.

As compared to the strength, it is more difficult to measure the semi-solid ductility at a high cooling rate. However, there are still some reports about the effect of the cooling rate on the semi-solid ductility in binary aluminium alloys[15]. The effects of the cooling rate on the semi-solid ductility in Al-Cu and Al-Si alloys are shown in Fig. 3.20. Slower cooling shifts the lower boundary of BTR to a lower temperature. The slower cooling rate makes the surface of grains smoother, and the transition from intergranular to intragranular fracture occurs at a lower temperature. In Al-1.5 wt% Cu and Al-0.7 wt% Si alloys with a small amount of non-equilibrium eutectic liquid, the lower boundary of the BTR is well above the NES under the low cooling rate (Fig. 3.20(a) and (c)). With the increase in the cooling rate, grains become more dendritic, and the lower boundary of the BTR is close to the equilibrium solidus. For Al-5 wt% Cu and Al-5 wt% Si alloys with large amounts of non-equilibrium eutectic liquid, the alloys are brittle during the entire solidification range, and the lower boundary of the BTR even is below the NES (Fig. 3.20(b) and (d)) due to the extremely weak Al/Al_2Cu or Al/Si

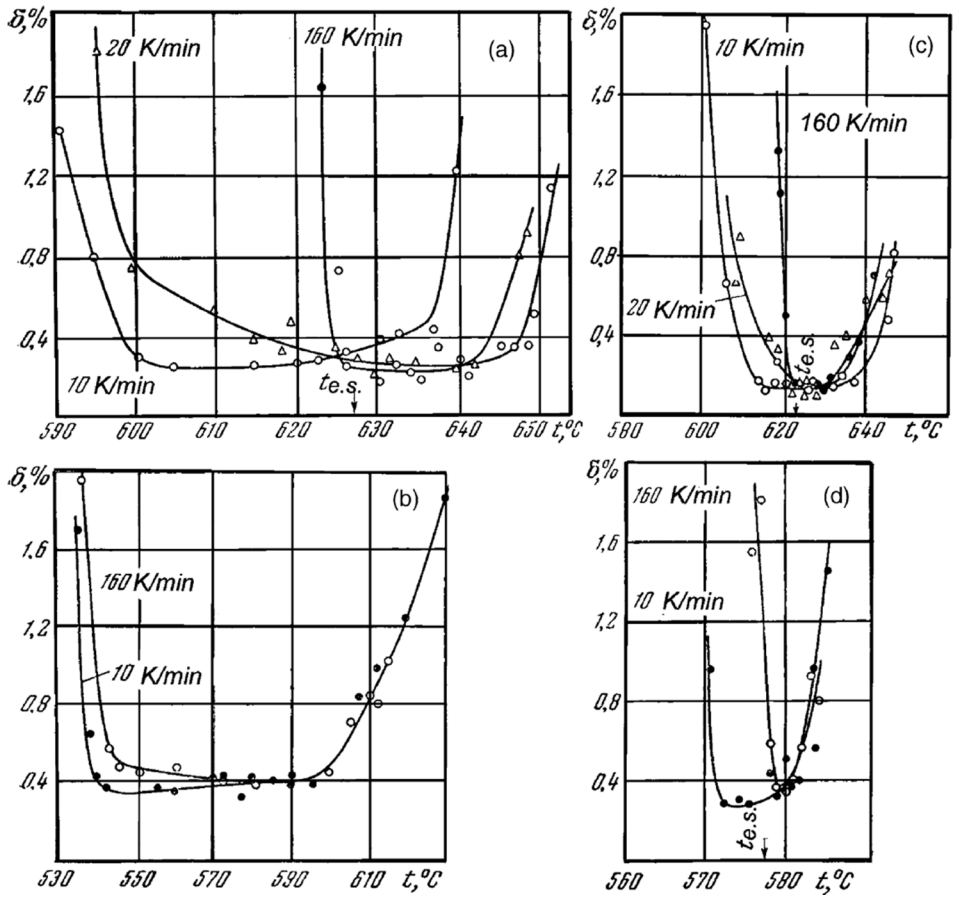

Fig. 3.20. Effect of cooling rate on the semi-solid elongation (δ) of (a) Al-1.5 wt% Cu, (b) Al-5 wt% Cu, (c) Al-0.7 wt% Si, and (d) Al-5 wt% Si. $t_{e.s.}$ is the equilibrium solidus, and the NES is 548 and 577 °C for Al-Cu and Al-Si alloys, respectively [15]. The testing method is the same as that used in Fig. 3.18.

interfaces. Although the position and range of the BTR depend on the cooling conditions, the elongation in the BTR remains virtually unaffected (Fig. 3.20). It can be explained as follows: on one hand, with the cooling rate decreasing, the liquid layers thicken, which impairs the elongation. On the other hand, the liquid layers become less continuous, which improves the elongation. Finally, the two opposing factors counteract each other. These two factors (testing upon solidification and high cooling rates) make relevant semi-solid studies highly challenging, especially in terms of the investigation of the semi-solid ductility of commercial aluminium alloys. Future work should be focused on improving this situation.

3.3.1.4. Effect of the strain rate on the strength and ductility of semi-solid aluminium alloys. Apart from testing methods and cooling rates, Giraud et al. [34] measured the semi-solid strength of AA6061 alloys at different strain rates. These data have been used to obtain relevant parameters for two semi-solid constitutive models (Section 5.1.1). As shown in Fig. 3.16(c), the UTS increases with an increase in the strain rate under the melting condition. The strain rate sensitivity can be derived from the slope of the curves as being equal to 0.13. The same tendency can also be found under the solidification condition (Fig. 3.16(d)) which the strain rate sensitivity is 0.17, except at a solid fraction of 0.97. Similar phenomena at the same solid fraction were found in AA6056 alloys upon reheating (Fig. 3.21 (a)) [41]. The unique behaviour at the solid fraction of 0.97 corresponds to the point where the strength increases rapidly (Fig. 3.16(a)) with a minimum ductility value (Fig. 3.16(b)). At this solid fraction, grains come into contact by the grain bridging, and consequently, the elasto-plastic mechanical behaviour of the semi-solid body becomes dominant. Moreover, different authors have reported on the correspondence of the higher strain rates to higher semi-solid UTS at high solid fractions, such as AA5182 (Fig. 3.22(a)) [42], AA3104 and AA5182 (Fig. 3.23) [18], AA3104, AA6111, and CA31218 (Fig. 3.24) [39], and AA7050 (Fig. 3.25) [38] alloys. This phenomenon occurs because the liquid concentrates at the triple junctions at higher strain rates, leading to more solid bridges and higher strength. At lower strain rates the liquid film spreads over the grain boundaries resulting in fewer bridges and thus a lower strength [42]. However, it can be observed from Figs. 3.22–3.25 that the alloys exhibit a nearly zero strain rate sensitivity at low solid fractions. In particular, the change in the strain rate has no obvious effect on the ZST for most aluminium alloys (Table 2). This is due to the existence of continuous liquid films along grain boundaries at such high liquid fractions regardless of the change in the strain rate.

The effect of the strain rate on the ductility of semi-solid aluminium alloys is closely related to the amount of final eutectic liquid and the occurrence of creep. Novikov [15] reported the elongation of semi-solid Al-Cu and Al-Si alloys at different strain rates, as shown in Fig. 3.26. The variation in the strain rates does not notably influence the two boundaries of the BTR; however, as the strain rates increase, the elongation in the BTR decreases for semi-solid Al–5 wt% Si and Al–6.5 wt% Cu alloys, which have a large amount of eutectic liquid. This is because the strain accommodation by the eutectic liquid occurs more easily at low strain rates. A similar tendency was observed in the AA5182 [42]. In contrast, no obvious change in the elongation in the semi-solid Al–0.7 wt% Si and Al–1.5 wt% Cu alloys can be observed due to the limited amount of eutectic liquid. Interestingly, Giraud et al. [34] reported that in AA6061, upon solidification, the ductility in the BTR increases with an increase in the strain rates. A similar tendency was observed in the Al-Cu alloys by Qingchun et al. [15] and Wisniewski [15]. This difference can be attributed to the occurrence of creep and strain accommodation by the redistribution of the liquid. In the latter scenario, creep does not take place and some micro-cracks are generated in the castings, which leads to less localised deformation and high ductility at high strain rates. Moreover, Colley et al. [42] found that the increase in the strain rate decreases the ZDT in AA5182 alloys, as shown in Fig. 3.22(b) and Table 2. The ductility at high solid fractions is more sensitive to the strain rate. A similar phenomenon was observed in the case of AA3104, AA6111, and CA31218 alloys [39] (Fig. 3.24 and Table 2).

In summary, the effect of the strain rates on the semi-solid strength and ductility, to establish the constitutive equations, has been widely reported to realise hot tearing simulations. The strength is mainly related to the distributions of the liquid among grain

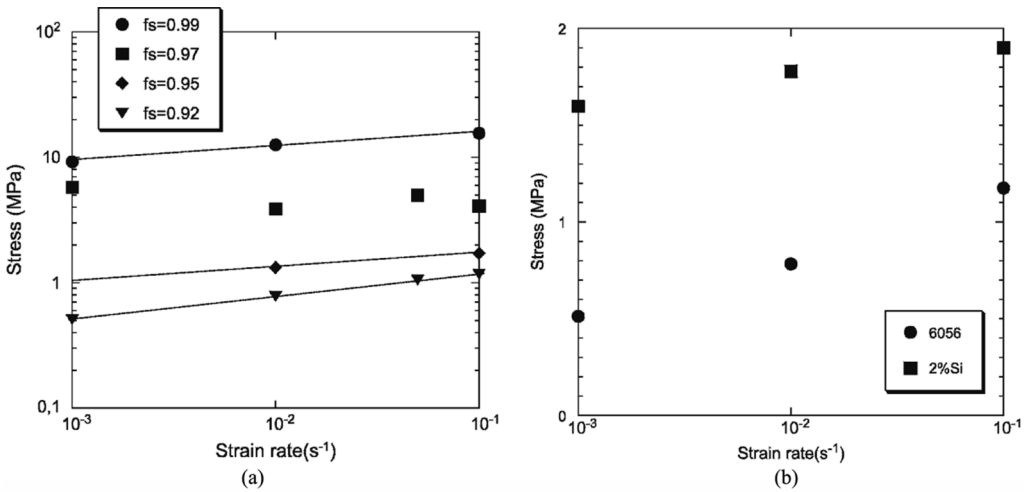

Fig. 3.21. (a) Maximum stress (i.e., UTS) versus strain rate at different solid fractions (f_s) for AA6056 alloys upon reheating, (b) maximum stress versus strain rate at the solid fraction of 0.9 for AA6056 alloys and the alloys with 2 wt% Si [41].

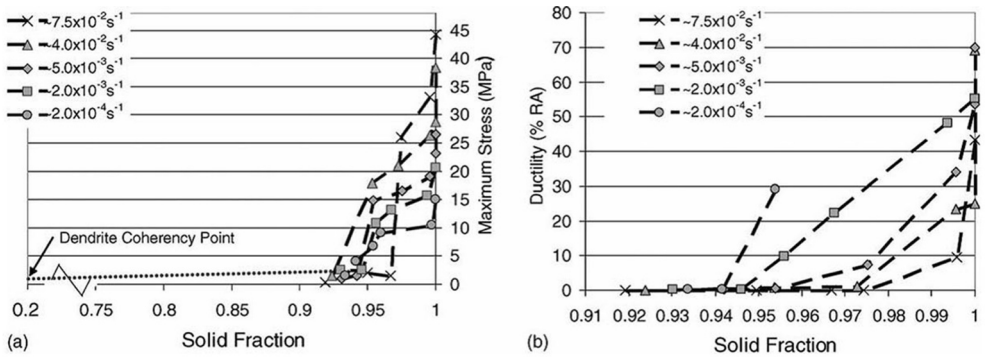

Fig. 3.22. (a) Variation of the maximum stress and (b) ductility (diametric strain) with the solid fraction at different strain rates upon reheating for AA5182 alloys [42]. The tests were performed upon reheating.

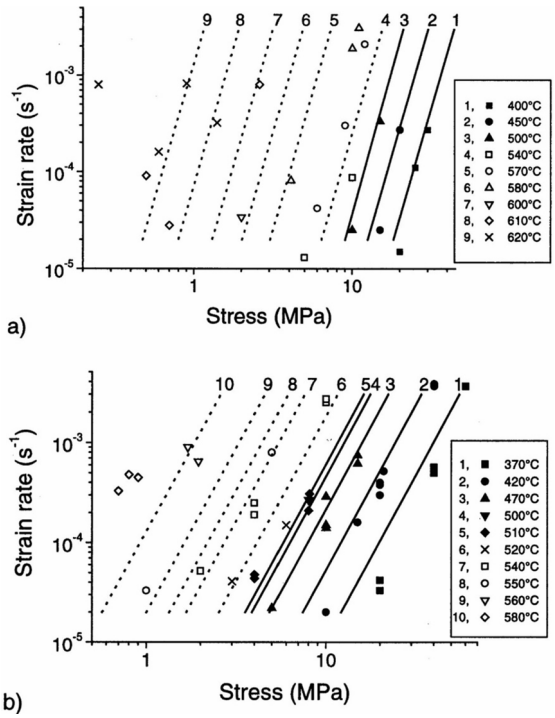

Fig. 3.23. Strain rate versus UTS under different temperature for (a) AA3104 and (b) AA5182 alloys. Hollow symbols: data above solidus; solid symbols: data below solidus. Lines represent predictions below solidus (—) and above solidus (- - -) [18]. The tests were performed upon reheating.

boundaries. The ductility, however, is more complex and influenced by the amount of final eutectic liquid and the occurrence of creep.

3.3.1.5. Effect of the initial state on the strength and ductility of semi-solid aluminium alloys. The as-cast and deformed materials exhibit different behaviours when it comes to semi-solid mechanical properties. The deformed and homogenised materials have a fine, equiaxed grain structure with few secondary phases at grain boundaries compared to the as-cast materials. The deformation process reduces the porosity, and consequently, the number of pores, which are the pre-existing nucleation sites for hot tears. These phenomena lead to a higher solidus temperature and UTS close to the solidus. The contrary tendency may occur close to the liquidus because grain bridging is easier between dendrites than between equiaxed grains. These phenomena are shown in Fig. 3.27.

In terms of the ductility, deformed alloys frequently exhibit a lower ductility in the BTR, as shown in Fig. 3.28. This tendency is attributed to two factors: the smaller amount of eutectics and fine grain structure in the deformed material decrease and increase the semi-solid ductility, respectively. The two opposite factors lead to a lower ductility in deformed materials. The lower boundary of the BTR and ZDT is shifted to a higher temperature in deformed alloys, likely because of the increased solidus temperature. Several examples are shown in Figs. 3.28 and 3.29. It should be noted that the deformed samples can be used to measure the semi-solid mechanical properties of welded joints and heat-affected zones, while they cannot be used to investigate the semi-solid mechanical

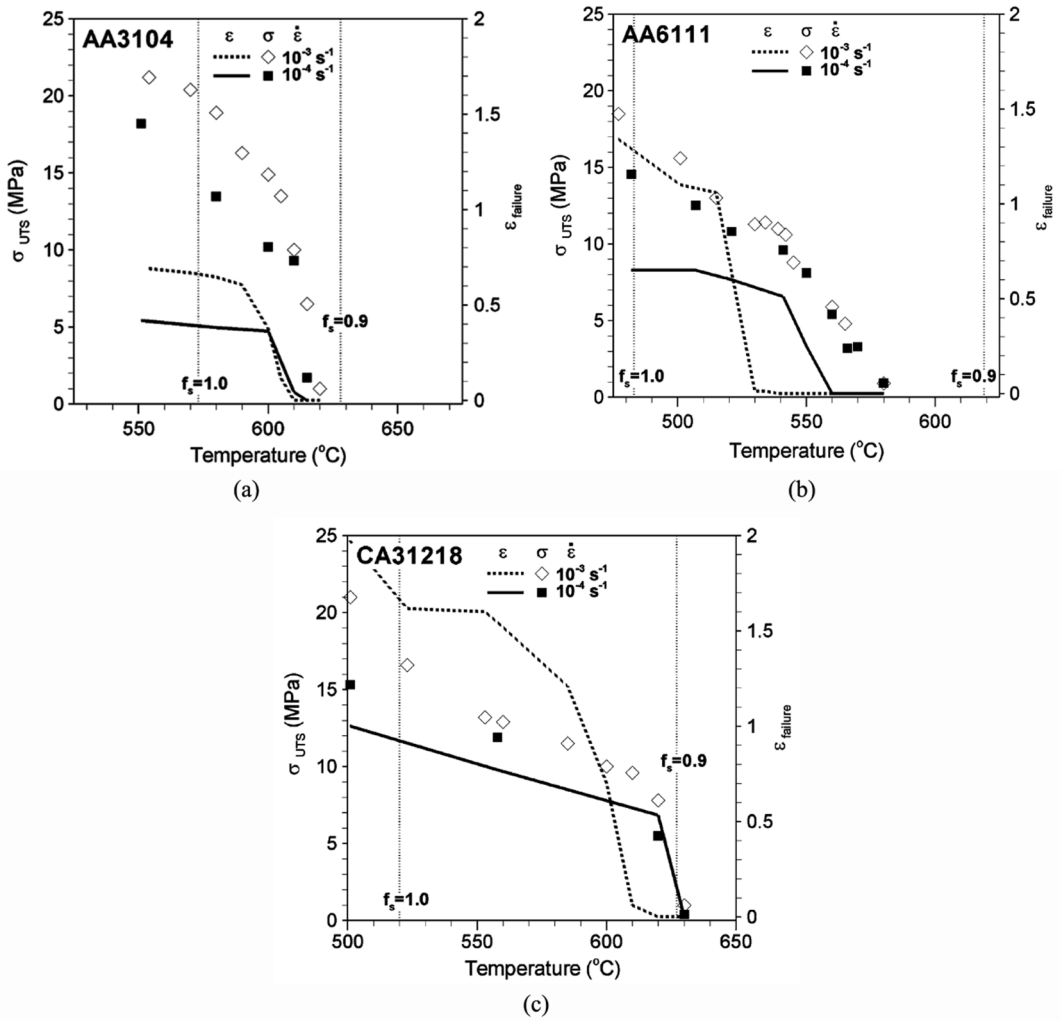

Fig. 3.24. Peak stress (σ_{UTS}) and failure strain (diametric strain) (ε) as functions of solid fraction for (a) AA3104, (b) AA6111, and (c) CA31218 (an alloy similar in composition to AA3003) alloys at different strain rates ($\dot{\varepsilon}$) [39]. The solidus and the temperature corresponding to the solid fraction of 0.9 are given. The tests were performed upon reheating.

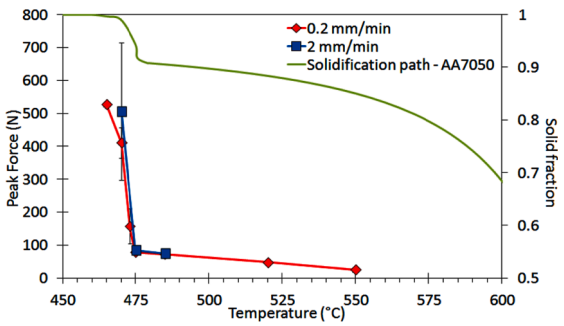

Fig. 3.25. Variation of peak forces with the temperature at two displacement rates. The corresponding solid fraction curve is given [38]. The tests were performed upon solidification.

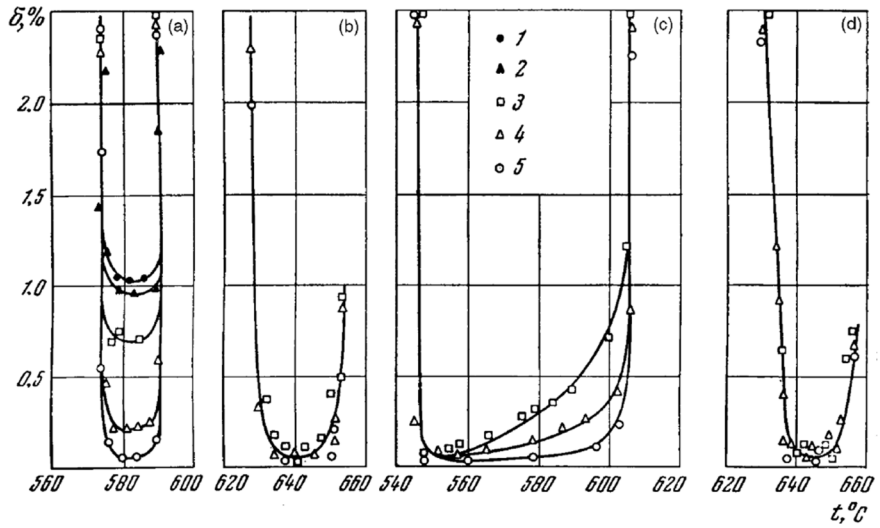

Fig. 3.26. Variance of semi-solid elongation (δ) with temperature during solidification (1, 2) and reheating (3, 4, 5) in different deformation rates (1–4: 2, 5, 8, and 80 mm/min, respectively; 5: dynamic loading) of (a) Al–5 wt% Si, (b) Al–0.6 wt% Si, (c) Al–6.5 wt% Cu, and (d) Al–1.5 wt% Cu [15]. The testing method is the same as that used in Fig. 3.18.

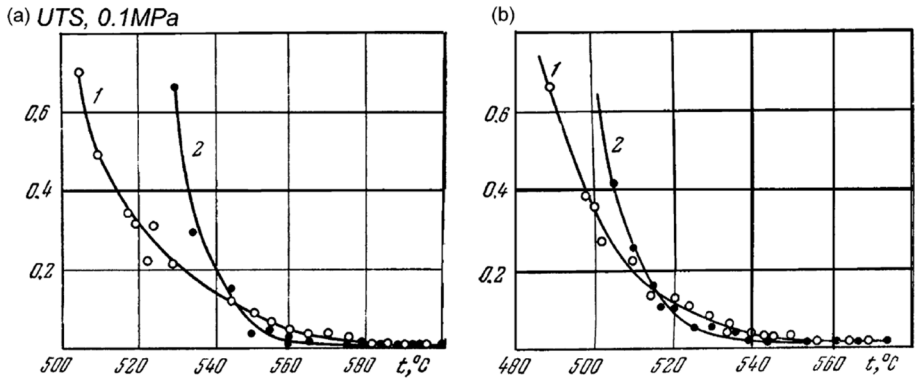

Fig. 3.27. Variance of UTS with the temperature of (1) as-cast and (2) hot-rolled and homogenized alloys: (a) Al–7 wt% Mg and (b) Al–10 wt% Mg [15]. The testing method is the same as that used in Fig. 3.18.

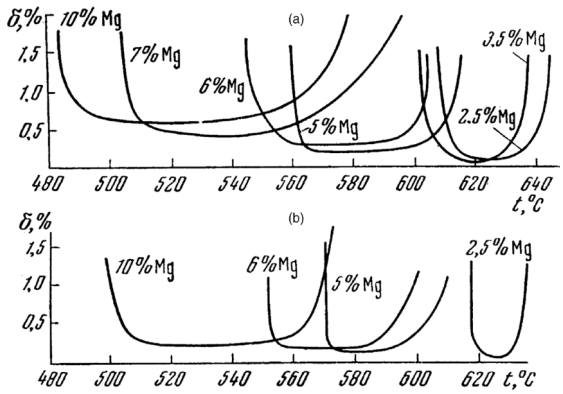

Fig. 3.28. Variance of semi-solid elongation (δ) with temperature in (a) as-cast and (b) deformed Al-Mg alloys [15]. The testing method is the same as that used in Fig. 3.18.

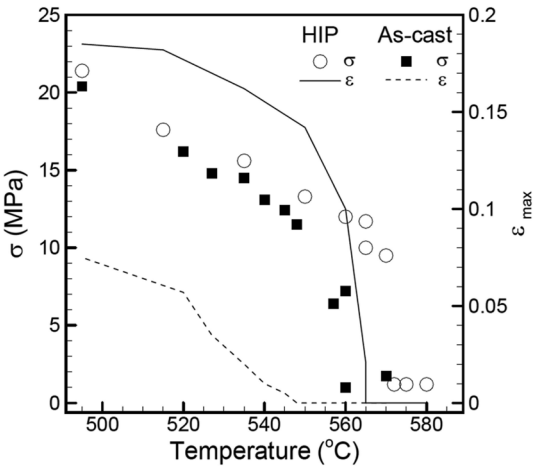

Fig. 3.29. Temperature dependence of the UTS and strain-to-failure of as-cast and HIP AA5182 alloys [40]. The tests were performed upon reheating.

properties of DC-cast materials.

3.3.2. Effect of the composition on the strength and ductility of semi-solid aluminium alloys

Eskin et al. [15] summarised the strength and ductility of some semi-solid binary, ternary, and commercial cast and wrought aluminium alloys. Since 2004, considerable attention has been focused on the mechanical properties of commercial aluminium alloys, which are summarised in the following text according to the alloy series. Moreover, the effect of impurities on the mechanical properties of semi-solid aluminium alloys is described. Note that for many commercial alloys, the effect of different factors has been mentioned previously and thus these alloys are described only briefly in the following text. The zero strength/ductility temperature/solid fraction data of different commercial aluminium alloys, extracted from the relevant references, are presented in Table 2.

3.3.2.1. 3XXX alloys. Phillion et al. [39] measured the semi-solid strength and ductility of as-cast AA3104, AA6111 and CA31218 (alloy similar in composition to AA3003) alloys upon reheating at different strain rates (Fig. 3.24). The effect of the strain rates on the strength and ductility of these alloys has been described above. Additionally, the difference in the ZST and ZDT is defined as the "vulnerable temperature range" [39,108], where the material can still withstand certain stress but with low ductility. The vulnerable temperature ranges of the three alloys match well with their hot tearing susceptibilities, as obtained from industrial practice (Table 2): AA3104, CA31218, and AA6111 exhibit the least, intermediate, and highest tendency to undergo hot tearing, with a vulnerable temperature range of less than 10 °C, less than 20 °C, and between 20 and 50 °C, respectively. This is because an alloy with a small vulnerable temperature range spends less time within the critical temperature range and is thus less prone to hot tearing. Note that van Haaften et al. [18] also studied the semi-solid strength properties of as-cast AA3104 alloy (Fig. 3.23). The stress results for AA3104 measured by Phillion et al. differ by about 50% as compared to those given by van Haaften et al. under the same solid fraction and strain rate. This is attributed to the difference in the compositions between the samples, causing different solid fractions at the same

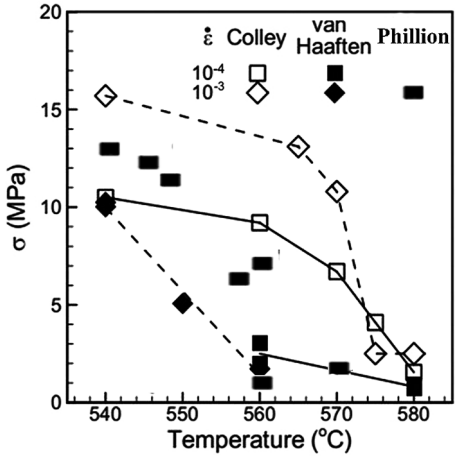

Fig. 3.30. Comparison of semi-solid UTS for AA5182 alloys measured by Colley et al. [42], van Haaften et al. [18], and Phillion et al. [40].

temperature. The solidus temperature reported by Phillion et al. [39] is 565 °C, which is 30 °C higher than the corresponding measurement of van Haaften et al. [18].

3.3.2.2. 5XXX alloys. Both Colley et al. [42] and van Haaften et al. [18] measured the semi-solid strength properties of AA5182 alloys upon reheating, as shown in Fig. 3.22(a) and Fig. 3.23(b), respectively. The effect of the strain rate on the strength properties of AA5182 alloys has been described above. The results of both experiments for strain rates of $\sim 10^{-4}$and 10^{-3} s^{-1} are replotted in Fig. 3.30. The data are qualitatively similar since the UTS decreases with the increasing temperature and the ZST occurs at around 580 °C as listed in Table 2. The UTS measured by Colley et al. [42] below the temperature of ZST is two to three times larger than that measured by van Haaften et al. [18], likely because of the different experimental conditions. The tested specimens were oriented vertically in Colley et al.'s study but oriented horizontally in van Haaften et al.'s study. This could affect the measurement results since the horizontally loaded specimens will be affected by gravity. Phillion et al. [40] measured the semi-solid strength properties of AA5182 alloys upon reheating at a strain rate of $\sim 10^{-3}$ s^{-1} by using the "2TC technique" described in Section 2.1.1, and the data are shown in Fig. 3.30. The tested specimens were oriented vertically. Their results are intermediate to those reported by Colley et al. [42] and van Haaften et al. [18]. The data from Phillion et al. are likely more accurate because their experimental method effectively addressed the three inherent challenges (Fig. 2.1) encountered in semi-solid testing. Moreover, both Colley et al. [42] and Phillion et al. [40] measured the semi-solid ductility (diametric strain) of AA5182 alloys upon reheating, as shown in Fig. 3.22(b) and Fig. 3.29, respectively. Colley et al. [42] reported the effect of the strain rates on the ductility, and Phillion et al. [40] studied the effect of the initial state, both of which have been described above. The ZDT points from these two reports are listed in Table 2. One can find that the results are different at the same strain rate of about10^{-3} s^{-1}. As mentioned above, the data from Phillion et al. [40] should be more accurate due to the more accurate testing technique.

Ludwig et al. [20] measured the semi-solid tensile properties of AA5182 alloys at a displacement rate of 0.02 mm s^{-1} upon solidification. As illustrated in Fig. 3.31(a) and Table 2, the maximum tensile stress increased sharply when the solid fraction was beyond 0.94 and the same point was observed by Ludwig et al. [21] for Al-2 wt% Cu and Al-4 wt% Cu alloys upon solidification (Fig. 3.31(b)). As listed in Table 2, the characteristic points of different aluminium alloys lie in the range between 0.9 and 0.97, which are related to the compositions and testing conditions. The point is delayed to a higher solid fraction when testing under the solidification condition with regard to reheating. As mentioned in Section 3.3.1.1, this characteristic point is closely related to the grain bridging/coalescence phenomenon. These semi-solid data have been used to obtain the relevant semi-solid constitutive parameters for a viscoplastic model (Section 5.1.1).

3.3.2.3. 6XXX alloys. Fabregue et al. [41] measured the semi-solid tensile properties of AA6056 alloy upon reheating and solidification under different strain rates. The effects of different testing methods and strain rates have been described above. Moreover, it was found that the higher Si content in AA6056 alloy leads to the higher maximum stress at the same solid fraction, as shown in Fig. 3.21 (b), because the grain bridges consisting of eutectic structure in the 2 wt% Si alloy are stronger than that in AA6056. As Si is added, the solid fraction where the eutectic structure begins to form is shifted from 0.98 to 0.9. The formation of more eutectic phases enhance the semi-solid network resulting in higher tensile strength.

Nagaumi et al. [45,107] reported the semi-solid tensile properties of two 6XXX alloys upon solidification: HS50 (1.1 wt% Mg, 1.2 wt% Si, 0.8 wt% Cu, 0.42 wt% Mn, 0.42 wt% Cr, 0.18 wt% Fe) and HS60 (1.12 wt% Mg, 1.23 wt% Si, 0.79 wt% Cu, 0.39 wt% Mn, 0.38 wt% Cr, 0.16 wt% Fe), as shown in Fig. 3.32 and Table 2. Although their compositions and liquidus temperatures are quite close, the

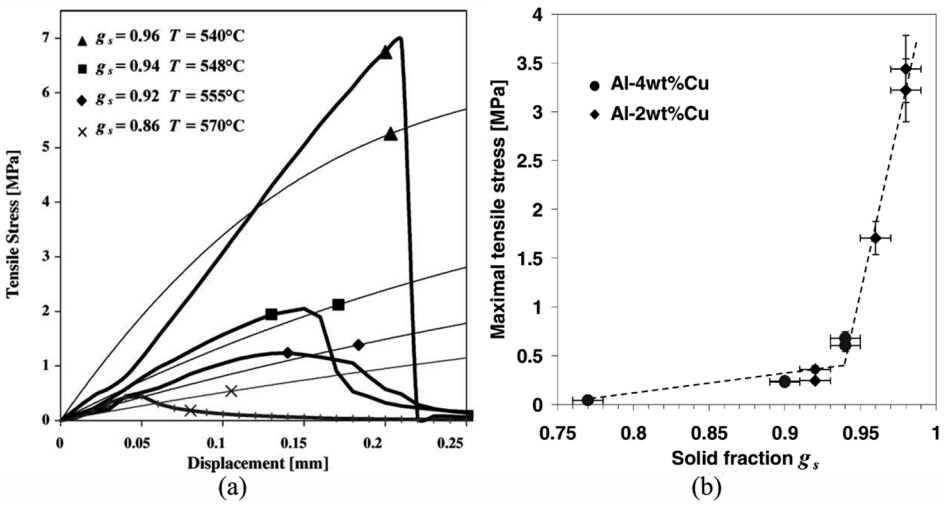

Fig. 3.31. (a) Tensile curves of AA5182 alloy at different temperatures or solid fractions (experimental (thick curves) and predicted results (thin curves)), and (b) variation of UTS with the solid fraction of two Al-Cu alloys [20,21]. The tests were performed upon solidification.

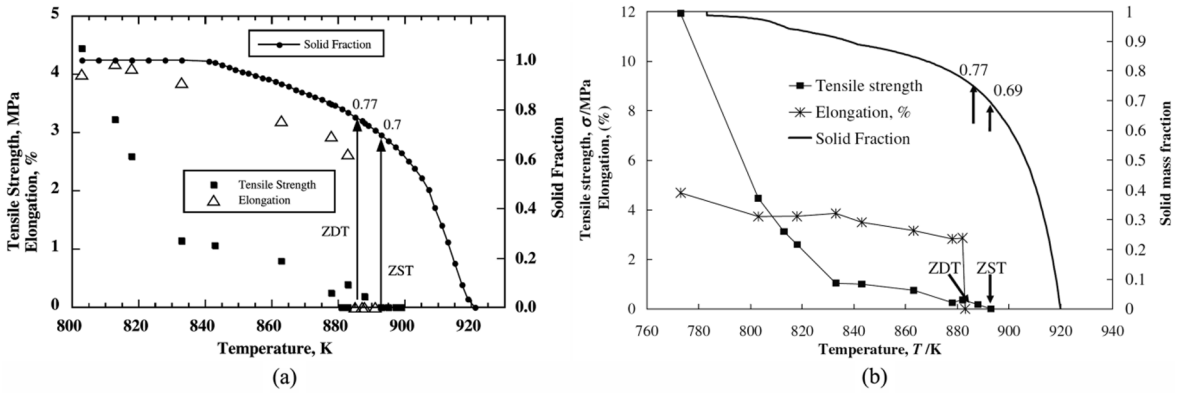

Fig. 3.32. Tensile strength and elongation versus temperature of (a) HS50 and (b) HS60 alloys. Solid fraction, ZST, and ZDT are also given [45,107]. The tests were performed upon solidification.

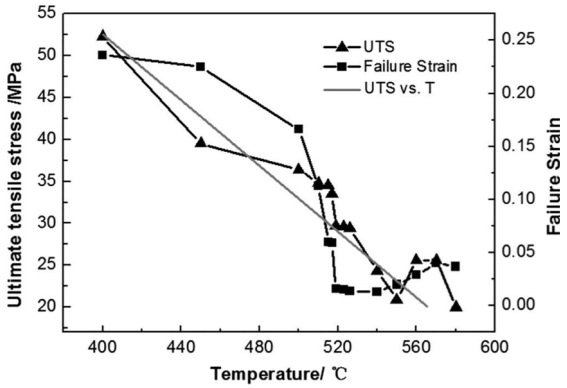

Fig. 3.33. Variations of UTS and failure strain with temperature for extruded AA7075 alloy [37]. The tests were performed upon reheating.

solidus temperatures and semi-solid tensile properties (both strength and ductility) are notably different. This could be attributed to the different DC casting parameters. By comparing the fracture morphology of the tensile sample with that of a DC billet, it is confirmed that the obtained tensile properties can be used to simulate the occurrence of hot tearing in the DC casting process.

3.3.2.4. 7XXX alloys. Chen et al. [37] reported the strength of the extruded AA7075 alloys upon reheating at a strain rate of 10^{-3} s^{-1}, as shown in Fig. 3.33. Although the tested UTS is still about 20 MPa at 550 °C due to the influence of a high-temperature adhesive, the alloy is thought to have lost the tensile strength and the ZST is approximately equal to 550 °C (Table 2).

Subroto et al. [8,38] measured the tensile behaviour of AA7050 alloy at different displacement rates upon solidification (Fig. 3.25). The effect of the displacement rates has been described above. The data were used to obtain relevant semi-solid constitutive parameters for a viscoplastic model to simulate the DC casting process (Section 5.1.1).

In summary, since 2004, more commercial aluminium alloys have been investigated to obtain reliable semi-solid strength properties. Some data have been used to build constitutive models for semi-solid aluminium alloys (see Section 5.1.1). However, as listed in Table 2, only a few studies for 2xxx and 7xxx alloys (like AA7055 and AA7085) were carried out after 2004. As cracking in 2xxx and 7xxx alloys is a notable practical problem during DC casting, adequate data are required to prevent the occurrence of cracking defects.

3.3.2.5. Impurities. Although the impurity levels are generally very low, their effect on the mushy zone mechanical properties should not be underestimated, and it is necessary to control the impurity content to avoid hot tearing in industry

Nagaumi et al. [108] investigated the effect of the Fe content on the semi-solid tensile properties of HS65 alloys (0.83 wt% Mg, 1.0 wt% Si, 0.4 wt% Cu) upon reheating. It was found that needle-shaped α(AlFeMn) intermetallic particles, which were formed early during solidification, could bridge the gap between the primary dendrites. As a result, the ZST increased from 623 °C (f_s = 0.79) to 631 °C (f_s = 0.63) with the Fe contents increasing from 0.15 to 0.25 wt%. Meanwhile, the ZDT increased from 613 °C (f_s = 0.82) to 617 °C (f_s = 0.78) with the addition of Fe. It is found that the vulnerable temperature range is wider with the increase of Fe content. And the vulnerable temperature range was found to be a good indicator of the hot tearing susceptibility, consistent with the reports of Phillion et al. [39] and Yang and Ou [15]. With the increase in the Fe content, the needle-shaped particles made grain boundaries more brittle, and hot tears occurred easily during solidification.

The effect of iron-rich intermetallics on the semi-solid tensile properties near the solidus for Al-Cu 206 cast alloys with different Si and Mn contents was evaluated by Bolouri et al. [36], as shown in Fig. 3.17(c). Alloy 311 contains 0.1 wt% Si and 0.1 wt% Mn and forms plate-like β-Fe(Al_7CuFe) intermetallics, whereas Alloy 333 contains 0.3 wt% Si and 0.3 wt% Mn and forms Chinese script-like α-Fe($Al_{15}(FeMn)_3(SiCu)_2$) intermetallics. As shown in Fig. 3.17(c), the maximum stress of the alloy dominated by the α-Fe intermetallics is generally higher than that dominated by the β-Fe intermetallics over the liquid fraction range from about 0.6% to 2.8%. This finding indicates that the structure with the Chinese script-like α-Fe intermetallics facilitates the formation of solid bridges. As can be seen from Fig. 3.17(d), the solid fraction corresponding to the ZDT in Alloy 333 is lower than that in Alloy 311, because the interdendritic liquid films flow more freely within the semi-solid structure with Chinese script-like α-Fe particles compared to that in the case of plate-like β-Fe particles.

To summarise, the presence of impurities can change the morphology, distribution, and types of secondary phases, which often occur in the late stage of solidification, thereby affecting the formation of the solid bridges. Consequently, the semi-solid tensile properties are altered together with the hot tearing susceptibility. However, these studies on the impurities were performed rarely upon solidification. The different testing methods have a significant effect on the evolutions of the secondary phases during the last stage of solidification and thus their semi-solid strength properties Future work should be focused on clarifying the influence of the impurities on hot tearing.

The following conclusions can be derived from Section 3.3: the tensile strength and ductility of semi-solid materials depend on the as-cast microstructure (solidification conditions, structure modification by addition of alloying elements, grain refiners, etc.), alloy composition (amount of eutectics), behaviour of solid bridges, and wetting conditions at the liquid/solid interface. Accurately determining the tensile properties of semi-solid aluminium alloys is essential to establish the constitutive equations for hot tearing simulations. Although the semi-solid tensile properties of many aluminium alloys have been measured, some data still need to be validated due to their low values and measurement errors. Particularly, reliable data of semi-solid AA2xxx and 7xxxx alloys need more attention in future. The use of powerful machine learning algorithms, including classification and regression aspects, can play an important role in comparing, classifying, and predicting semi-solid mechanical property data. These algorithms and their possible applications in hot tearing research are discussed in Section 6.3.

3.4. Characteristic points related to hot tearing

A schematic of the solidification behaviour is shown in Fig. 1.2. A critical transition point is known as the rigidity point [14], where a continuous solid network is formed enabling the transfer of forces. Its value is related to the linear contraction onset temperature (Section 3.1), load onset temperature (Section 3.2), and ZST (Section 3.3.1). The related data of some aluminium alloys have been presented in the corresponding sections. The rigidity point is closely related to the alloy composition, grain size, and morphology. Its value varies for different testing methods. Hence, the data measured using the same type of apparatus should be used when comparing the effect of different compositions or casting parameters. For example, Li et al. [77] regarded the load onset temperature as the rigidity point for the hot tearing predictions in Al-*x*Zn-*y*Mg-*z*Cu alloys. The RDG criterion indicated that this point does not considerably influence the predicted hot tearing susceptibility for aluminium alloys because of the relatively small pressure increase at low fraction solids [64,77,78]. However, this point becomes critical when predicting the effect of the grain refinement on the hot tearing susceptibility [66]. Because the same curve of the solid fraction versus temperature is often used as an input to the RDG criterion, the rigidity point and grain size are two key parameters to predict the hot tearing susceptibility.

As solidification proceeds, solid bridges begin to form above a certain solid fraction, i.e., grain coalescence occurs. It is related to the transition from a continuous liquid film network to a fully coalesced solid skeleton. The bridges make grains combine so closely that the formed solid skeleton can transfer higher stresses and withstand larger deformations. Note that grain coalescence occurs in the last stage of solidification. A specific solid fraction (like 0.98 or 0.99) is often used to roughly consider the effect of the grain coalescence in hot tearing criteria (Section 5.2). Bai et al. [111] modified this approach by introducing two important parameters in their revised SKK criterion, namely, the fraction of the grain boundaries covered by the liquid and solid energy. For more details, the readers may refer to the corresponding text on the hot tearing criteria, presented in Section 5.2.2.1.

Many researchers have attempted to investigate grain coalescence. By applying the quenching method, Ju et al. [112] found that Al – 1–5 wt% Cu alloys exhibited significant grain coalescence in the solid fraction range of 0.9–0.97. Through semi-solid tensile testing, Ludwig et al. [21] found a similar grain coalescence onset solid fraction of 0.94 for two Al-Cu alloys where a sharp increase in strength is observed (Fig. 3.31(b)). Similar transition points where the strength increases rapidly in various aluminium alloys can be found in Section 3.3. The obtained semi-solid tensile strength have been used in the exponential creep law constitutive equation to derive the evolution of the grain coalescence with the solid fraction for hot tearing simulations (see Section 5.1.1). By combining semi-solid tensile testing with fracture observations, Mathier et al. [113] reported on a similar grain coalescence onset solid fraction of 0.92 in an Al-1 wt% Cu alloy. Using in situ XRD in a dog-bone-shaped mould to measure the strain evolution during solidification, Drezet et al. [58] found that the coalescence onset solid fraction in Al-6.2 wt% Zn alloys increased from 97.4% % to 98.4% as the solidification was reduced from 363 s to 86 s, respectively (Section 2.2.3). For the Al-Mg-Si-Fe system with a large amount of eutectics, based on the load development during solidification and microstructure examination, Sweet et al. [29] found that the morphology, prevalence, and solidification sequence of the intermetallic and eutectic compounds considerably influenced the grain coalescence. In short, grain coalescence, which occurs in the last stage of solidification, is affected by the composition, grain size and morphology, process parameters, and secondary phase features. An accurate hot tearing prediction should include the effect of the grain coalescence on the hot tear nucleation and propagation.

4. Effect of the composition and process parameters on the hot tearing susceptibility

4.1. Effect of the composition on the hot tearing susceptibility

Eskin et al. [15] published a comprehensive review of the effect of alloying elements on the hot tearing susceptibility for many aluminium alloy systems, such as Al-Cu, Al-Mg binary systems, Al-Cu-Mg, Al-Cu-Si, Al-Fe-Si, Al-Mg-Si and Al-Cu-Li ternary systems, and AA2XXX (Al-Cu-Mg), AA6XXX (Al-Mg-Si) and AA7XXX (Al-Zn-Mg) commercial alloys systems. However, since 2004 many new data for the effect of the composition on the hot tearing susceptibility have been reported. Among many results obtained from two different post-mortem tests including shape casting and DC casting, it is necessary to clarify their differences and indicate which results are more appropriate.

4.1.1. Al-Cu system

Suyitno et al. [110] investigated the effect of the Cu contents and casting speed on the hot tearing susceptibility of non-refined Al-Cu alloys. Several Al-Cu alloys were tested upon casting 200-mm round billets in a DC caster. An experimental scheme with casting speed ramping was chosen, as shown in Fig. 4.1(a). The hot tearing susceptibility was quantified as the area affected by the cracks in the horizontal cross-section divided by the area of the billet cross-section. The result is shown in Fig. 4.1(b). At a certain casting speed, a typical "lambda" curve can be observed, and the compositional range of the maximum hot tearing susceptibility is between 0.5 and 1.5 wt% Cu. A compositional dependence on hot tearing is observed for DC casting. The higher hot tearing susceptibility at lower Cu contents can be explained by the presence of coarser grains, extent of the mushy zone, less residual liquid available for feeding

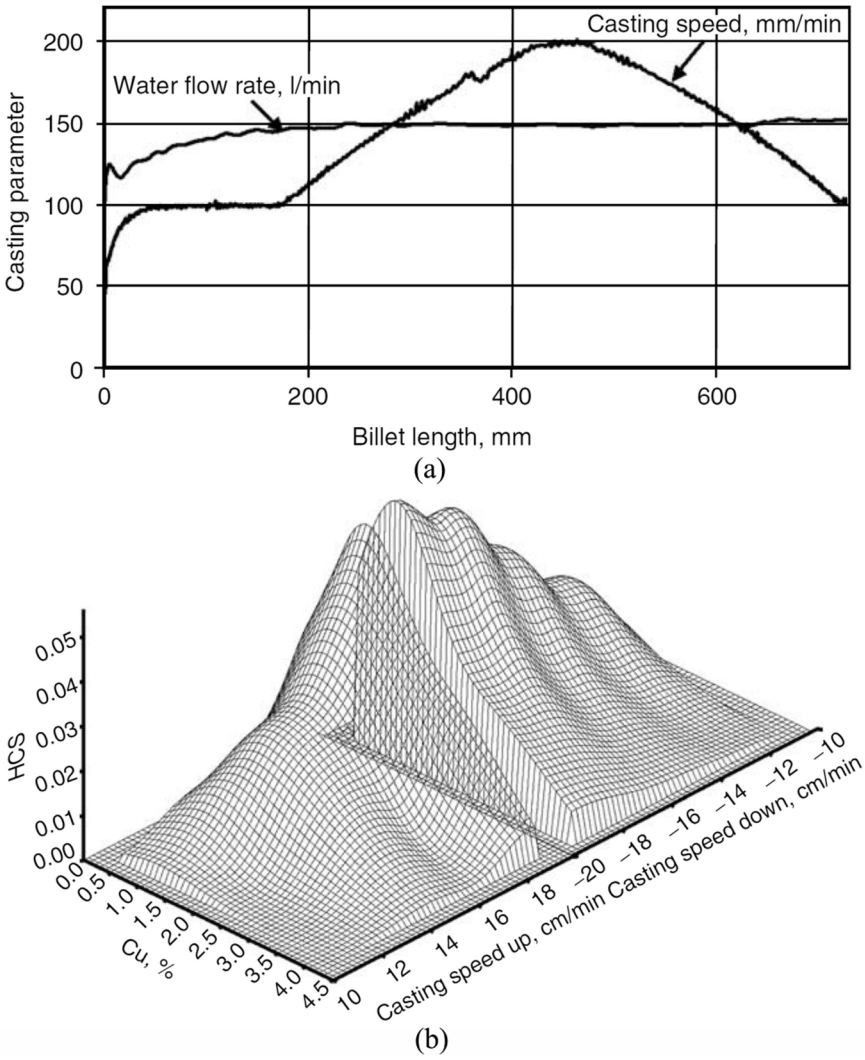

Fig. 4.1. (a) Experimental scheme of DC casting with ramping up and down the casting speed, (b) effect of Cu content and casting speed on the measured hot tearing susceptibility in Al–Cu alloys during DC casting [110].

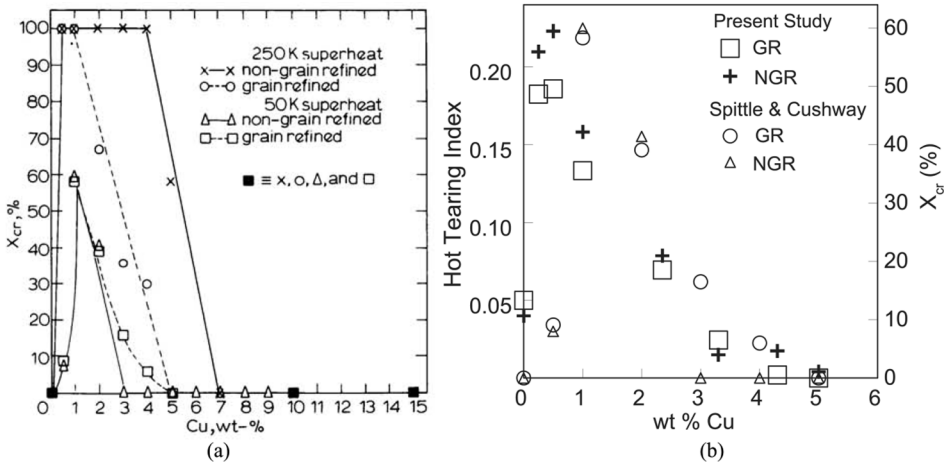

Fig. 4.2. (a) Hot tearing susceptibility (X_{cr}) from Spittle and Cushway at 50 and 250 °C superheat [114], and (b) hot tearing index from Viano et al. [68] at 100 °C superheat (the data at 50 °C superheat from Ref. [114] is replotted). 'NGR' represents non-grain refined, and 'GR' grain refined.

(represented by the amount of non-equilibrium eutectics, see Fig. 4.8), and a larger linear contraction (Fig. 3.7(a)).

As mentioned in Section 2.2.1, some devices have been designed to simulate the DC-casting conditions and employed to investigate the hot tearing susceptibility of Al-Cu alloys. Viano et al. [68] examined the hot tearing susceptibility of Al-Cu alloys by using the CHT rig (Fig. 2.7(a)) at 100 °C superheat. The hot spot zone was radiographed and the size of the hot tears was measured. The obtained result was compared with that from Spittle and Cushway [114] based on a cylindrical dog-bone-shaped mould at 50 and 250 °C superheat. These results are shown in Fig. 4.2. A typical "lambda" shape is observed in all the curves. For the 50 °C and 100 °C superheat, the most susceptible ranges are similar and observed at about 1 wt% Cu content regardless of the addition of grain refiners, although the data are from two different moulds. A higher superheat (250 °C) increases the peak of the lambda curve and makes the curve broader, because increasing superheat makes the hot tearing susceptibility at a fixed composition rise and thus expands the composition range over which hot tears are readily detectable. Moreover, grain refinement reduces the hot tearing susceptibility at a high superheat (100 and 250 °C), but has little effect at a low superheat (50 °C). The influence of the grain structure on the hot tearing susceptibility reduces with decreasing superheat, because at higher superheat the stronger intergranular liquid flow and finer grains lead to an enhanced liquid feeding, thereby preventing the formation of hot tears. In addition, Warrington and McCartney tested the hot tearing susceptibility of non-refined Al-Cu alloys by using the "cold finger" mould (Fig. 2.4) at a 60 °C superheat. It was found that the hot tearing susceptibility reached a maximum value at a copper content ranging between 0.5 and 2 wt% [56].

Table 3 summarises the compositions corresponding to the maximum hot tearing susceptibility in Al-Cu alloys from different testing moulds. The results obtained using post-mortem test moulds in shape casting (ring mould and sand mould) do not match well with the DC casting practices. By comparison, the results from the "cold finger" mould and CHT rig are quite similar to the DC casting practices. This is mainly attributed to the similarity with the DC casting conditions of the used testing moulds.

4.1.2. Al-Mg system

Clyne and Davies [31] investigated the hot tearing susceptibility of Al-Mg alloys by using a dog-bone-shaped rectangular mould (Fig. 2.6), and the hot tearing susceptibility was evaluated by using the electrical resistance method (Fig. 2.13). A typical "lambda" shape curve with the maximum hot tearing susceptibility at 1 wt% Mg was found at a 200 °C superheat, which matches well with the linear contraction measurements (Fig. 3.7(b)). Moreover, the effect of the superheat on the hot tearing susceptibility of Al-Mg alloys

Table 3
Comparison of compositions corresponding to maximum hot tearing susceptibility in Al-Cu alloys using different test moulds. 'NGR' represents non-grain refined, and 'GR' grain refined.

Alloying system	Maximum hot tearing susceptibility at this concentration (wt. %)	Condition	Device	Ref.
Al-Cu	0.5–1.5	70 °C superheat, NGR	DC casting practice	[110]
	~1.0	50 °C superheat, NGR and GR	Dog-bone-shaped cylindrical mould	[114]
	0.5–4.0	250 °C superheat, NGR		
	~1.0	250 °C superheat, GR		
	0.5–1.0	100 °C superheat, NGR and GR	CHT rig	[68]
	0.5–2.0	60 °C superheat, NGR	"Cold finger" mould	[56]
	5.0	NGR and GR	Sand mould	[31]
	0.5	20 °C superheat, NGR	Ring mould	[15]
	0.5; 3.0–3.5	100 °C superheat, NGR		

with minor impurities (0.29 wt% Fe, 0.44 wt% Si) was investigated. When the superheat is increased from 50 to 150 °C, the maximum hot tearing susceptibility increased and the Mg content corresponding to the maximum value shifted from about 1 wt% to 0.5 wt%. A similar trend was reported in Ref. [15] using the ring mould. This explanation regarding the effect of the superheat is similar to that mentioned in the above Al-Cu system [68]. Rosenberg et al. [31] investigated the hot tearing susceptibility of Al-Mg alloys but using a sand mould. It was found that hot tearing susceptibility reaches a maximum value at about 5 wt% Mg, which is significantly different from the above-mentioned results due to the difference in the testing moulds.

Thus, the Al-Cu and Al-Mg systems exhibit similar "lambda" shape composition-hot tearing susceptibility curves and the effect of the superheat is consistent. Increasing the Cu/Mg content extends the solidification range and thus increases the amount of linear contraction and the hot tearing susceptibility, while further alloying beyond the solid solution limit generates more eutectics, thereby reducing the hot tearing susceptibility. Similar to that in the case of the Al-Cu system, it is predicted that the data from Clyne and Davies [31] are more consistent with the DC casting practice since the used mould can better reproduce the DC casting conditions.

4.1.3. Al-Mg-Si system

Similar to binary alloys, ternary alloys also follow the lambda-type regularity, i.e., at certain compositions, the hot tearing susceptibility reaches its maximum value. Easton et al. [64] investigated the hot tearing behaviour of grain-refined Al-Mg-Si alloys by using the CHT rig (Fig. 2.7(a)) as a DC casting simulator. The maximum hot tearing susceptibility occurred at approximately 0.1 to 0.25 wt% Si and 0.1 to 0.2 wt% Mg (Fig. 4.3). As mentioned in Section 3.2, the maximum load value at the NES occurs in the same composition. This composition is lower than that from Jennings et al. [15] by using ring moulds (0.5 wt% Si and 0.25 wt% Mg). This is attributed to the application of grain refiners and different devices. Similar to the explanation for the lambda curve for binary alloys, the increased hot tearing susceptibility is attributed to a decrease in the amount of the final eutectic. For the Al-Mg-Si system, small amounts of the ternary eutectic Al + Mg_2Si + Si lead to a higher hot tear susceptibility.

Sweet et al. [65] investigated the dependence of the hot tearing susceptibility on the Mg content for various AA6xxx alloys using the CHT rig (Fig. 2.7(a)). As shown in Fig. 4.4, the hot tear susceptibility of all the tested 6xxx alloys decrease with the addition of Mg. When the Mg content exceeds a certain value, the hot tears are eliminated. This is because the higher-solute alloys produce more eutectics and hence exhibit a lower hot tearing susceptibility due to the excellent liquid feeding ability. The beneficial effect of high Mg contents on decreasing the hot tearing susceptibility was also observed in other systems, including 3XXX and 7XXX alloys [65].

Furthermore, Sweet et al. [29] studied the effect of the Fe content on the hot tearing susceptibility of AA6060 alloys using the same mould. The results are shown in Fig. 4.5(a). At low Fe contents (0.04–0.17 wt%), the alloy exhibits a high hot tearing susceptibility. No hot tearing occurrence is observed above 0.2 wt% Fe. At Fe contents between 0.2 and 0.3 wt%, the amount of the β-Al_5FeSi phase increases, leading to earlier grain bridging and coalescence and thus a lower hot tearing susceptibility. For Fe contents above 0.3 wt%, the hot tear susceptibility is still low mainly due to the significant increase in the eutectic feeding originating from earlier precipitation of other Fe-based phases.

In addition to the Fe content, Sweet et al. [54] reported the effect of Cu and Mn on the hot tearing susceptibility of AA6060 alloys using the same device. The hot tearing susceptibility is insensitive to the Cu content between 0 and 0.22 wt%, but increases with the Mn content above about 0.04 wt% (Fig. 4.5(b)). The data from DC casting practices confirmed this tendency [54]. The presence of Mn changes the volume fraction of α-AlFeSi and β-AlFeSi in the as-cast microstructure and thus affects the grain bridging and intergranular liquid flow.

The above-mentioned investigations can be applied during DC casting. In a vertical DC casting where a start-up off-cut length is permissible, it is feasible to add an excess of Fe or Mg to AA6XXX alloys in the start-up stage to prevent the occurrence of hot tearing. Hot tears often start at the start of casting and rarely at the steady state [65]. This addition can be achieved e.g. by adding extra Mg or Fe in the launder in the start-up stage. As Mg is easier to dissolve in aluminium alloys than Fe, it is preferred to add Mg to prevent the

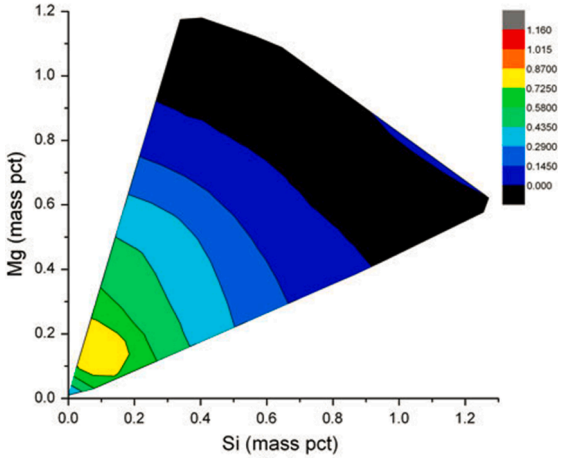

Fig. 4.3. Hot tearing susceptibility of refined Al-Mg-Si alloys [64].

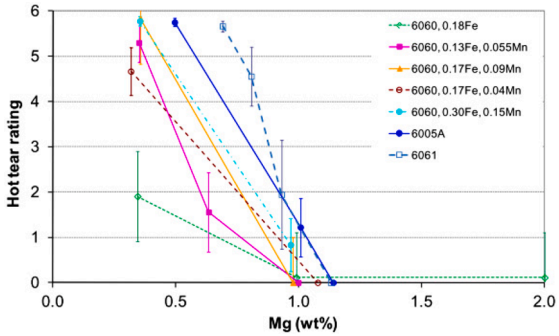

Fig. 4.4. Variance of hot tearing susceptibility with Mg content in various AA6xxx alloys [65].

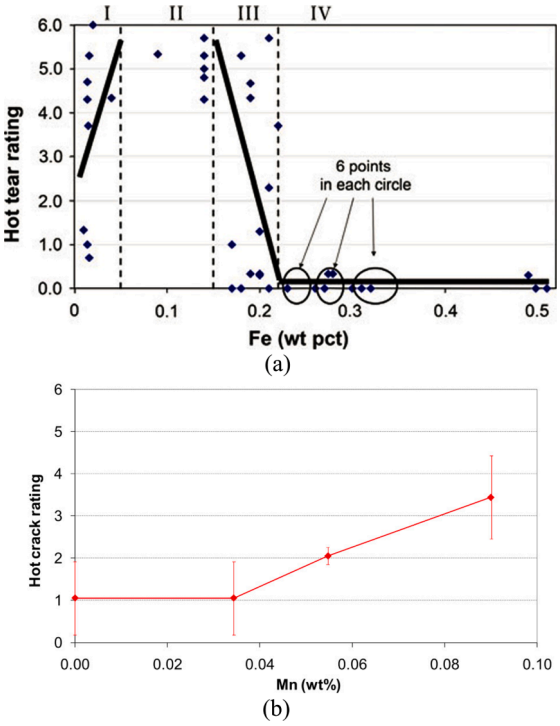

Fig. 4.5. (a) Effect of Fe content on the hot tearing susceptibility of AA6060 (0.34 wt% Mg, 0.52 wt% Si, 0.05 wt% Ti); (b) effect of Mn content on the hot tearing susceptibility of another AA6060 alloy (0.35 wt% Mg, 0.53 wt% Si, and 0.18 wt% Fe) [29,54].

hot tearing at the transient stage for commercial applications.

In terms of the AM, Li et al. [115] investigated the hot tearing susceptibility of Al-*x*Mg(-Si)-0.2 Sc-0.1Zr ($x = 1.5$, 3.0, and 6.0 wt%) alloys. In the absence of Si, the hot tearing susceptibility increases with increasing Mg content. Adding 1.3 wt% Si effectively inhibits hot tearing, which is attributed to the refined microstructure and formation of Al-Mg_2Si interdendritic eutectics. In the future, the effect of the Fe content can be investigated for the additive manufacturing Al-Mg-Si systems.

4.1.4. Al-Mg-Zn-Cu system

In the Al-Zn-Mg-Cu quaternary system, the hot tearing susceptibility exhibits a more complex behaviour and does not follow the typical "lambda" curve. Li et al. [77,78] systematically investigated the hot tearing behaviour of non-refined and refined Al-Zn-Mg-Cu model alloys by using the T-shape device (Fig. 2.8(b)). These compositions fall within the common commercial 7xxx alloy range. The results are shown in Fig. 3.14. For non-refined Al-xZn-2 Mg-2Cu ($x = 2$–12) alloys, the minimum and maximum hot tearing susceptibility values occurred at a Zn content of 4 and 12 wt%, respectively. For refined Al-xZn-2 Mg-2Cu alloys, the minimum value occurred at 4 wt% Zn, although the maximum value is shifted to 9 wt% Zn. The Zn content shift corresponding to the maximum hot tearing susceptibility is attributed to the tensile stress development and liquid feeding ability. First, the grain-refined Al-12Zn-2 Mg-2Cu alloy is subjected to lower tensile stresses than the grain-refined Al-9Zn-2 Mg-2Cu alloy, in contrast to the case in the non-grain-refined

condition. Moreover, the Al-12Zn-2 Mg-2Cu alloy has more non-equilibrium eutectics than the Al-9Zn-2 Mg-2Cu alloy, suggesting its enhanced liquid feeding ability. The addition of Mg and Cu decreases and increases the hot tearing susceptibility of refined Al-9Zn-2 Mg-2Cu alloys, respectively. The complex tendencies of these main elements are attributed to the interaction of the tensile stresses (Fig. 3.14), melt feeding, and final eutectics. The SKK criterion introduced in Section 5.2.2.1 considers these factors and thus makes good predictions on the hot tearing tendencies. Furthermore, the effects of the main alloying elements on the hot tearing susceptibility of refined Al-Zn-Mg-Cu model alloys (Fig. 3.14) were successfully applied to rate four commercial 7xxx alloys: the hot tearing susceptibility rises from AA7022, AA7050, AA7085, to AA7055, which matches well with the DC casting practice and linear contraction

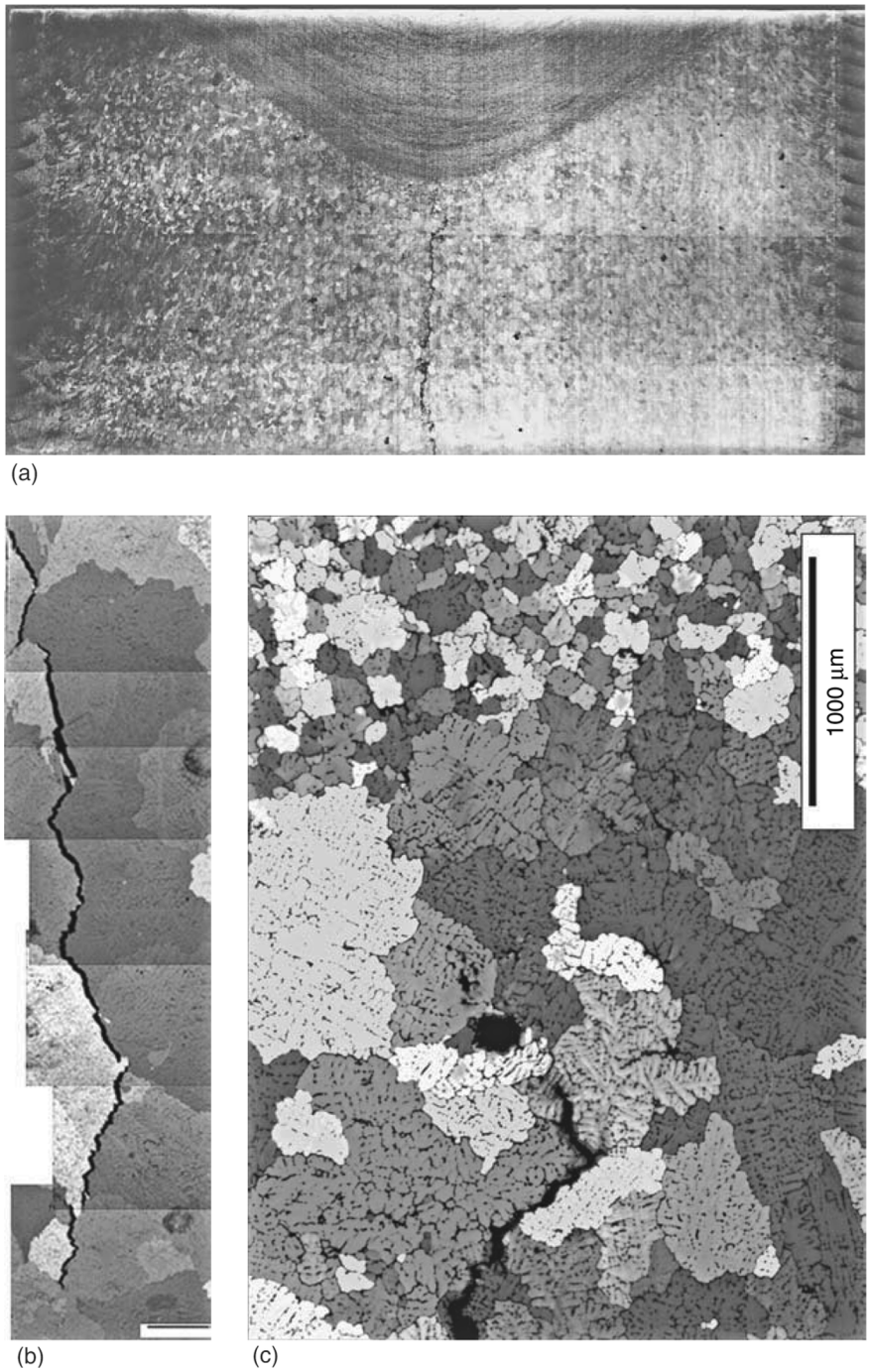

Fig. 4.6. Propagation and stop of a hot tear in a DC-casting AA7075 billet: (a) macro photo showing the transition zone from non-refined to refined structure; (b) propagation of the hot tear along grain boundaries in the non-refined zone; (c) stop of the hot tear in the refined zone [117].

data upon solidification (Fig. 3.6). This is explained as follows: first, AA7022 has the lowest Cu content and the highest Mg content, and its Zn content is closer to 4–6 wt%, all of which lead to its lowest hot tearing susceptibility according to the influence rules of the main alloying elements. AA7055 and AA7050 exhibit similar compositions except for the Zn content. AA7055 has a higher hot tearing susceptibility than AA7050 because its Zn content is close to 9 wt% and other compositions are similar. Moderate Zn content as well as lower Mg and Cu content makes the hot tearing susceptibility of AA7085 lie between AA7055 and AA7050. Thus, the effects of the alloying elements can be used as a guideline to evaluate the hot tearing susceptibility when developing new 7xxx aluminium alloys.

Ellingsen et al. [55] reported on the effect of the Fe and Si contents on the hot tearing susceptibility in AA7075, based on the DC casting practice. No obvious relationship was observed between the Fe content and critical casting speed (representing the hot tearing susceptibility) because Fe-based phases form early and have no influence on the last stage of solidification. In contrast, the alloy with a higher Si content exhibits a higher hot tearing susceptibility due to the formation of low-melting S(Al_2CuMg) and Al_7Cu_2Fe phases. Recently, we investigated the effect of Fe and Si contents in the Al-9Zn-2 Mg-2Cu model alloys by using the T-shape device (Fig. 2.8(b)) [104]. The same regularity with respect to Fe was obtained because the Fe-based intermetallics are generated in the early stage of solidification in which hot tearing likely does not occur, but interestingly the addition of Si decreases the hot tearing susceptibility of the Al-9Zn-2 Mg-2Cu-xSi alloys. Unlike in the case of Ref. [55], no Fe addition is performed when studying the effect of Si and the low-melting S(Al_2CuMg) and Al_7Cu_2Fe phases are not formed. The decrease in the hot tearing susceptibility in the higher Si content occurs because the Si addition promotes the formation of grain coalescence and leads to earlier grain bridging, as discussed in Section 3.2. In the future, the effect of the co-additions of Fe and Si on the hot tearing susceptibility of 7XXX alloys should be further investigated, and the relevant semi-solid tensile tests should be performed to clarify the evolutions of the grain coalescence with the solid fractions under different Fe and Si levels. These investigations can help to define the addition level of Fe and Si required to prevent the occurrence of hot tearing in DC casting, such as in the AA6XXX alloys.

The effect of Si on the hot tearing behaviour of AA7XXX alloys subjected to AM has also been investigated. Montero et al. [116] reported that the addition of Si decreased the hot tearing susceptibility of AA7075 mainly because grain refinement occurred as the Si content increased. But Stopyra et al. [12] observed the opposite phenomenon in AA7075 because grain refinement did not occur in their study, and the Si segregated to the grain boundary, which increased the stability of the liquid film. Compared with that in the above-mentioned as-cast sample, the grain refinement effect of Si in AM is the main reason for the reduction in the hot tearing susceptibility. However, the detailed grain refinement mechanism is still unclear and must be further examined.

In summary, the results obtained from the devices simulating DC casting conditions are closer to casting practice and often different from those obtained using post-mortem test moulds in shape casting. For the main alloying elements, the compositional dependence of hot tearing exists in DC casting and a typical “lambda” curve still occurs in binary and ternary systems but is absent in quaternary systems. For minor elements, the hot tearing susceptibility is affected by the change in the type, morphology, amount, and distribution of the secondary phases. The presence of secondary phases affects the load development during solidification, semi-solid strength and ductility, hot tearing characteristic points, and permeability of the mushy zone. For commercial aluminium alloys, the compositional range of the main elements is often fixed to a narrow band, but adjusting the contents of the minor elements is a practicable way to reduce the hot tearing susceptibility as described previously [54,55]. The researchers should attempt to clarify the effect of the addition of minor elements on the hot tearing susceptibility of commercial aluminium alloys in DC casting by combining the advanced hot tearing tests, in situ observations, semi-solid tensile tests, and hot tearing simulations.

4.1.5. Grain refiners

A common approach to improve the microstructure and properties of as-cast material is grain refinement. Nadella et al. [117] investigated the effect of grain refinement on the hot tearing susceptibility in DC-casting AA7075 billets. Two methods of adding grain refiners were investigated. First, the billet was cast without adding grain refiners, and Al–3Ti–1B rods were added into the melt in the launder (Fig. 1.1(a)). As shown in Fig. 4.6, a hot tear occurred in the start-up phase of the casting at a speed of 80 mm/min and propagated along the grain boundaries. The hot tearing process stopped when grain refiners were added. A hot tear reoccurred when the casting speed increased to 120 mm/min. The second test was conducted with a similar processing sequence, albeit with a refined melt grain prepared in the furnace. No hot tears occurred in the entire billet. In the two cases, the grain size was reduced significantly from 1080 to 165 μm with the addition of the grain refiners; this aspect depended slightly on the casting speed (165 and 95 μm at 80 and 120 mm/min, respectively) but not on the approach through which the grain refiners were added. No notable difference was observed in the dendrite arm spacing (approximately 23 μm) in the centre of the non-grain-refined and grain-refined billets. Thus, the grain refinement can efficiently decrease the hot tearing susceptibility of DC-cast aluminium alloys, because the grain refinement often results in a smaller linear contraction and slower load development owing to the delay in reaching the rigidity point (Figs. 3.6 and 3.13), higher semi-solid tensile strength and ductility (Section 3.3), and lower permeability of the mushy zone. The complex interaction of these phenomena often results in a decrease in the hot tearing susceptibility. The fact that the hot tear re-occurs at a higher casting speed in the first test and does not occur at all in the second test can be explained by the absence of the micro-cracks as the initiator of hot tears in the second test.

The positive effect of grain refinement on preventing the development of hot tears was also observed in post-mortem tests during DC casting. In the “cold finger” mould (Fig. 2.4), Warrington and McCartney [57] found that grain refinement reduced the severity of hot tearing in AA7010 and AA7050 with a moderate addition of grain refiners. The minimum hot tearing susceptibility occurred at 0.005 wt% and 0.03 wt% Ti, respectively. Easton et al. [66] used the CHT rig (Fig. 2.7(a)) and found that grain refinement delayed the load onset point and load development during solidification (Fig. 3.15) and reduces the hot tearing susceptibility in AA6061. The above-mentioned reasons in terms of DC casting can explain these positive effects of grain refinement in these post-mortem tests during DC casting.

Grain refinement through the addition of Sc, Zr or Ti to form $L1_2$-type Al_3M intermetallics is also widely applied to AM to eliminate the hot tears, and the solidification microstructure often changes from columnar to equiaxed grains [118–122]. Martin et al. [118] controlled the AM solidification microstructure by adding hydrogen stabilised Zr nucleants to AA7075 and AA6061 and successfully avoided the occurrence of hot tearing. The formed Al_3Zr phase provided a high density of nucleation sites for the generation of fine-grained microstructure. Similarly, Spierings et al. [120] and Zhou et al. [119] added Sc and/or Zr to Al-Mg and Al-Mg-Zn alloys to eliminate the occurrence of hot tears through the formation of Al_3(Sc, Zr) particles, which contributed to grain refinement. Tan et al. [123] added 0.7 wt% Ti to AA2024 in situ to form Al_3Ti nanoparticles for grain refinement. Similar additions using different filler materials have also been implemented in the welding process to avoid hot tearing, as summarised in Ref. [124].

However, some experimental data have indicated that alloys with extremely fine grains or globular structures may exhibit a higher hot tearing susceptibility, as observed in Al-6 wt% Cu [56], AA7010 and AA7050 [57] alloys. When the microstructure changes from columnar or equiaxed dendritic grains to globular grains, the structure parameter that determines the permeability shifts from the SDAS to grain size and results in the decrease in the permeability of the mushy zone. The negative effect due to the decreased permeability exceeds the above-mentioned positive effects from grain refinement and thus the hot tearing susceptibility increases in the case of a globular grain structure. This has been confirmed by the predictions from the RDG model [66,125]. Nevertheless, globular structures are not always harmful. One of the technical ways to obtain globular structures is ultrasonic melt treatment. The casting practices using this technique did not show an increasing hot tearing susceptibility in globular structures for the studied 2XXX and 7XXX alloys [7]. And Li et al. [59] found that the hot tearing susceptibility still decreases in Al-Cu alloys when the grain morphology shifts from dendrite to globular grains. Whether the hot tearing susceptibility will increase with the occurrence of a granular structure is still an open topic, and the inherent mechanisms need to be investigated. Several factors including the tensile stresses, semi-solid mechanical properties, and permeability of the mushy zone should be considered comprehensively. Excess additions of grain refiners do not necessarily produce granular grains. The aggregation of the inoculant particles due to the excess additions of grain refiners will deteriorate the hot tearing resistance, as observed in AA7050 with excess amounts of Al-5Ti-1B refiners [26]. These particles block the feeding channel and act as stress accumulators, causing the formation of voids.

Other special phenomena were also found in terms of the effect of grain refinement. From Clyne and Davies' study [26], it was found that for the Al-2 wt% Mg alloy with a low hot tearing susceptibility, an increased cracking tendency occurs over a narrow range of Ti contents although the grain structure is fine and equiaxed. For the Al-1 wt% Mg with a high hot tearing susceptibility, the hot tearing susceptibility is unaffected by the Ti additions except at high levels (>0.2 wt% Ti) even though the grain morphology transforms from columnar to equiaxed grain. The reason is still unclear and further investigations are required.

In summary, grain refinement often decreases the hot tearing susceptibility. When excess amounts of grain refiners are added, the aggregation of the secondary phase particles and the presence of globular grains deteriorates the hot tearing resistance. Especially for grain sizes below 50 μm, the alloy likely exhibits a high hot tearing susceptibility due to the lower permeability. However, the aggregation of inoculant particles may be a reason for the increased hot tearing susceptibility in the alloy with a globular structure, which needs to be further investigated. In addition to Al-Ti-B grain refiners, many other types of grain refiners exist, like Al-Ti-C, Al-Ti-B-C, and Al-Sc-Zr master alloys. It is desirable to examine the effect of different grain refiners on the hot tearing susceptibility. More information regarding grain refiners and their refining mechanism can be found in Refs. [7,126–128].

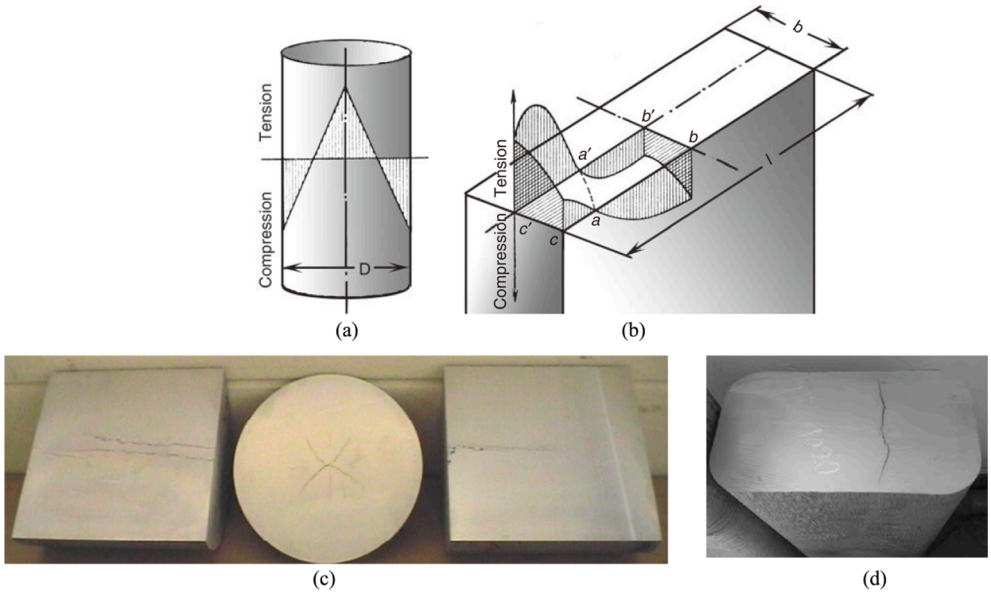

Fig. 4.7. Schematic of stress distribution in (a) a round billet and (b) sheet ingot in the steady-state stage of DC casting [7]; typical hot tears in (c) a round billet and (d) a flat ingot from DC casting [189].

4.2. Effect of the process parameters on the hot tearing susceptibility

For a commercial aluminium alloy, its composition range is often limited to be adjusted to decrease the hot tearing susceptibility. The more commonly used method to avoid hot tearing is to set appropriate DC casting process parameters. The effect of relevant process parameters on the hot tearing susceptibility during DC casting is discussed in the following subsections.

4.2.1. Dimension and geometry of ingots

DC-cast ingots can be divided into round billets and rectangular sheet ingots. These two basic shapes have different stress distributions resulting in different hot tearing susceptibilities. The thermo-mechanical behaviour of round billets is much simpler than that of the sheet ingots.

For round billets, hot tearing usually appears in the central section because of the high stresses and lack of available feeding liquid at the end of solidification. First, the stress distribution of a round billet is demonstrated in Fig. 4.7(a). A region of compressive stresses occurs in the periphery of the billet, while the centre of the billet experiences tensile stresses. The centre part has a slower cooling rate than the surface and wants to contract but is constrained by the solid shell. Consequently, tensile stresses occur at the centre, while the surface is under compression, which is confirmed by measuring the residual stresses and strains in a DC-cast AA6063 billet by using the neutron diffraction technique [96]. The amount of eutectic structure is an important structural indicator of hot tearing. It decreases towards the centre of the billet (Fig. 4.8). The stress and small amount of eutectic phases often result in a hot tear at the centre of the round billets (Fig. 4.7(c)).

For sheet ingots, the tensile stresses are located close to the short-side surface (along with the $a^{'}-c^{'}$ direction in Fig. 4.7(b)) and corners. Note that tensile stresses in the centre of the ingot may still exist, but their values are much smaller than those at the short-side periphery (area $a^{'}-c^{'}-c-a$ in Fig. 4.7(b)). Because of this stress distribution, the short side of the ingot is prone to hot tearing. The hot tear often occurs in the short-side periphery (area $a^{'}-c^{'}-c-a$ in Fig. 4.7(b)). A typical hot tear occurring in the sheet ingot is shown in Fig. 4.7(d). Moreover, it was observed that the amount, distribution, and types of non-equilibrium eutectics change along with both the thickness and length directions in a DC-cast sheet ingot [129]. Note that the width-to-thickness ratio often has a big effect on the hot tearing susceptibility in sheet ingots. Livanov [8] early reported the correlations among the ingot thickness, casting speed, and occurrence of hot tears or cold cracks based on various experimental data. When the casting speed is too fast or slow, hot tears or cold cracks will occur (Fig. 4.9(a)). There exists an appropriate casting speed zone for the corresponding ingot thickness (b_1 in Fig. 4.9(a)), although ingots thicker than a certain value appear not to be feasible (b_2 in Fig. 4.9(a)). Fig. 4.9(b) shows similar curves for various width-to-thickness ratios. When the ratio increases, the desired no-crack zone shifts to higher casting speeds and lower thicknesses of the ingots. The changes in the stress/strain fields and distribution of the eutectic structure under different width-to-thickness ratios should be investigated in detail to explain this phenomenon.

4.2.2. Casting speed

The casting speed, as one of the most important casting parameters, must be accurately controlled during the DC casting of

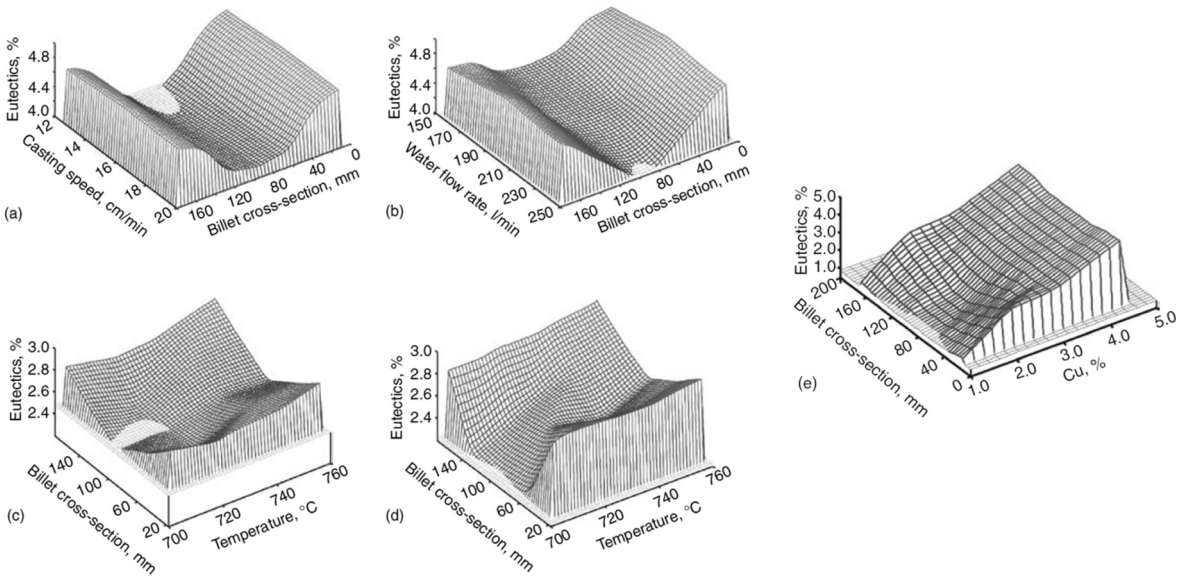

Fig. 4.8. Effect of compositions and process parameters on the amount and distribution of measured non-equilibrium eutectics in the Al–Cu system: (a) Al–4.3 wt% Cu, water flow rate 150 l/min, melt temperature 715 °C; (b) Al–4.3 wt% Cu, casting speed 200 mm/min, melt temperature 715 °C; (c) Al–2.8 wt% Cu, water flow rate 150 l/min, casting speed 100 mm/min; (d) Al–2.8 wt% Cu, water flow rate 150 l/min, casting speed 200 mm/min; (e) water flow rate 150 l/min, casting speed 200 mm/min [7,110,133].

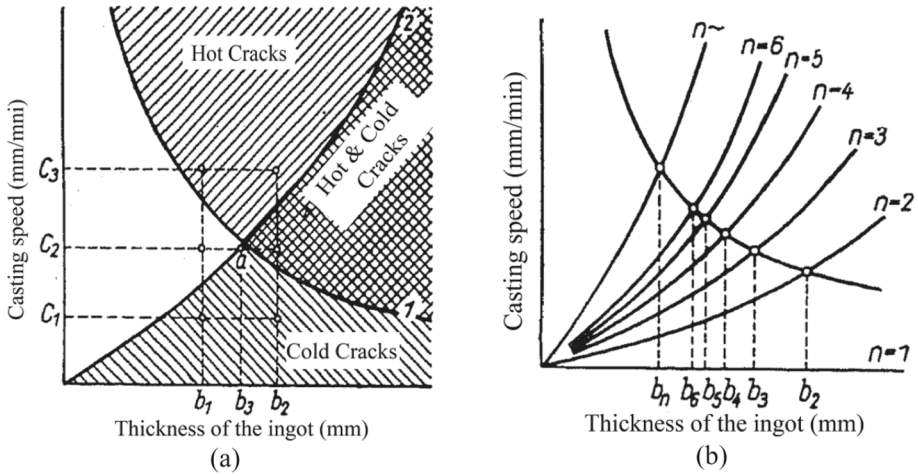

Fig. 4.9. Correlation between the thickness of an ingot, casting speed and occurrence of hot tears or cold cracks: (a) constant and (b) variant width-to-thickness ratios (n) [8].

aluminium alloys. Its effect on the hot tearing susceptibility of Al-Cu alloys has been studied systematically by Suyitno et al. [110], as shown in Fig. 4.1(b). Obviously, increasing the casting speed facilitates the occurrence of hot tearing in the centre of the billet [69,130,131] where the high stresses and strains occur with high casting speeds. The calculated dependence of the stresses and strains on the casting speeds is given in Section 5.1.2.2. The amount of eutectics tends to decrease from the surface to the centre of the billet

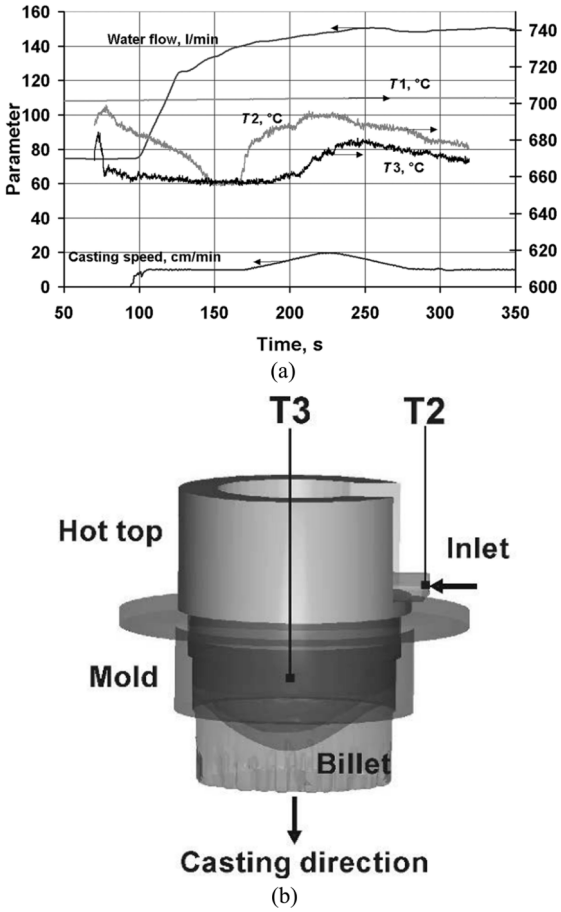

Fig. 4.10. Casting setup and the positions of thermocouples [133].

with the increase of casting speed (Fig. 4.8). Note that almost no hot tears are present at any given casting speed when the Cu content is above 4 wt% (Fig. 4.1(b)). This is attributed to the sufficient amount of eutectics under a high Cu content (Fig. 4.8(e)), suggesting sufficient liquid feeding.

An interesting fact was observed from Fig. 4.1(b) that the maximum hot tearing susceptibility corresponds not to the maximum casting speed but to a certain speed during the deceleration stage of casting. A similar phenomenon was observed elsewhere [131]. This is because the deepening of the sump (from the bottom of the hot top to the solidus, see Fig. 4.6(a)) with increasing casting speed occurs with a certain delay due to the thermal inertia. Thus, the maximum hot tearing susceptibility in fact corresponds to the deepest sump for DC casting, rather than the highest casting speed. Fig. 4.1(b) also indicates that the casting speed required for the initiation of a hot tear is higher than the casting speed at which a hot tear is healed. Similarly, this is due to the delayed development of the depth of sump originated from thermal inertia. This matches well with the experimental results as reported in Refs. [131,132].

4.2.3. Melt temperature

Unlike the casting speed, there are not too many investigations on the effect of the melt temperature on hot tearing in DC-cast billets. Only limited data on this subject are available, which is attributed to the technological difficulties of the high pouring temperatures during DC casting. The effects of the melt temperature on the microstructure evolution and hot tearing tendency have been studied in shape castings [7,15,103]. Some common phenomena occur with increasing superheat in these reports: the formations of coarser grains and even columnar structures, and the accompanying higher hot tearing susceptibility. Direct investigations of the effect of the superheat on the hot tearing susceptibility in DC casting are limited.

Such effort was made by Eskin et al. [133] by studying this effect in DC-cast Al–2.8 wt% Cu alloys. According to Fig. 4.1(b), this composition has a moderate hot tearing susceptibility. Fig. 4.10 shows the casting setup and the positions of the three thermocouples. The melt temperature in the furnace, T1, was 700, 720, 740, and 760 °C corresponding to the superheat of 47, 67, 87, and 107 °C, respectively. The temperature drop over the melt delivery system was detected by using a thermocouple situated in the entrance to the hot top, T2. The third thermocouple was installed in the centre of the bottom edge of the hot top, T3.

Table 4 gives the widths of the transition zone and mushy zone, and the sump depths under different melt temperatures. The only obvious difference is that the width of the transition zone in the centre of the billet decreases with the increase in the melt temperature. This is attributed to a faster downward movement of the liquidus isotherm compared to that of the solidus isotherm. The slight variations in the sump depth suggest that there should not too many differences in terms of hot tearing susceptibility. However, the DC casting practice exhibits a smaller hot tearing susceptibility at a higher melt temperature. This is contrary to those obtained using shape mould devices [7,15,103]. Several reasons are given based on liquid feeding ability and tensile stress/strain developments. First, with the increase in the melt temperature, the mushy zone keeps its dimension, but the transition zone becomes slightly thinner in the centre of the billet (Table 4), suggesting that the alloy spends less time during solidification. The fully liquid area (difference in the sump and mushy zone) becomes slightly deeper with the increase in the melt temperature, leading to a larger metallostatic pressure in the mushy zone, and a higher liquid feeding ability to potential pores and micro-cracks. This is verified by the observation that several micro-cracks have been healed by the eutectics spreading along grain boundaries. It has been pointed out in Sections 4.2.1 and 4.2.2 that the amount of eutectic structure is an important structure indicator for the hot tearing susceptibility, i.e., the larger the amount of eutectics, the lower the hot tearing susceptibility. Fig. 4.8 shows that the amount of eutectics increases with the increase in the melt temperature, which matches well with the reduced hot tearing susceptibility. With the increase in the melt temperatures, a coarser dendritic structure is formed resulting in wider liquid flow channels and a stronger melt flow due to the macro-segregation further facilitates the liquid feeding in the centre of the billet. Therefore, more eutectics are generated.

In addition to the feeding behaviour, the tensile stresses and strains in the centre of the billet are crucial. As shown in Fig. 3.3(a), the expansion occurs before the thermal contraction, which can compensate for the contraction [73] and reduce the hot tearing susceptibility. Note that even a small increase in the hydrogen solubility at a higher melt temperature will result in more gas evolution at the early stage of solidification and the induced pre-shrinkage expansion can reduce the hot tearing susceptibility of the billet [73]. In short, the effect of the melt temperature on the hot tearing susceptibility in DC casting is different from that in shape casting due to the effect of the higher liquid feeding capacity and more gas evolution at a high DC-casting temperature.

4.2.4. Water flow rate

The water flow rate in DC casting contributes to the heat transfer coefficient at the surface, h. The equivalent heat transfer coef-

Table 4
Effect of melt temperature on temperature distribution, width of transition zone (from liquidus to solidus) and mushy zone (from 30% solid fraction to solidus), and sump depth in DC-cast Al–2.8 wt% Cu billets [7].

Practice	Casting speed (mm/min)/ T1 (°C)	T2/T3 (°C)	Width of transition zone (mm) centre/ periphery	Width of mushy zone (mm) centre/ periphery	Sump depth (mm)
Steady	200/700	675/675	145/13	24.5/7	166
Transient *		695/675	100/13	11/7	123
Steady	200/760	725/725	138/13	23/7.5	169
Transient *		750/725	92/13	11/7.5	125

* Ramping rate in the transition mode 113.2 mm/min^2.

ficient, h_{eq}, of the DC billets can be expressed as [134]:

$$\frac{1}{h_{eq}} = \frac{1}{h} + \frac{\sqrt{\pi t}}{\varepsilon_{th}} \tag{4.1}$$

where ε_{th} is the thermal diffusivity of the cast materials. This equation corresponds to the overall thermal resistance, which consists of the thermal resistance at the surface and that within the billet. The relative contribution from the thermal resistance at the surface, R_{surf}, is expressed as [134]:

$$R_{surf} = \frac{1/\mathrm{h}}{1/h_{eq}} \tag{4.2}$$

It was found that R_{surf} is high in the start-up phase, but then it drops to less than 5% in the steady phase. This means that above 95% of the thermal resistance is provided by the heat transfer within the billet. Increasing the water flow rate is meaningful only during the start-up phase of DC casting. At this stage, the water flow rate is rather low and stable film boiling occurs to form a vapour layer to insulate the billet surface [135]. Once this vapour layer breaks down at the Leidenfrost temperature [134,136], R_{surf} becomes below 5% and the thermal resistance at the surface becomes negligible.

As reported in Section 4.2.2, the sump depth is a crucial parameter for the development of hot tearing. Prasso et al. [7] found that the water flow rate exerts only a small influence on the sump depth, i.e., a decrease in the water flow rate by 20% causes the deepening of the sump by only 4%. Eskin et al. [137] demonstrated that the water flow rate can affect the depth of the sump, but only at low casting speeds. It is concluded that the water flow rate influences the hot tearing susceptibility only during the start-up phase of the DC casting and its effect is limited.

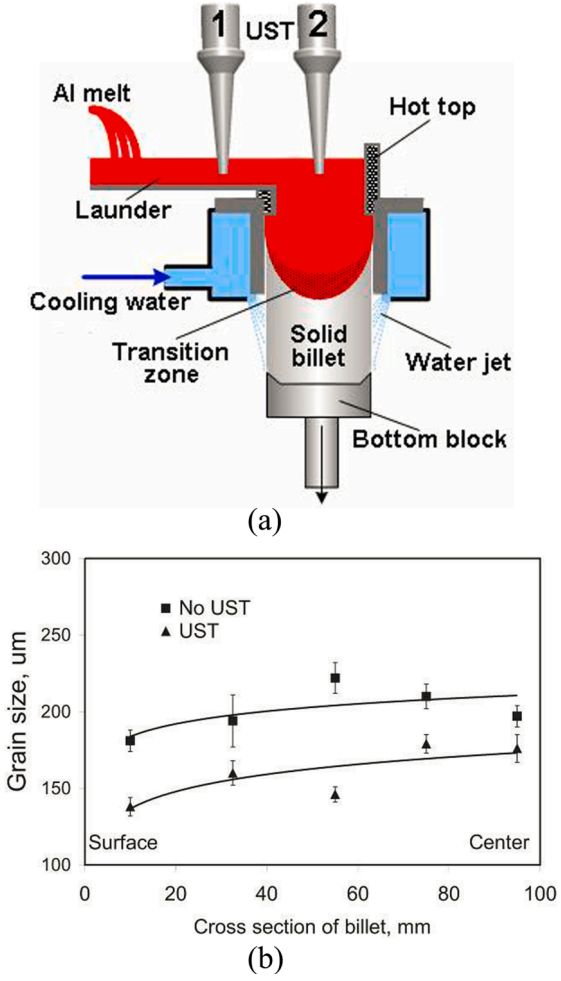

Fig. 4.11. (a) Schematic of DC casting setup with UST; (b) distribution of grain size in the horizontal section of a DC-cast AA7050 billet with and without UST [71].

4.2.5. Ultrasonic and electromagnetic treatments

The application of UST to the DC casting can help refine grains, alleviate the macro-segregation, and improve the surface quality in large billets/ingots [138,139]. Zhang [71] systematically investigated the effect of the UST on the grain size and morphology in a DC-cast AA7050 billet. A schematic of the laboratory scale DC casting setup with UST is shown in Fig. 4.11(a). Ultrasonic processing in the launder makes the grains finer and eliminates columnar grains (Fig. 4.11(b)), which decreases the linear contraction during solidification (Fig. 3.5). This results in a lower hot tearing susceptibility, as confirmed experimentally by Zhang et al. in a laboratory-scale DC-cast AA7050 billet [101]. For more information regarding the UST technology, the readers can refer to Ref. [138].

In addition to the UST, the LFEC is another efficient way to reduce the grain boundary segregation, refine the grain size, and improve the surface quality of DC-cast billets, especially in high-alloying 7xxx alloys. Researchers [140–142] have investigated the effect of LFEC on the hot tearing susceptibility in some 7xxx alloys in laboratory-scale DC casting. Under the LFEC condition, the alloying element distributions become uniform, the grains become finer and have a uniform spherical shape, and the sump depth reduces. Therefore, the centre of the billet is subject to lower tensile stresses compared to that in conventional DC casting. The LFEC decreases the size and fraction of the eutectics along grain boundaries, and a thinner liquid film exists at grain boundaries, which can increase the semi-solid tensile strength. All these factors help decrease the hot tearing susceptibility of a DC-cast billet.

5. Hot tearing simulations, criteria, and mechanisms

5.1. Hot tearing simulations

Determining the optimal casting recipe through trial and error to produce sound cast aluminium products without hot tears is a time-consuming and expensive process. With the development of computer and software technology, the fluid-flow velocities, stresses, strains and temperatures during DC and shape casting are being widely modelled. At present, many commercial multi-physics simulation packages are available, including ANSYS, ABAQUS, MSC Marc, and ALSIM [8]. The key to successfully simulate the hot tearing process is the application of an appropriate constitutive equation to describe the complex deformation behaviour of the mushy zone. The relevant work is discussed in the following subsections.

5.1.1. Constitutive models of semi-solid aluminium alloys

Section 3.3 has summarised the mechanical properties of different semi-solid aluminium alloys. These data can be used to understand the deformation mechanisms of semi-solid materials as well as to build different casting process models and formulate hot tearing criteria. Over the years, several equations have been developed to describe the constitutive behaviour of semi-solid aluminium alloys. In principle, the ideal constitutive equation should be able to describe the complex behaviour of the mushy zone from the low solid fraction at the rigidity point (Section 3.4) to the fully solid state. This complex behaviour embraces some features pertaining to suspensions (close to the rigidity point) and the viscoplastic behaviour at high solid fractions.

5.1.1.1. The extended creep-law-based constitutive equation. Initially, a simple approach was developed by extending the creep law of the solid materials to describe the semi-solid materials [18,19]. Braccini et al. [19] applied the exponential creep law of the solid phase to describe the semi-solid constitutive behaviour by assuming that the solid skeletons can withstand all of the loadings. The extended creep law is expressed as:

$$\sigma = \sigma_o \exp(\alpha f_s) \exp\left(\frac{mQ}{RT}\right) (\dot{\varepsilon})^m \tag{5.1}$$

where σ is the stress; σ_o and α are the materials constants; f_s is the solid fraction; m and Q denote the strain rate sensitivity coefficient and activation energy, respectively, which are obtained by the solid phase deformation experiments, R is the gas constant; T is the temperature; $\dot{\varepsilon}$ is the strain rate. This equation has been employed by Suyitno et al. [110,143–145] to simulate the DC casting process by using a finite element method and laboratory-scale experiments [146]. The simulation results are presented in Section 5.1.2.

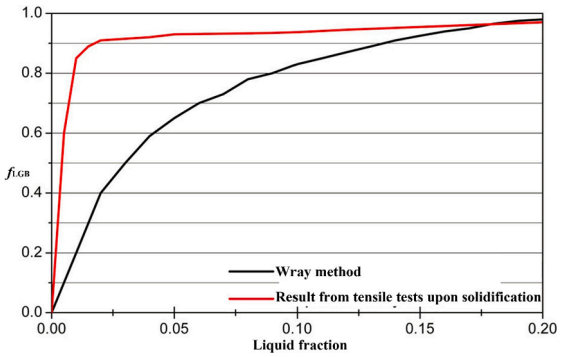

Fig. 5.1. Fraction of grain boundary area covered by liquid phases (f_{LGB}) from Wray method and tensile tests under solidification [111].

Drezet and Eggeler [19] extended the exponential creep law to make the load-carrying area directly proportional to the solid fraction. The equation is expressed as follows:

$$\dot{\varepsilon} = A(\frac{\sigma}{f_s})^n \exp(-\frac{Q}{RT}) \tag{5.2}$$

where A is a material constant, f_s is the solid fraction, and n is the stress exponent. Considering the phenomenon that the low melting phases are located at grain boundaries, van Haaften et al. [18] replaced f_s with $(1 - f_{LGB})$, where f_{LGB} is the amount of grain boundary area covered by the liquid phases. The improved equation is expressed as:

$$\dot{\varepsilon} = A(\frac{\sigma}{1 - f_{LGB}})^n \exp(-\frac{Q}{RT}) \tag{5.3}$$

The material parameters$A$, n, and Q can be determined by the tensile tests at the solidus temperature. f_{LGB} is closely related to the evolution of the liquid distribution with the solid fraction. Wray [111] derived the dependence of f_{LGB} on the solid fraction (above 0.9) by assuming the tetrahedral liquid pockets and perfect wettability of the solid by the liquid. The predictions obtained using Wray's data were in agreement with those obtained in the semi-solid tensile experiments under reheating for AA3104 and AA5182 (Fig. 3.23) [18] and AA6056 with 2 wt% Si [41]. A rather poor prediction was obtained using Wray's data in the tensile tests under solidification for AA6056 [41] and AA6061 [34]. This is attributed to the difference in the number of grain boundaries wetted by the liquid in the two conditions. As mentioned in Section 3.3.1, the liquid phases are more prone to stay as films along grain boundaries at the same solid faction under solidification than under reheating. This results in different dependency on f_{LGB} on the liquid fraction in two conditions, as shown in Fig. 5.1. The variance of f_{LGB} with the liquid fraction has been applied to model the hot tearing propagation along coalesced grain boundaries in a recently proposed hot tearing criterion (Section 5.2.2.1).

In the modified creep laws, it was assumed that the load is transferred only by the solid phases. This assumption would become unsuitable when a significant number of grain boundaries are wetted with the liquid phases, i.e., at the low solid fraction corresponding to the rigidity point, where the solid-liquid mixture tends to a Newtonian-like behaviour.

5.1.1.2. The viscoplastic based constitutive equation. Another approach to consider the effect of the liquid is based on the viscoplastic solid mechanics. It is assumed that the cohesion of the solid network is reduced by the existence of liquid. The total strain (ε_{total}) can be divided into three parts: elastic (ε_e), thermal (ε_T), and viscoplastic (ε_P) parts. Thus,

$$\varepsilon_{total} = \varepsilon_e + \varepsilon_T + \varepsilon_P \tag{5.4}$$

The elastic strain is calculated as:

$$\sigma = E\varepsilon_e \tag{5.5}$$

where E is Young's modulus. The thermal strain can be calculated by Eq. (3.4). To describe the viscoplastic behaviour of semi-solid materials, a cohesion constitutive equation was proposed by Martin and co-workers [20,21]. It is assumed that the semi-solid materials consist of a porous solid skeleton filled with liquid phases. An internal variable C is introduced to describe the partial cohesion of the porous material, i.e., the degree of dendrites interlocking. This viscoplastic equation is given:

$$\dot{\varepsilon}_P = \frac{\dot{\varepsilon}_0}{(CS_0)^n}\left[-\frac{A_2(f_s)}{3}\overline{P}_s^2 \mathrm{I} + \frac{3}{2}A_3(f_s)\mathrm{S}_s\right]\left[A_2(f_s)\overline{P}_s^2 + A_3(f_s)\overline{\sigma}_s^2\right]^{\frac{n-1}{2}} \tag{5.6}$$

where S_0, $\dot{\varepsilon}_0$, and n are material constants which can be obtained by the high-temperature tensile tests of the fully solid materials. $\overline{P}_s$ is the effective pressure on the solid skeleton. S_s is the solid phase deviatoric effective stress tensor. $\overline{\sigma}_s$ is the Von Mises stress. The solid fraction functions $A_2(f_s)$ and $A_3(f_s)$ represent the softening effect of the liquid in the form of pockets, while the softening effect due to the existing of the liquid films at grain boundaries is considered by the internal variable C. The alloy-dependent parameter C can be determined by rheological experiments. Recently, an additional internal variable D was introduced into this model to account for the opening up, decohesion of the solid skeleton which is related to the initiation of hot tears during semi-solid tensile tests [147]. The relevant semi-solid constitutive parameters for this viscoplastic model of Al-Cu [21], AA5182 [20], AA6061 [34], AA7050 [8] alloys have been reported by researchers. The elastic-viscoplastic constitutive function has been applied to model both laboratory-scale [63,69,148,149] and industrial DC casting [8,69,111,150,151] experiments. The simulation results are presented in Section 5.1.2.

In the two kinds of models, the development of the liquid distribution with the solid fraction has been considered by internal variables such as f_{LGB} for van Haaften's model and C for the viscoplastic model. These variables need to be accurately measured by semi-solid tensile experiments. Similar to the variances of f_{LGB} in Fig. 5.1, the value of C in the reheating conditions is higher than that in solidification conditions, suggesting that fewer liquid films exist at grain boundaries under the same solid fraction. Compared to these two methods, the simple modified creep laws based model may fail at high liquid fractions while the complex-style viscoplastic model is more appropriate to model the entire solidification process (both during and after solidification) via changing the value of C. When the fully solid state is achieved, the value of C is equal to one.

5.1.1.3. Phillion et al.'s constitutive equation. The above-mentioned two models only consider the effect of the strain rate and temperature and not the influence of the microstructure features and defects. Based on the predictions from a finite element simulation of

the semi-solid tensile deformation by using a sophisticated granular microstructure model [152], Phillion et al. [22] proposed a semi-solid constitutive equation for AA5182 which firstly takes into account the effects of the solid fraction, f_s, strain rate, $\dot{\varepsilon}$, grain size, $\overline{d}$, and porosity fraction, f_p, on the semi-solid tensile deformation. The new constitutive relationship for AA5182 in the solid fraction range, $0.75 < f_s < 0.95$, is:

$$\sigma = K_p(f_s\sigma_s)\left(\varepsilon_p + \varepsilon_0\right)^n(1 - f_p/(1 - f_s)) \tag{5.7}$$

$$\sigma_s = (483.5 - 0.77T)\dot{\varepsilon}^{0.205+0.00006T} \tag{5.8}$$

$$n = -6.35 \times 10^{-4}h^2 + 0.0202h \tag{5.9}$$

$$h = \overline{d}(1 - f_s^{1/3}) \tag{5.10}$$

where σ is the stress; K_p is the porosity proportionality coefficient; σ_s is the solid flow stress; ε_p is the plastic strain; ε_0 is the initial strain such that $\sigma(\varepsilon_p = 0) = \sigma_{yield}$; T is the temperature; and $\dot{\varepsilon}$ is the strain rate. n is a function of the intergranular liquid channel thickness, h. The solid fraction has the most important effect on the semi-solid constitutive behaviour, followed by the grain size and then porosity fraction. Because the local values of the solid fraction, porosity fraction and grain size can be calculated by relevant methods, the proposed constitutive equation allows the constitutive behaviour to change as a function of solidification conditions. The constitutive law has been applied to simulate the DC casting process for AA5182 and investigate the effect of various microstructure features (grain size and rigidity point) and process parameters (casting speed) [132], as discussed in Section 5.1.2.

5.1.2. Modelling results

Based on the aforementioned semi-solid constitutive models, many DC casting process simulations have been performed to predict the temperature, fluid-flow, and stress/strain fields in a billet/ingot under different process parameters. The relevant results are summarised in the following text.

5.1.2.1. Thermomechanical simulations in round billets. Suyitno et al. [143] predicted the temperature evolution of different locations in a DC-casting 200-mm Al-4.5 wt% Cu round billet, as shown in Fig. 5.2. First, the computed result matches well with the experimental results (curves 4 and 5). The surface of the billet (curve 5) has a lower temperature and a higher cooling rate than the centre (curve 1). Suyitno et al. [143] further predicted the stress distributions during the steady-state stage in this round billet using Eq. (5.1). The results are shown in Fig. 5.3. During solidification, the radial (2) and circumferential (3) tensile stresses prevail at the centre of the billet, while only the circumferential (6) tensile stresses occur at the periphery. This explains why the hot tear most likely occurs in the centre of a billet and propagates along the axial (normal to radius) and radial (normal to circumference) directions, as shown in Fig. 4.7 (c).

5.1.2.2. Effect of the casting speed on the thermomechanical behaviour. Based on Eq. (5.1), Suyitno et al. [143,144] predicted the effect of the casting speed-ramping on the thermomechanical and hot tearing behaviour in a DC-casting 200-mm Al-4.5 wt% Cu alloy round billet. The results are illustrated in Fig. 5.4. A strong relationship can be observed between the predicted hot tearing susceptibility

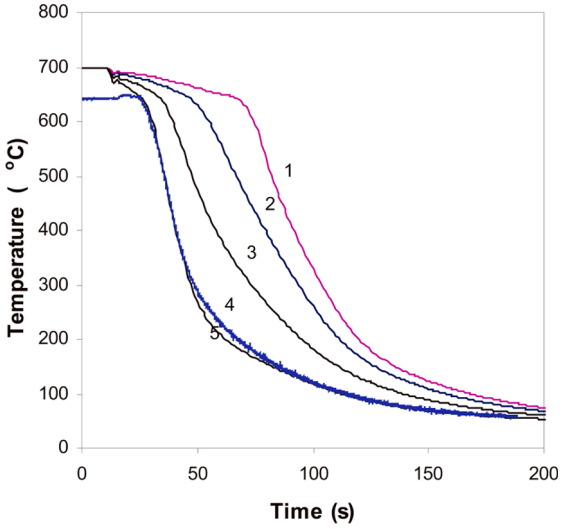

Fig. 5.2. Temperature evolutions with the time of different radial distances in a DC-casting 200-mm Al-4.5 wt% Cu round billet (casting speed: 120 mm/min): (1) 0 mm, (2) 50 mm, (3) 70 mm, (5) 90 mm and (4) measured temperature at 90 mm [143].

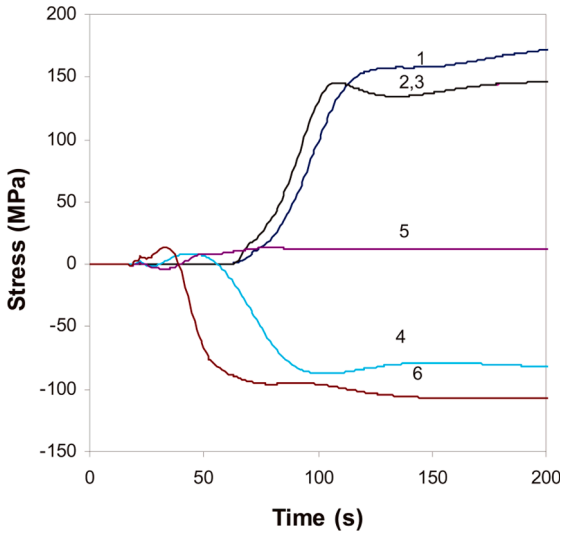

Fig. 5.3. Calculated stresses development during steady-state stage in a DC-casting 200-mm Al-4.5 wt% Cu round billet (casting speed: 120 mm/min): axial (1), radial (2) and circumferential (3) stresses at the centre of the billet, and axial (4), radial (5) and circumferential (6) stresses at the periphery (10 mm from the surface) [143].

based on the SKK criterion (Section 5.2.2.1), development of tensile stresses and strains, depth of the sump, and length of the mushy zone along the centre line of the billet. When the sump depth at the centre of the billet becomes wider, the thermal gradient between the centre and surface of the billet increases, which leads to higher tensile stresses and strains. This will increase the possibility of the occurrence of hot tearing. The start-up mode 3 in Fig. 5.4(a), which is the most rigid casting practice, shows the highest tensile stress and strain (Fig. 5.4(c) and (d)) as well as the maximum sump depth and mushy zone length (Fig. 5.4(e) and (f)), leading to the maximum hot cracking susceptibility (Fig. 5.4(b)). The slowest start-up mode 2 in Fig. 5.4(a) produces more moderate stresses and strains (Fig. 5.4(c) and (d)) as well as the minimum sump depth and mushy zone length (Fig. 5.4(e) and (f)), which results in the minimum hot cracking susceptibility. In addition, M'hamdi et al. [153] investigated the effect of different initial casting speeds on the thermomechanical and hot tearing behaviour in the DC-casting of an AA6060 alloy using a simplified viscoplastic equation. The calculated viscoplastic strain rate exhibits a good correlation with the measured hot tearing susceptibility, while the calculated accumulated strain does not well predict the severity of the centre cracks. Similarly, based on Eq. (5.7), Mathier et al. [69] highlighted that the calculated volumetric strain rate is a better indicator of the hot tearing susceptibility than the calculated accumulation strain for DC-cast billets. It suggests that the strain rate plays a more prominent role in the formation of hot tears.

By comparing the thermomechanical situation at the steady state in Fig. 5.4, a common phenomenon can be observed that increasing the casting speed promotes the stress/strain development, widens the depth of the sump and length of the mushy zone in the centre of the billet, and thereby increases the hot tearing susceptibility.

Thermal inertia often occurs in the transient initial stage of a DC casting. The magnitude of the thermal inertia can be revealed by the sump depth, as mentioned in Section 4.2.2. Du et al. [154] calculated the effect of different ramping rates on the evolutions of the sump depth. The results are shown in Fig. 5.5. Nearly real-time response of the sump depth to the ramping casting rate is obtained in mode 4, while mode 1 exhibits an extremely large delay. Thus, the ramping rate is an obvious controlling parameter that determines the magnitude of the thermal inertia. As mentioned the sump depth is a better indicator of hot tearing than the casting speed.

5.1.2.3. Effect of the microstructure variations on the thermomechanical behaviour. Based on Eq. (5.7), Jamaly et al. [132] investigated the effect of the fixed and variable grain size distributions on the thermomechanical behaviour in an AA5182 alloy billet. A "hot tearing strain", ε_{HT}BTR, was defined as the accumulated strain within the solid fraction of 0.98 and rigidity point where the ductility was close to zero. If $\varepsilon_{HT}\text{BTR} > 0$, a hot tear was likely to occur. Fig. 5.6(a) shows the variation of the hot tearing strain in the cross-section close to the bottom block. The maximum hot tearing strain occurs in the centre for all cases and is tensile. The hot tearing strain is also tensile close to the surface of billet, which suggests that hot tearing is prone to occur in the centre and the surface. Case A with the variable grain size exhibits the highest strain value, while case D shows the smallest value. This is due to the variation in the yield strength existing in case A. Overall, this study stresses the importance of incorporating the grain size dependency into the constitutive equations. This equation should be widely applied to more alloying systems considering the dramatic microstructure variances in DC castings. In the future, it is suggested to couple reliable as-cast grain size prediction models [128,155] with this grain-size-dependent constitutive equation to perform DC casting process simulations. Other microstructure features like dendritic grains and eutectics may also be considered in the simulations.

Jamaly et al. [132] highlighted the effect of the rigidity point and casting speed on the hot tearing strain close to the bottom block, as shown in Fig. 5.6(b). In the initial transient stage, ε_{HT}BTR increased as the rigidity temperature decreased from 602 to 580 °C, which suggested that hot tears are more prone to occur. This is contrary to the phenomenon observed in grain-refined alloys that a decreased

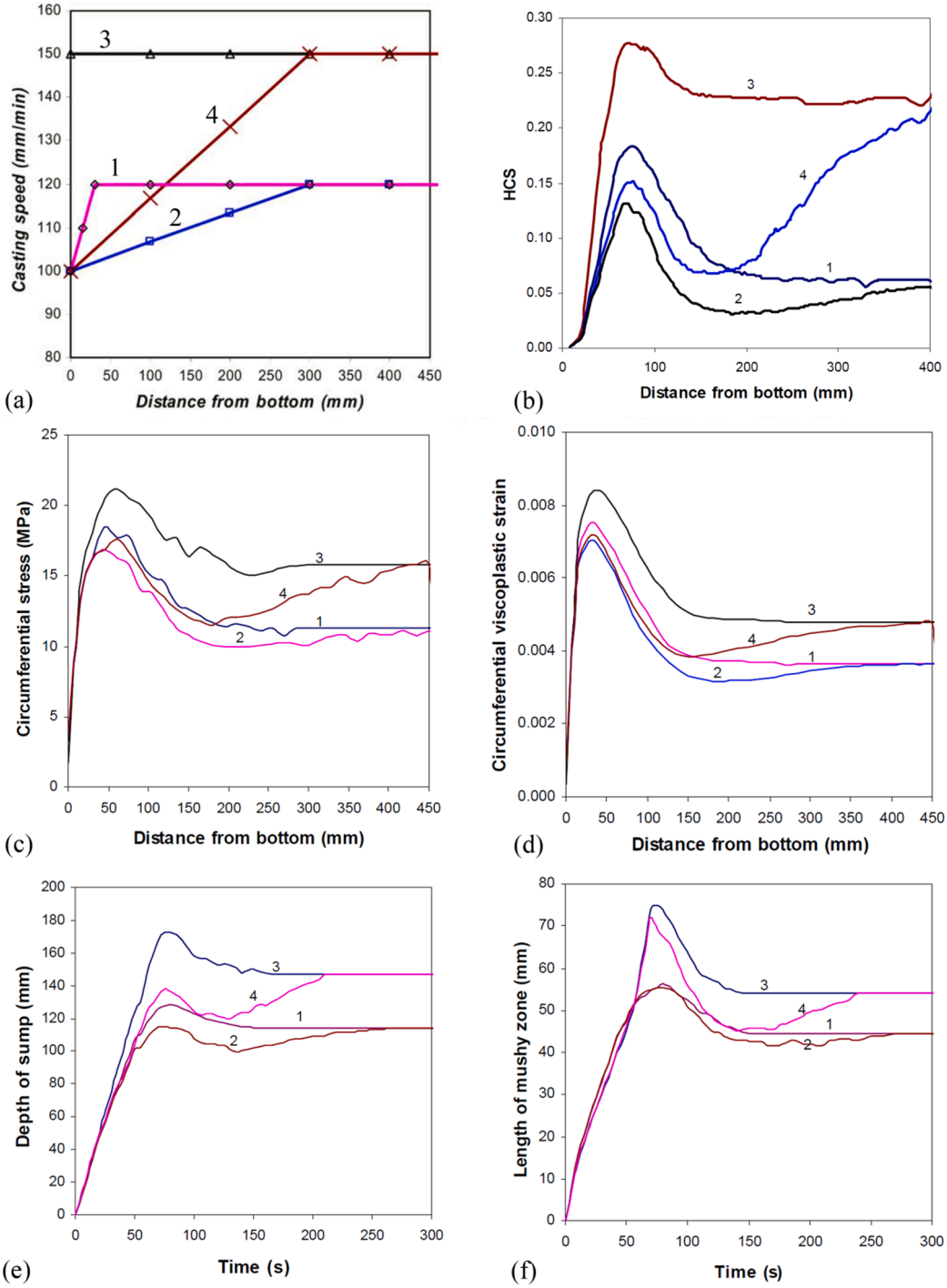

Fig. 5.4. Thermomechanical simulations of a DC-casting 200-mm Al–4.5 wt% Cu alloy billet: (a) case studies on casting-speed ramping in the start-up phase of casting; corresponding developments of (b) predicted HCS, (c) circumferential stress, (d) circumferential strain at solidus temperature, (e) depth of sump, and (f) length of mushy zone in the centre of the billet [143,144].

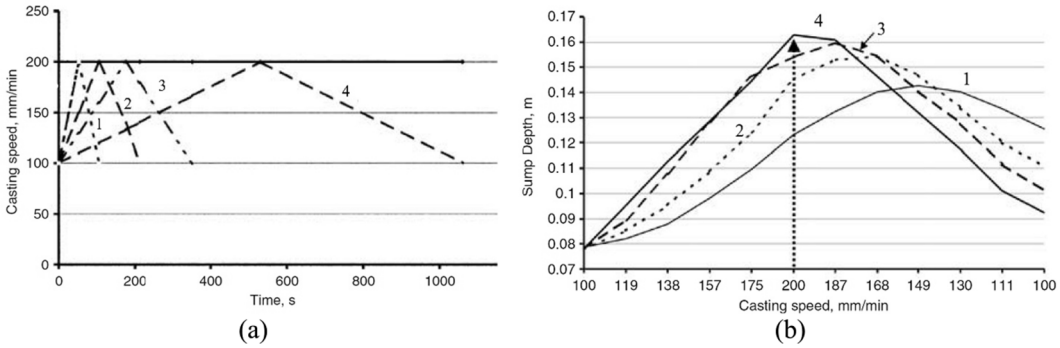

Fig. 5.5. (a) Four kinds of ramping casting modes, (b) effect of different ramping casting rates on the evolutions of the calculated sump depth in a 200-mm Al–4 wt% Cu billet [154].

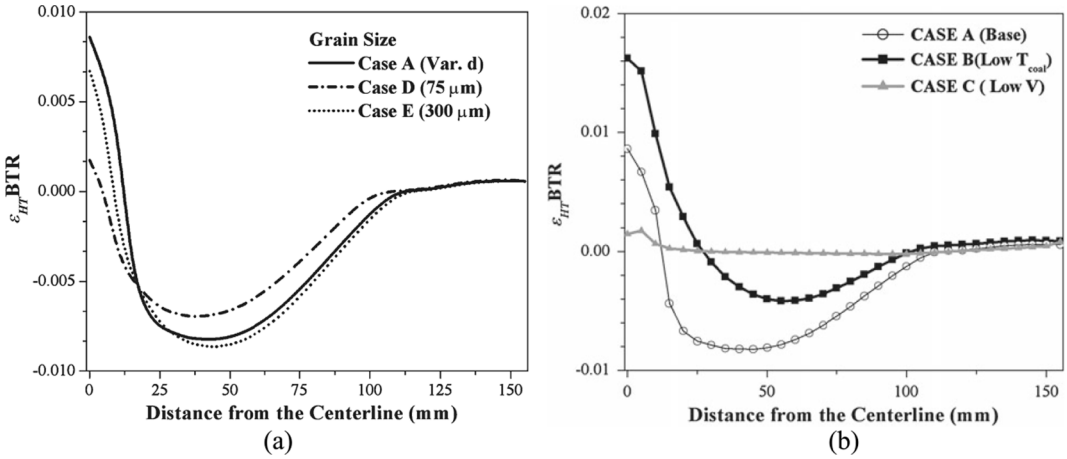

Fig. 5.6. Variation of ε_{HT}BTR in the cross-section close to the bottom block: the effect of (a) grain size as well as (b) rigidity point and casting speed [132].

rigidity temperature always accompanies with the lower hot tearing susceptibility, because the present simulations changed only the rigidity point and not the grain size, while both of them changed in grain-refined alloys. In addition, only a small amount of ε_{HT}BTR is accumulated at the low casting speed due to a low temperature gradient.

In summary, the state-of-the-art high-throughput computing techniques should be applied to multi-scale simulations to reduce the calculation times. Machine learning has been playing important role in different research fields like molecular dynamics calculation [156,157] and will also bring opportunities for multi-field simulations and hot tearing predictions.

5.2. Hot tearing criteria

5.2.1. Development history of hot tearing criteria

Various hot tearing criteria have been proposed in the past years. These criteria can be classified into two categories: mechanical and nonmechanical criteria. The former criteria contain those based on the critical stress, critical strain, and critical strain rate. The latter criteria involve the vulnerable temperature zone, phase diagram, and process parameters. Eskin et al. [15] have reviewed the details of these criteria in 2004, as summarised in Table 5 along with their applications in hot tearing predictions. It can be found that these criteria mostly succeed in predicting the effect of the compositions on the hot tearing susceptibility but fail to predict the effect of the process parameters. Since 2004, the researchers have focused on both these aspects, and the hot tearing criteria have been developed to predict both the severity and the initiation and propagation of hot tears, especially during DC casting. These studies have advanced the domain beyond simple criteria to more quantitative hot tearing predictions.

5.2.2. Recent hot tearing criteria

5.2.2.1. SKK criterion. Suyitno et al. [144] proposed a micro porosity-related hot tearing criterion called SKK criterion. In this criterion, several phenomena are considered. When the coherency point is reached, the liquid becomes increasingly isolated in separate

Table 5
Summary of hot tearing criteria before 2004 based on Ref. [15].

Category	Author(s)	Equation(s)	Comments	Applications
Stress-based criteria	Novikov	$\sigma_{fr} = 2\gamma/b$	$\sigma_{fr}$is the fracture stress γ is the surface tension b is the film thickness	
	Dickhaus et al.	$F = \frac{3\pi\mu R^4}{8t}(\frac{1}{b_1^2} - \frac{1}{b_2^2})b = \frac{(1-f_s)d}{2}$	Fis the force required to increase the thickness of the liquid film from b_1 to b_2 μ is the dynamic viscosity t is the time required to increase the film thickness from b_1 to b_2 f_s is the solid fraction d is the average thickness of a solidifying grains	
	Lahaie and Bouchard	$\sigma_{fr} = \frac{4\mu}{3b}(1 + \frac{f_s^m \varepsilon}{1-f_s^m})^{-1}$	mis equal to 1/3 for equiaxed and 1/2 for columnar structure ε is the strain	Success in predicting the effect of solid fraction, grain morphologies and size on the calculated fracture stress, but failure in their effect on the calculated fracture strain [15]
	Langlais and Gruzleski	$HTS = 1/\text{themaximumtensilestrength}$	HTSis the hot tearing susceptibility	Al-Si system [15]
	Williams and Singer	$\sigma_{fr} = \sqrt{\frac{8G\gamma}{\pi(1-\nu)AV_L^{0.5}}}$Modified equation: $\sigma_{fr} = \sqrt{\frac{16G\gamma}{\pi(1-\nu)(0.07D + 0.47AV_L^{0.5} + 0.37D^{0.5}V_L^{0.25})}}$	$\sigma_{fr}$is the fracture stress G is the shear modulus γ is the effective fracture surface energy V_L is the volume of liquid ν is Poisson's ratio A is a constant dependent on the grain size and the dihedral angle D is the grain diameter	Al-Sn system [15]; Failure in predicting the effect of grain size on the calculated fracture stress [15]
Strain-based criteria	Novikov	$P_r = \frac{S}{\Delta T_{br}}$If ε_{th} curve intersects ε_p curve in the vulnerable temperature range, $P_r = \frac{S_1 - S_2}{\Delta T_{br}}$	$P_r$is the reserve of plasticity in the solidification range S is the difference between the average integrated value of the elongation to failure (ε_p) and the linear contraction (ε_{th}) ΔT_{br} is the vulnerable temperature range S_1 is the area where ε_p minus ε_{th} S_2 is the area where ε_{th} minusε_p	Al-Cu-Li-(Mn) and 7xxx alloys [15]
	Magnin et al.	$HTS = \varepsilon_{\theta\theta}/\varepsilon_{fr}$If HTS > 1, a hot tear will occur.	$\varepsilon_{\theta\theta}$is the maximum principle plastic strain at the solidus temperature ε_{fr} is the measured strain at a temperature close to the solidus HTS is the hot tearing susceptibility	Success in predicting the effect of casting speed in a DC-cast Al-4.5 wt% Cu alloy [15]
Strain rate-based criteria	Prokhorov	$\frac{\Delta\varepsilon_{res}}{\Delta T_{br}} = \frac{D_{min} - (\Delta\varepsilon_{free} + \Delta\varepsilon_{app})}{\Delta T_{br}}\dot{\varepsilon}_{res} = \dot{\varepsilon}_{min} - \dot{\varepsilon}_{free} - \dot{\varepsilon}_{app}$If $\dot{\varepsilon}_{res} \leq 0$, a hot tear will occur.	$D_{min}$and $\dot{\varepsilon}_{min}$ is the minimum fracture strain and strain rate in ΔT_{br}, respectively	

(*continued on next page*)

Table 5 (*continued*)

Category	Author(s)	Equation(s)	Comments	Applications
			$\Delta\varepsilon_{res}$ and $\dot{\varepsilon}_{res}$ is the reserve of hot tearing strain and strain rate, respectively $\Delta\varepsilon_{free}$ and $\dot{\varepsilon}_{free}$is the free linear contraction and strain rate, respectively $\Delta\varepsilon_{app}$ and $\dot{\varepsilon}_{app}$ is the actual strain in the solidifying body and strain rate, respectively	
	RDG criterion	$\Delta P = \Delta P_{sh} + \Delta P_{mech} - \rho g h \Delta P_{sh} + \Delta P_{mech} = \frac{180\mu\Delta T}{G\lambda_2^2}\left[AV_T\beta + B\frac{(1+\beta)\dot{\varepsilon}\Delta T}{G}\right]A = \frac{1}{\Delta T}\int_{T_{end}}^{T_{mf}} \frac{f_s(T)^2}{(1-f_s(T))^2}dTB = \frac{1}{\Delta T}\int_{T_{end}}^{T_{mf}} \frac{f_s(T)^2 F(T)}{(1-f_s(T))^3}dTF(T) = \frac{1}{\Delta T}\int_{end}^{T} f_s(T)dT$If $\Delta P > \Delta P_c$, a hot tear will occur. $HTS = 1/\dot{\varepsilon}^{max}\dot{\varepsilon}^{max} = \frac{\lambda_2^2 G^2}{180(1+\beta)B\mu\Delta T^2}\Delta P_c - \frac{V_T\beta AG}{(1+\beta)B\Delta T}$	ΔPis the pressure drop over mush ΔP_{sh} and ΔP_{mech} is the pressure drop contributions in the mush due to the solidification shrinkage and the deformation induced liquid flow G is the thermal gradient λ_2 is the SDAS V_T is the casting speed β is the volumetric solidification shrinkage factor $\dot{\varepsilon}$ is the viscoplastic strain rate T_{mf} is the massive feeding temperature T_{end} is the temperature where bridging of the dendrite arms between grains occurs f_s is the volume fraction of solid ΔP_c is the critical cavitation pressure $\dot{\varepsilon}^{max}$ is the critical strain rate beyond which cavitation, i.e., nucleation of a first void, occurs HTS is the hot tearing susceptibility	Al-Cu system [161,190] Success in predicting the effect of casting speed and billet size in a DC-cast AA6063 alloy [161]
	Grandfield et al.	$HTS = 1/\dot{\varepsilon}^{max}\dot{\varepsilon}^{max} = \frac{\rho^2 G^2}{180(1+\beta)B\mu\Delta T^2}\left[P_m + \frac{4\gamma}{d(1-\sqrt[3]{f_{s,co}})}\right] - \frac{V_T\beta AG}{(1+\beta)B\Delta T}\rho =$ $\begin{cases}\lambda_2 : equiaxed grains\\ d : cellular grains\end{cases}$	$P_m$is the metal head pressure $f_{s,co}$ is the coalescence solid fraction d is the grain size	AA6061 with different Ti contents [66] and cooling rates [125] Al-Mg-Si system [64] AA6060 with different Fe contents [29] Al-Zn-Mg-Cu system [78]
	Braccini et al.	$\dot{\varepsilon}^c = \left(1-\frac{e}{l}\right)\left[\frac{\lambda-a}{\lambda}\left(\frac{\frac{2}{3}P_c - P_M}{K(T,f_s)}\right)\right]^{\frac{1}{m}} + \frac{e}{l}\frac{2\kappa}{(\lambda-a)^2}\frac{P_c}{\mu}$	$\dot{\varepsilon}^c$is the critical strain rate for hot tearing e is the liquid film thickness l is the gage length λ is the half grain size a is the length of the tear K is the constitutive parameter as a function of temperature T and solid fraction f_s m is strain-rate sensitivity κ is the permeability of the mushy zone P_c is the cavitation	

(*continued on next page*)

Table 5 (*continued*)

Category	Author(s)	Equation(s)	Comments	Applications
			pressure P_M is the metallostatic pressure	
Nonmechanical criteria	Feurer	$SPV = \frac{f_l^2 \lambda_2^2 P_s}{24\pi C^3 \eta L^2} SRG = \frac{\partial \ln V}{\partial t} = -\frac{1}{\rho}\frac{\partial \overline{\rho}}{\partial t}$ If SPV < SRG, a hot tear will occur.	SPV is the maximum volumetric flow rate (feeding term) through a dendritic network SRG is the volumetric solidification shrinkage, respectively (shrinkage term) f_l is the volume liquid fraction P_s is the effective feeding pressure C is the tortuosity constant of dendrite network L is the length of the porous network $\overline{\rho}$ is the average density of the mush V is the volume element of the solidifying mush with constant mass t is the time	Al-5Si [15]
	Clyne and Davies	$HTS = \frac{t_v}{t_r} = \frac{t_{0.99} - t_{0.9}}{t_{0.9} - t_{0.4}}$	$t_v$is the vulnerable time period (hot tearing) t_r is the time available for stress relief process (mass and liquid feeding) $t_{0.99}$, $t_{0.9}$, and $t_{0.4}$ is the time when the volume fraction of solid is 0.99, 0.9, and 0.4, respectively	Al-Cu system [7] Al-Mg system [15] Various commercial aluminium alloys (1xxx-7xxx) [15] Failure in predicting the effect of casting speed and billet size in DC-cast AA6063 [161] and Al-4.5 wt% Mg alloys [15]
	Katgerman	$HCS = \frac{t_{0.99} - t_{cr}}{t_{cr} - t_{0.4}}$ Modified equation: $HCS = \frac{t_{0.99} - t_{cr}}{t_{cr} - t_{coh}}$	$t_{cr}$is calculated using Feurer's criterion when SPV is equal to SRG t_{coh} is the time when the coherency temperature is achieved	Al-Mg system [15] Various commercial aluminium alloys (1xxx-7xxx) [15] Success in predicting the effect of casting speed but failure in the effect of ingot size in a DC-cast Al-4.5 wt% Mg alloy [15]

locations of the mush and eventually, cavities may form at the triple junctions of grain boundaries as a result of the solidification shrinkage, thermal contraction, and low permeability [7]. Three possible phenomena may occur in the last solidification stage. First, the liquid flow and later high-temperature creep completely compensate for the solidification shrinkage and thermal contraction and, therefore, cavities are not formed and a fully dense porosity-free structure is generated. Second, the feeding capacity is limited and the cavities develop into pores. The interplay between the feeding and shrinkage/contraction is responsible for the shift between the first and second phenomena. The shrinkage/contraction rate *fr* is defined as

$$fr = -\left(\frac{\rho_s}{\rho_l} - 1\right)\frac{\partial f_l}{\partial t} + \left(\frac{\rho_s}{\rho_l}\right)\dot{\varepsilon} \tag{5.11}$$

where ρ_s and ρ_l denote the solid and liquid densities, respectively; f_l is the liquid fraction; t is the time; $\dot{\varepsilon}$ is the strain rate. The feeding rate *fe* is expressed as:

$$fe = K\frac{P}{\eta L^2} \tag{5.12}$$

$$K = \frac{\lambda^2(1 - f_s)^3}{180 f_s^2} \tag{5.13}$$

$$P = P_a + P_m - \frac{4\gamma_{sl}}{\lambda} \tag{5.14}$$

where K is the permeability; P is the feeding pressure; η is the viscosity of liquid; L is the mushy zone length; λ is the SDAS; f_s is the solid fraction; P_a and P_m are the atmospheric pressure and metallostatic pressure, respectively; and γ_{sl} is the solid-liquid interfacial energy. The cavity fraction f_v can be expressed as:

$$-\frac{\rho_s}{\rho_l}\frac{\partial f_v}{\partial_T}\dot{T} = \left(\frac{\rho_s}{\rho_l} - 1\right)\frac{\partial f_l}{\partial_T}\dot{T} + \left(\frac{\rho_s}{\rho_l}\right)\dot{\varepsilon} - fe \tag{5.15}$$

$$f_v = \int_{T_{crit}}^{T} \frac{\partial f_v}{\partial_T} dT \tag{5.16}$$

where $\dot{T}$ is the cooling rate; T_{crit} is the critical temperature where the feeding rate fe is equal to the shrinkage/contraction rate fr. The cavity size d is given:

$$d = \left(\frac{3c}{2\pi} f_v d_g^3\right)^{1/3} \tag{5.17}$$

where c is chosen as $2\sqrt{2}$ for aluminium alloys; d_g is the grain size.

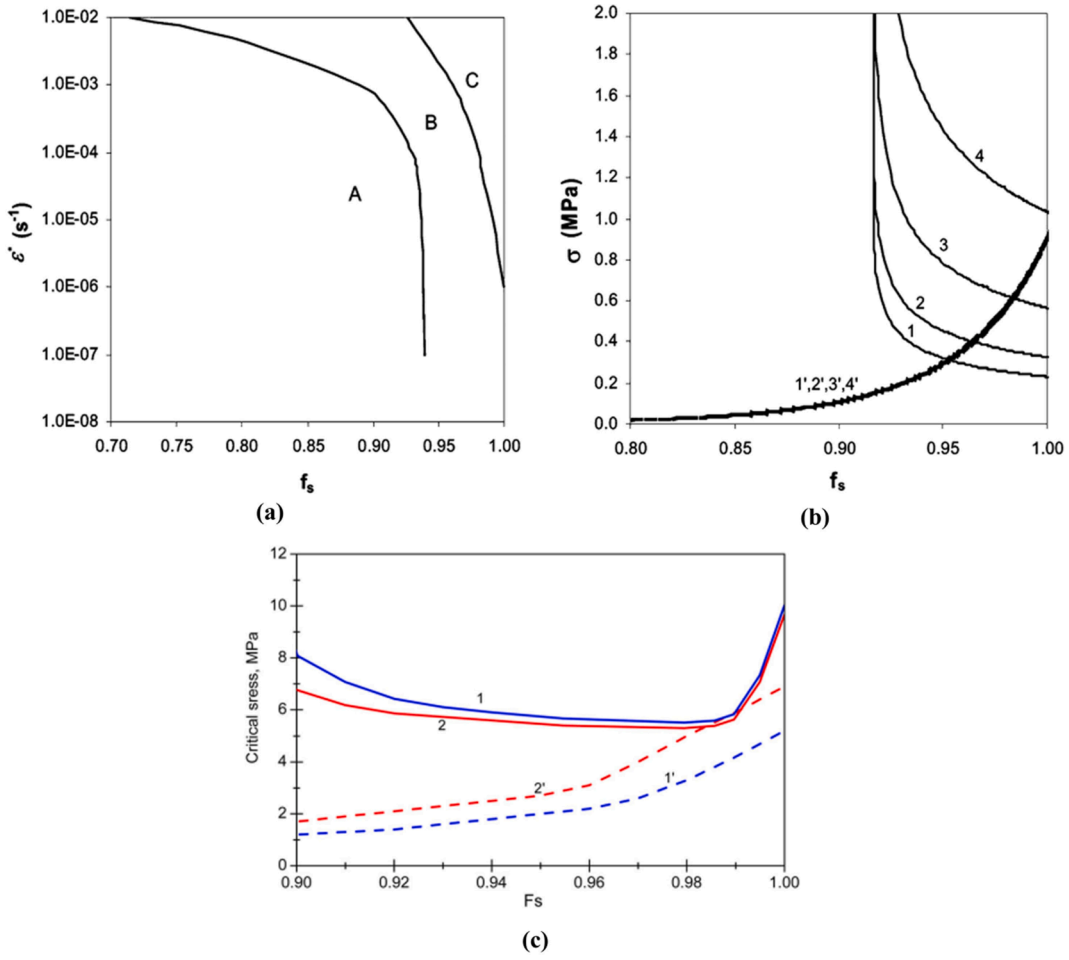

Fig. 5.7. (a) Three regions (A = micro-pores and hot tears are absent, B = micro-pores develop but hot tears do not form, and C = hot tears are formed); (b) effect of grain size on the developed stress in the mush (1'-4') and the critical stress (1–4): 1,1', 600 μm; 2,2', 300 μm; 3,3', 100 μm; and 4,4', 30 μm; (c) effect of casting speed on the developed stress (dash line) in the mush and the critical stress (solid line): 1,1', 25 mm in^{-1} and 2,2', 35 mm min^{-1} [111,144].

Third, when the cavity size d exceeds a critical size a_{crit}, hot tearing occurs. a_{crit} is determined by using the modified Griffith criterion:

$$a_{crit} = 4\gamma_l \frac{E}{\pi\sigma^2} \tag{5.18}$$

where γ_l is the surface energy of the liquid phase; E is Young's modulus of the semi-solid; and σ is the tensile stress.

The hot tearing susceptibility (*HTS*) is defined as:

$$HTS = \frac{d}{a_{crit}} \tag{5.19}$$

When $HTS > 1$, hot tears occur. Otherwise, only micro-pores are generated. As a result, it is possible to simultaneously predict the occurrence of micro-pores and hot tears, as shown in Fig. 5.7(a). This criterion works well in considering the change in the deformation rate, cooling rate, grain size, casting speed, and casting recipe [144]. An example of the effect of the grain size is shown in Fig. 5.7(b). It is observed that the critical fracture stress increases obviously with the grain refinement and below a certain grain size, hot tearing does not occur. Recently, the SKK criterion was applied to predict the compositional sensitivity of hot tearing in grain-refined Al-Mg-Zn-Cu alloys using the measured load developments upon solidification [77]. The complex hot tearing tendency (Fig. 3.14) of this quaternary system was successfully predicted.

The SKK criterion always predicts an increasing hot tearing tendency during solidification with a high value at the solidus temperature, which does not agree well with the casting practice. This is due to the assumption that all the grains are surrounded by a liquid film during the entire solidification transformation. It is known that certain grain bridges are formed in the last stage of solidification. Recently, Bai et al. [111] improved this criterion by considering the effect of the solid bridging/grain coalescence, which plays an important role during hot tear propagation. Two important parameters were introduced into the criterion, including the fraction of the grain boundaries covered by liquid (f_{LGB} in Eq. (5.3)) and the solid energy term (U_s), representing the energy to be overcome for the hot tearing to propagate along the coalesced grain boundaries. The critical cavity dimension to cause hot tearing under tensile stress σ is modified:

$$a_{crit} = 4[\gamma f_{LGB} + U_s(1 - f_{LGB})]\frac{E}{\pi\sigma^2} \tag{5.20}$$

This modified criterion responses well to the change in the deformation rate, cooling rate, grain morphology and casting speed [111]. An example of the effect of the grain size and casting speed is shown in Fig. 5.7(c). It can be seen that the critical stress displays an irregular "U" type curve towards the end of solidification. In the left side of the curve, the critical stress decreases with the increase of solid fraction while it increases on the right side. The former is due to the decreased liquid feeding while the latter is attributed to more developed grain coalescence in the mushy zone. The evolution of the critical stresses obtained with the modified criterion is different from the result from the original SKK criterion (Fig. 5.7(b)). It leads to a decreased hot tearing tendency close to the solidus, which is in accordance with the industrial practice. Note that it is crucial to measure the variance of f_{LGB} with liquid fractions (as in Fig. 5.1) and consider the effect of the grain coalescence, especially when predicting the effect of the impurities (Section 4.1).

5.2.2.2. Two-phase model. A sophisticated two-phase model was suggested by M'Hamdi et al. [150]. In this strain-based criterion, the initiation and propagation of pores due to the lack of feeding in the last stage of solidification and the localisation of viscoplastic deformation was regarded as a potential trigger for hot tearing. Hot tearing will not occur if (1) the liquid pressure P_l is sufficiently high

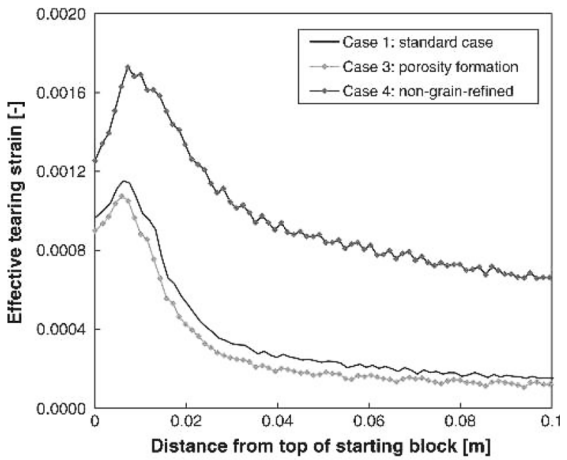

Fig. 5.8. Effective tearing strain for ($w_v = 1$, $w_{d=0}$) when viscoplastic deformation is taken into account (Case 1), when pressure relaxation due to microporosity is taken into account (Case 3), and when a non-grain-refined microstructure is considered (Case 4) [150].

for feeding the thermal-contraction-induced deformation, or (2) the liquid pressure P_l is below the critical value P_c and the pores form but do not reach the critical size, or (3) the pore forms at a very high solid fraction g_s^{nof} where the coalescence and bridging between the grains occur such that the material exhibits sufficient ductility to prevent the formation of a hot tear. The effective tearing strain ($\Delta\varepsilon$) between the rigidity and coalescence points is regarded as the hot tearing indicator, which is expressed as:

$$\Delta\varepsilon = \begin{cases} 0 & \text{for} P_l \geq P_c \\ \int_{t(P_l=P_c)}^{t(g_s=g_s^{\text{nof}})} (w_v.\text{tr}\left(\dot{\varepsilon}_s^P\right) + w_d.\bar{\dot{\varepsilon}}_s^P)\text{d}t & \text{for} P_l < P_c \end{cases} \tag{5.21}$$

where t is the time; w_v and w_d are the weighting factors; $\dot{\varepsilon}_s^P$ is the effective viscoplastic strain rate; $\text{tr}\left(\dot{\varepsilon}_s^P\right)$ is the volumetric part of the viscoplastic strain rate; and $\bar{\dot{\varepsilon}}_s^P$ is the effective deviatoric viscoplastic strain rate.

If $\Delta\varepsilon > \Delta\varepsilon_c$, hot tears occur. The value of $\Delta\varepsilon_c$ depends on the microstructure, number of pores, i.e., potential hot tearing sites, extent of the dendritic coalescence, distribution of the liquid films, and wetting conditions. For the grain-refined granular microstructures relevant for DC casting, $\Delta\varepsilon_c$ is approximately defined as [150]:

$$\Delta\varepsilon_c = \frac{4\pi n_\rho}{3}\left(\frac{nd_s}{2}\right)^3 \min(\chi, \chi^{-2}) \tag{5.22}$$

$$n \in [1, 10]$$

where n_ρ is the volume density of the pore nucleation sites; d_s is the average grain size; and χ is the shape factor of the pores relevant to the thickness of the liquid film, wetting conditions, and applied deformation. This equation has considered the importance of the pore nucleation sites, grain size, and wetting conditions for the formation of hot tears, which should be refined to further consider the effect of the dendritic coalescence.

The model has been successfully applied to study the formation of hot tears under different DC casting process parameters, including the casting speed and its ramping rate, grain refinement, and kind of starting block [150]. An example of the effect of grain refinement on the predicted effective tearing strain in a DC casting ingot is shown in Fig. 5.8. Compared with that in a non-refined microstructure (Case 4), the effective tearing strain decreased due to grain refinement (Case 1). An interesting consequence from Eq. (5.22) is that a large number of distributed pores nucleation sites can result in a distributed relaxation of the applied deformation and, therefore, delay or even prevent the occurrence of hot tearing, as shown in Fig. 5.8 (Case 3). This is verified by the industrial casting experience that adding hydrogen leads to larger micro porosities and thus has a beneficial effect on decreasing hot tearing susceptibility [150]. For the compositional sensitivity, the model well predicts the "lambda" curve in the Al-Cu system [63]. Recently, the model was applied to predict the effect of the Si contents on the hot tearing susceptibility of DC-cast AA7075 billets. The relevant experimental phenomena have been described in Section 4.1.4. The larger $\Delta\varepsilon$ with increasing Si contents was attributed to the longer solidification interval due to the precipitation of low-melting phases. However, the effect of impurity Si on grain coalescence was not considered. This should be improved by considering the grain coalescence in Eq. (5.22).

5.2.2.3. Kou's criterion. Kou [158] proposed a susceptibility criterion for the cracking in a columnar dendritic structure. Note that this criterion is applicable for casting [158], welding [159,160], and even AM [115] processes. Unlike the entire mushy zone was dealt with in the RDG model [15,161], this model only considers the events occurring at grain boundaries. It is assumed that a tear forms when the tensile deformation separating two neighbouring grains exceeds the sum of the liquid feeding of the grain boundary area and the growth of two grains towards each other. Since the hot tearing occurs near the end of solidification ($\sqrt{f_s} \to 1$), based on the analysis of the space between two neighbouring columnar dendritic grains in a volume element near $\sqrt{f_s} = 1$, the following hot tearing criterion is derived:

$$\left\{ \underbrace{\frac{d\varepsilon_{local}}{dT}}_{\text{(separation)}} > \underbrace{\sqrt{1-\beta}\ \frac{d\sqrt{f_s}}{dT}}_{\text{(growth)}} + \underbrace{\frac{1}{dT/dt}\frac{d}{dz}\left[\left(1-\sqrt{1-\beta}\sqrt{f_s}\right)v_z\right]}_{\text{(feeding)}} \right\}_{\sqrt{f_s}\to 1} \tag{5.23}$$

where ε_{local} is the local strain; T is the temperature; f_s is the volume solid fraction; dT/dt is the cooling rate; z is the growth direction of the columnar dendritic grain; and v_z is the velocity of the intergranular liquid flow in the negative z-direction. The three terms in this equation are positive and related to the strain rate, growth rate and feeding rate. The steepness $\left|dT/d(f_s^{1/2})\right|$ near $(f_s)^{1/2} = 1$ is proposed as an index for the hot tearing susceptibility.

The reasons $\left|dT/d(f_s^{1/2})\right|$ near $(f_s)^{1/2} = 1$ can be regarded as the susceptibility index are as follows. First, the higher $\left|dT/d(f_s^{1/2})\right|$ is, the slower the lateral growth rate becomes, i.e. the slower the two neighbouring grains grow towards each other to bond together and resist hot tearing. Second, under a slow lateral growth rate, the columnar grains can grow very long without bridging. This means that the intergranular liquid channel can be very long and hence making it difficult for the fluid to flow through to feed the shrinkage and resist cracking. Third, a long intergranular liquid channel may act as a long sharp notch to promote crack initiation.

Initially, to calculate the index, a short interval of $f_s^{1/2}$ near $(f_s)^{1/2} = 1$ can be taken as $\Delta(f_s)^{1/2}$ and the corresponding temperature

interval can be taken as ΔT to calculate the $\left|\Delta T/\Delta(f_s^{1/2})\right|$ near $(f_s)^{1/2}=1$ [158]. There is no theoretical basis on how to choose the interval of $f_s^{1/2}$ for each alloy. Alternatively, the maximum steepness $\left|dT/d(f_s^{1/2})\right|_{peak}$ near $(f_s)^{1/2}=1$ was used and its validity was verified by its successful application to binary, ternary, and commercial wrought Al alloys [159,162–164] and some magnesium alloys [165].

This criterion was initially proposed for the columnar dendritic structure, and it could be extended to the equiaxed grain structure in the future. Considering the simple form of the hot tearing susceptibility index, this criterion is promising to be widely adopted to different alloys and manufacturing processes.

5.2.2.4. 3D coupled hydromechanical granular model. Over the past few years, many studies have been carried out with the aim to couple granular mechanics with the thermomechanical behaviour of the solidifying alloys [148,149,152,166–168]. Compared to the macro-scale average methods [69,144,150], the granular approach can simulate the interactions between the liquid and solid phases at the microstructure scale while at the same time taking into account the long-range stresses and strains. This model consists of four separate modules [149]: (1) a solidification module used to calculate the liquid-solid geometry at a given solid fraction; (2) a fluid-flow module used to calculate the liquid pressure drop; (3) a semi-solid deformation module that simulates the rheological behaviour of the granular structure; and (4) a failure module that simulates the crack initiation and propagation.

In principle, a hot tear initiates in a liquid channel connected to the atmosphere once the liquid pressure P_l reaches a critical pressure P_l^c. The liquid pressure in the semi-solid medium is computed by the following equation:

$$\frac{2h^3}{3\mu}\nabla^2 P_l = 2\beta v^* + \Delta v_{sn} + \frac{2h}{k_l}\frac{\partial P_l}{\partial t} \tag{5.24}$$

where h is the half-width of the liquid channel; v^* is the solidification speed of the solid-liquid interface; v_{sn} is the normal velocity difference of the solid grains; and k_l is the bulk modulus of the liquid. Moreover, the critical pressure P_l^c is given by:

$$P_l^c = P_a - \frac{\lambda\cos\theta}{h} \tag{5.25}$$

where P_a is the atmospheric pressure; λ is the surface tension at the void-liquid interface; and θ is the dihedral angle. This model was successfully applied to predict the hot tearing observed using the X-ray micro tomography technique, as shown in Fig. 5.9 [167]. The small figure shows the three calculated curves as a function of the tensile displacement: the stress-strain, intergranular liquid pressure P_l (downward curve), and capillary pressure P_l^c associated with the air-liquid interface (air-oxide skin) in the widest liquid channel connected to the exterior (upward curve). When the two curves corresponding to P_l and P_l^c intersect, the first void initiates at the

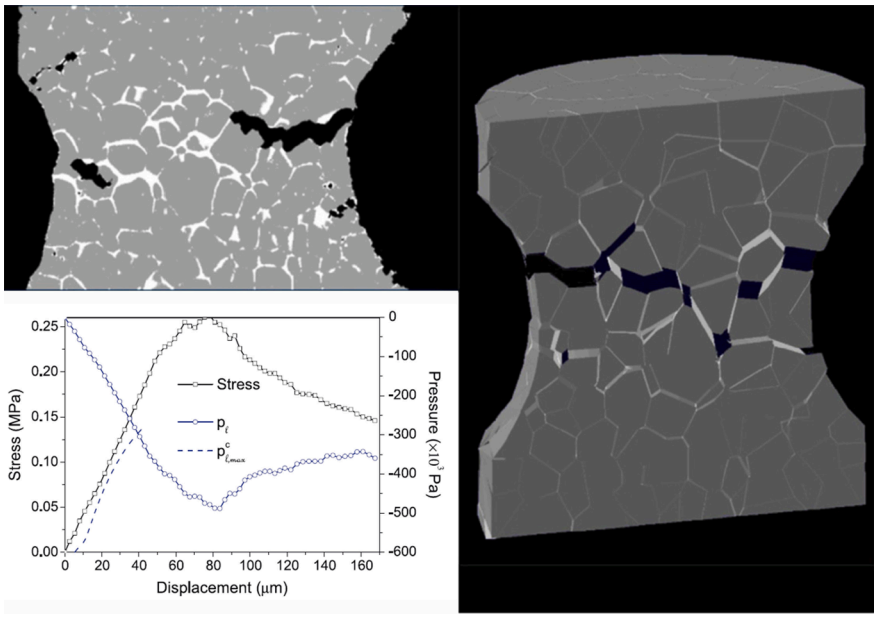

Fig. 5.9. In situ X-ray micro tomography imaging the microstructure of an Al-8 wt% Cu cylindrical specimen under semi-solid tensile test (top left); corresponding microstructure simulation using the 3D granular model (light); predicted stress-strain curve, liquid pressure (P_l) and critical pressure ($P_{l,max}^c$) developments at $f_s = 0.91$ (bottom left) [167]. Note that the white parts represent the intergranular liquid, the dark parts the voids and the grey parts the solid phase.

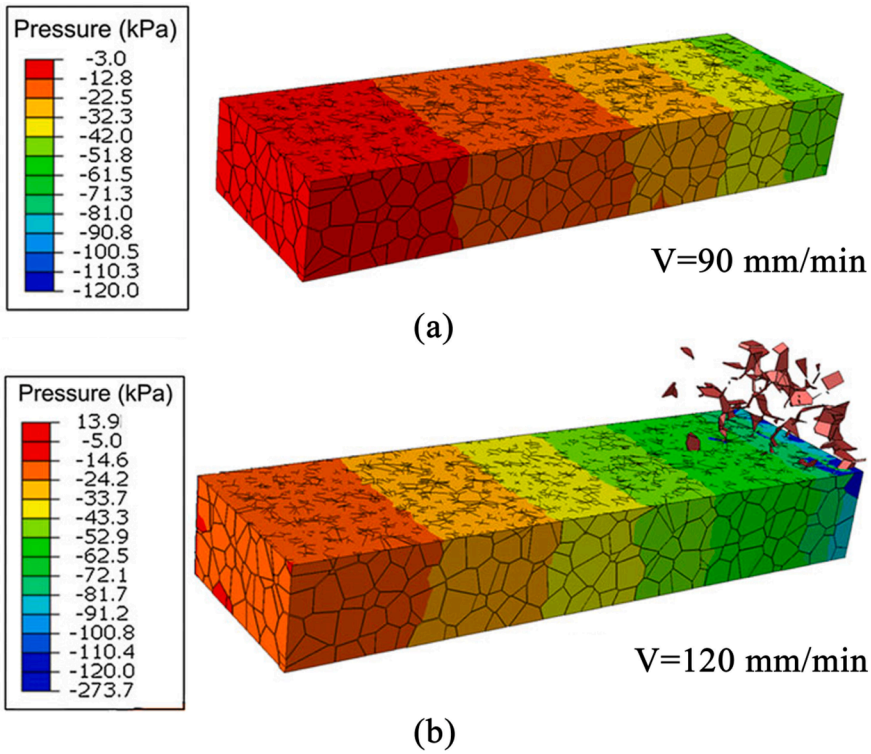

Fig. 5.10. 3D granular model predictions of the liquid pressure in a representative volume located at the centre of a round billet at two casting speeds [170].

surface of the specimen in the widest channel and then propagates inside. Different from the above macro-scale average methods, this model can predict the sites of hot tearing initiation and propagation at a finer scale.

The granular model can provide the inputs for hot tearing criteria at the microstructure scale, along with the spatial variations in these parameters [169]. This allows the formation of hot tearing in grain boundaries by considering both the stochastic variations in grain morphology and the process parameters in DC casting [166,170]. As shown in Fig. 5.10, at a low casting speed, only the individual pores form in the widest channels because the liquid feeding is efficient. As the casting speed increases, the flow of liquid required to compensate for the solidification shrinkage increases and as a result, the pores initiate, propagate and coalesce to form a centreline crack. The criterion can accurately predict whether centreline hot tears will be generated by adjusting only one parameter, $\lambda\cos\theta$.

Zareie and Phillion extended this granular approach to the welding of Al-Mg-Si alloys[169]. The modified model involves (1) a welding solidification module which simulates both the columnar and equiaxed microstructures as a function of the welding parameters; (2) a fluid-flow module to calculate the variation in the pressure within the liquid channels; (3) semi-solid deformation module that predicts the solidification contraction in welding; and (4) Kou's criterion to predict the crack initiation. This approach well links the welding process parameters, external restraints, and hot tearing susceptibility. Because the AM exhibits certain similar characteristics to those of welding [124], in the future, this granular approach can be extended to the AM process to predict the

Table 6
Sensitivity of hot tearing criteria to process parameters and practice during DC casting [144,145].

Criterion	Hot tearing increases with casting speed	More hot tears in the billet centre	Ramping casting speed during start-up of the casting reduces hot tearing	Correlation with actual cracking observed in practice
Clyne and Davies	No	No	No	N/A
Katgerman	Yes	Yes	No	N/A
Feurer	Yes	Yes	No	N/A
Novikov	No	No	No	N/A
Magnin et al.	Yes	No	No	No
Prokhorov	Yes	Yes	No	No
Rappaz et al.	Yes	Yes	Yes	No
Braccini et al.	Yes	Yes	No	N/A
Suyitno et al.	Yes	Yes	Yes	Yes

occurrence of hot tears.

5.3. Comparison of hot tearing criteria

The shape casting and DC casting impose their specific requirements on the hot tearing criteria. A reasonable criterion for DC casting should respond well to the alloy compositions and process parameters and predict the vulnerable locations in a casting. Most of the existing criteria have been tested for the compositional sensitivity by predicting the so-called "lambda" curve in several binary and ternary alloys and their predictions are often successful (Table 5). Apart from some scattered reports on the process parameters sensitivity of the above-mentioned hot tearing criteria, Suyitno et al. [144,145] systematically evaluated the process parameter sensitivity of several commonly used hot tearing criteria by implementing them in a thermomechanical model of DC casting. The results are presented in Table 6.

The criteria of Clyne and Davies and Novikov give results that are inconsistent with the casting practice and do not exhibit any sensitivity to the casting speed and position within the billet volume. These criteria work well in predicting the compositional dependence of hot tearing and are often applied to shape casting (Table 5). The criteria proposed by Katgerman, Feurer, Magnin et al., Braccini et al., Suyitno et al., Rappaz et al., and Prokhorov are sensitive to the casting parameters, showing that the rise in the casting speed leads to higher susceptibility to hot tearing in the centre of the round billet, which matches well with the casting practice (Section 4.2.2). But most of these criteria do not consider the effect of the ramping of casting speed during the starting stage except for the criteria proposed by Rappaz et al. and Suyitno et al.. The criteria developed by Prokhorov, Rappaz et al., and Magnin et al. predict the occurrence of hot tearing whereas no tears have been observed in billets. Only the criterion proposed by Suyitno et al. responds correctly to all the tested parameters. Bai et al. [111] further enhanced the SKK criterion by considering the effect of the solid bridging/grain coalescence, and the improved SKK criterion predicts better with the DC casting practice, especially close to the solidus (Fig. 5.7 (c)). The sensitivities of the two SKK criteria are dependent on the correct values of properties such as Young's modulus of the mushy zone, the surface tension between the solid and liquid phases, fraction of grain boundaries covered by the liquid, and solid energy term (U_s) [7,77,111,144]. These parameters must be accurately measured in the future.

The two-phase model predicts well on the effect of both the compositions and casting parameters during DC casting, as mentioned in Section 5.2.2.2. However, unlike the SKK criterion, the two-phase model does not distinguish between the pore formation and crack initiation. The voids are regarded as the crack nucleus, although the pores should not necessarily develop into hot tears. Another important microscopic factor, the grain coalescence, needs to be integrated into Eq. (5.22).

Different from the two-phase model based on the macro-scale average methods, the granular model highlights the hot tearing mechanism at a more microscopic scale. In the future, the granular model can be combined with the two-phase model or SKK criterion [171]. First, the two-phase model or SKK criterion can be applied to determine the critical regions where hot tears could mostly occur.

Table 7
Summary of hot tearing mechanisms and conditions based on Ref. [23].

Mechanisms and conditions	Suggested and developed by*
Cause of hot tearing	
Solidification shrinkage and thermal contraction	Heine (1935), Pellini (1952), Dobatkin (1948)
Liquid film distribution	Verö (1936)
Liquid pressure drop	Prokhorov (1962), Niyama (1977)
Vacancy supersaturation	Fredriksson et al. (2005)
Nucleation	
Liquid film or pore as a stress concentrator	Patterson et al. (1953, 1967); Niyama (1977); Rappaz et al. (1999); Braccini et al. (2000); Suyitno et al. (2009)
Oxide bi-film or intermetallic particle	Campbell (1991)
Vacancy clusters at a grain boundary or solid/liquid interface	Fredriksson et al. (2005)
Propagation	
By liquid film sliding	Patterson (1953); Williams and Singer; Novikov and Novik (1963)
By liquid film rupture	Pellini (1952); Patterson (1953); Saveiko (1961); Dickhaus (1994); Suyitno et al. (2009)
By liquid metal embrittlement	Novikov (1966); Sigworth (1996)
By liquid film or solid bridge depending on the temperature range	Guven and Hunt (1988); Bai et al. (2016)
Diffusion of vacancies from the solid to the crack	Fredriksson et al. (2005)
Conditions	
Thermal stress exceeds the rupture stress of the liquid film	Saveiko (1961)
Thermal stress exceed rupture or local critical stress	Lees (1946); Langlais and Gruzleski, (2000); Lahaie and Bauchard (2001); Suyitno et al. (2009)
Thermal strain cannot be accommodated by liquid flow and mush ductility	Pellini (1952); Prokhorov (1962); Novikov (1966); Magnin et al. (1996)
Strain rate reaches a critical value that cannot be compensated by liquid feeding and much ductility	Pellini (1952); Prokhorov (1962); Rappaz et al. (1999); Braccini et al. (2000); Kou (2015)
Stresses and insufficient feeding in the vulnerable temperature range	Bochvar (1942); Lees (1946); Pumphrey and Lyons (1948); Clyne and Davies (1975); Feurer (1977); Katgerman (1982)
Pressure drop over the mush reaches a critical value for cavity nucleation	Niyama (1977); Guven and Hunt (1988); Rappaz et al. (1999); Farup and Mo (2000); M'Hamdi et al. (2006); Sistaninia (2012)

* The list of the authors is by no means complete.

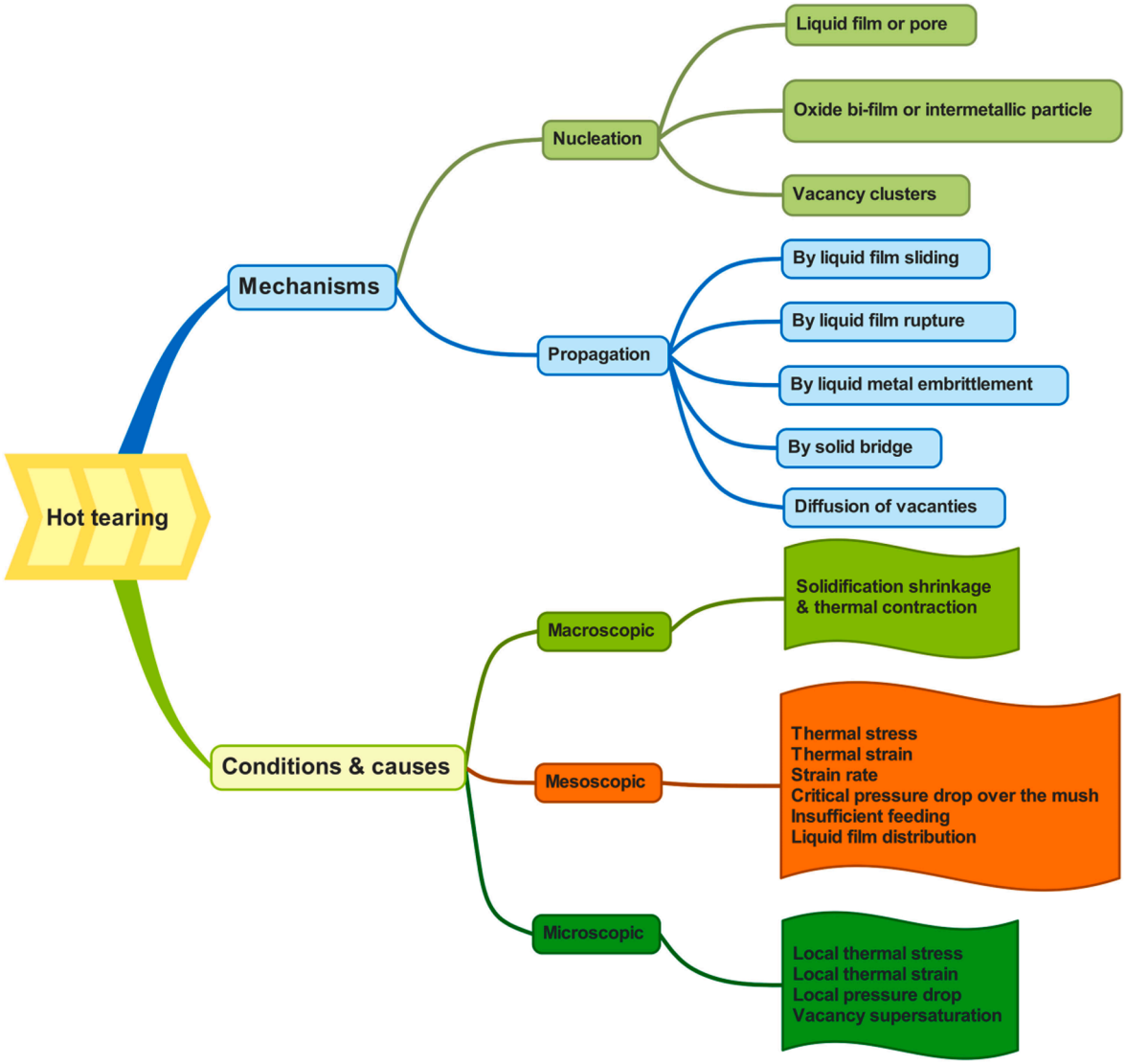

Fig. 5.11. Mechanisms and conditions of hot tearing based on Ref. [23].

Then, the granular model can make a finer microscopic simulation in such critical zones at the grain scale. In fact, similar approaches have been applied to study the crack propagation in solids [172–174].

5.4. Mechanisms of hot tearing

To develop a more powerful hot tearing criterion for casting, a comprehensive summary of the mechanisms of hot tearing is necessary. Great efforts have been made to investigate the mechanisms of hot tearing. Several mechanisms of hot tearing and some conditions for hot tears to occur are summarised in Table 7 and Fig. 5.11. It can be seen that the mechanisms of hot tearing, including the nucleation and propagation of hot tears, have received only limited attention, and most of the research efforts have been devoted to surveying the conditions required to trigger hot tearing. These conditions are considered from different scales, including macroscopic, mesoscopic, and microscopic aspects (Fig. 5.11).

Initially, the macroscopic thermal contraction and mesoscopic/microscopic parameters ((local) stress/strain) were considered as the critical factors for the occurrence of hot tearing. Afterwards, the mesoscopic parameter (strain rate) was regarded as an important factor for the occurrence of hot tearing. It was thought that the liquid films need to take a certain time to accommodate the strains from the solidification shrinkage and thermal contraction. There exists a critical strain rate above which a hot tear can occur. Another important mesoscopic parameter is liquid feeding. The criteria of Feurer, Clyne and Davies, and Katgerman were based on the consideration that hot tearing does not occur under sufficient feeding during solidification. Finally, the (local) pressure drop over the mushy zone was considered as a critical mesoscopic/microscopic parameter for the occurrence of hot tearing in the RDG, two-phase,

and 3D coupled hydromechanical granular models. Note that the pressure drop originates from the solidification shrinkage and thermal contraction.

Many previous hot tearing criteria were based on the conditions that may cause hot tearing and ignore the mechanisms of hot tear nucleation and propagation. An improved hot tear criterion should include fracture mechanics to describe the nucleation and propagation of hot tears, as listed in Table 7 and shown in Fig. 5.11. Suyitno et al. [144] proposed the SKK criterion based on this methodology to simultaneously predict the occurrence of micro-pores and hot tears, as shown in Fig. 5.7(a). This model considers the insufficient feeding as a starting point of the cavity nucleation. Whether the growing cavity becomes a micro-pore or hot tear is determined by the modified Griffith fracture criterion. Bai et al. [111] went further to consider the propagation of hot tears through solid bridges by introducing two parameters (f_{LGB} and U_s), which is an important step to embrace the multi-phase fracture mechanisms.

In a quest for a new hot tearing criterion, Eskin and Katgerman [23] considered different nucleation and propagation mechanisms of the hot cracks at different temperature or solid fraction ranges, as listed in Table 8. The crack initiator could be represented by pore, liquid pool or film, interface with an intermetallic particle, or non-metallic inclusion. At relatively low solid fractions below the coherency point, no tensile stresses have formed, and the permeability of the mushy zone enables the liquid to feed the solidification shrinkage. Most of the precipitating gas can float to the liquid phase of samples. After the coherency point is reached, the tensile stresses caused by the non-uniform thermal contraction of the coherent dendrites may induce the formation of cavities and gaps that are immediately filled with liquid, or "healed". Upon a further decrease in the temperature, the tensile stress accumulates to such an extent that the liquid film separating the grains ruptures, and the gap cannot be filled with the liquid due to the increasing capillary pressures required to fill the increasingly narrowing openings between the grains. When the material is further cooled to the rigidity point, the former entanglement and contact of the grains are replaced by the grain bridging phenomenon. Moreover, the stress can be transmitted over larger distances through the rigid solid skeleton; hence, the semi-solid body acquires macroscopic strength. Moreover, the decreased permeability of the mushy zone in combination with the thermal shrinkage leads to a local pressure drop over the semi-solid region, which, in combination with the evolving gas, promotes the formation of the voids on grain boundaries and the interfaces with the inclusions. The non-uniform thermal stress causes significant strains in the semi-solid body that may not be sustained by the solid bridges. Moreover, the limited liquid flow to the solid bridge may lead to its brittle fracture by the mechanism of the liquid-metal embrittlement. It is possible that the semi-solid body fails macroscopically in a brittle manner (because of the film rupturing and liquid-metal embrittlement) with a ductile rupture of certain solid bridges at the microscopic level [7]. Finally, the bridged grain boundaries become excessively large, and the remaining liquid phases scatter at the grain boundary triple junctions. The semi-solid materials behave completely as solid materials and fail in a ductile manner owing to pore coalescence and high-temperature creep.

6. Future prospects

6.1. Development of hot tearing criteria

An ideal hot tearing criterion should be able to predict not only the probability but also the nucleation and propagation of hot tearing. Despite many hot tearing mechanisms listed in Table 8, the lack of knowledge on nucleation and propagation mechanisms is still a big challenge to the development of the ideal hot tearing criterion. To reveal the nature of hot tearing, several suggestions are provided herein. First, in addition to the SKK criterion to calculate the critical pore size, it is important to further study the critical dimensions of the defects or structural characteristics that can cause the nucleation of hot tears, like oxide bi-films or intermetallic particles. Second, it should be acknowledged that the mechanisms of the hot tearing propagation are dependent on the solid fractions. Different models or variable parameters should be established or adopted depending on the grain structure, composition, and level of stresses/strains. For example, for a coarse grain structure with a high coherency temperature, hot tears can occur early due to the rupture of the liquid films. When considerable amounts of eutectics exist, e.g., in the Al-Si alloys, the hot tears may be healed. For a fine

Table 8
Possible mechanisms acting in the hot tearing phenomenon [23].

Temperature range/solid fraction	Nucleation of crack	Propagation of crack	Fracture mode
Between coherency and rigidity temperatures; 50–80% solid	Grain boundary covered with liquid, shrinkage or gas pore	a. Liquid film rupture b. Filled gap	a. Brittle, intergranular b. Healed crack
Below rigidity temperature; 80–99% solid	Pore, surface of particle or inclusion, liquid film or pool, vacancy clusters	a. Liquid film rupture; liquid metal embrittlement of solid bridges b. Plastic deformation of bridges	a. Brittle, intergranular b. Ductile failure of bridges possible
Close to the solidus; 98–100% solid	Pore, surface of particle or inclusion, segregates at grain boundary, liquid at stress concentration point, vacancy clusters	a. Liquid metal embrittlement of solid ridges b. Plastic deformation of bridges, creep	a. Brittle, intergranular, transgranular propagation is possible b. Macroscopically brittle or ductile, intergranular; transgranular propagation is possible

equiaxed structure with a low coherency temperature and a small amount of eutectics, e.g., some commercial wrought alloys, several fracture mechanics may co-exist, including liquid-metal embrittlement and plastic deformation of solid bridges with a mixed brittle/ductile fracture. Third, the multi-stage mechanism of the hot tearing propagation should be simulated to predict the crack propagation based on the granular approach (Section 5.2.2.4) or phase field simulations. The size and morphology of the grains, distributions of eutectic liquid, grain bridging, and stochastic effects should be considered. A combination of the hot tearing simulations and machine learning algorithms can be used to predict the hot tearing patterns, which has been achieved in solid-state fracture phenomena recently [175].

6.2. *Measurement prospects*

As indicated at the end of Section 2, a standard testing framework to characterise the hot tearing behaviour under DC casting conditions is needed, including the hot tearing susceptibility, thermomechanical behaviour of semi-solid materials, and initiation and propagation of hot tears. It does not imply that one apparatus is omnipotent to simulate different DC casting conditions and can evaluate all the influencing factors. Several standard testing apparatus or functional components should be established corresponding to DC casting practice. Thus, the experimental data from different researchers can be compared when included in a hot tearing database of different aluminium alloys. An outline of this testing framework is given in Fig. 6.1, which is expected to possess the following features and functions:

Fig. 6.1. An outline of the standard hot tearing testing framework for DC casting.

- Ability to simulate the DC casting conditions. It can accurately evaluate and differentiate the hot tearing susceptibility of alloys with different alloying compositions. The effect of different process parameters on hot tearing susceptibility should be evaluated. The authors propose to further improve the CHT rig (Fig. 2.7) into the main testing unit based on other testing devices (Section 2.2.1), which is attributed to its existing advantages (Fig. 2.5).
- Advanced visualisation technology to be applied to the testing apparatus to in situ characterise the nucleation and propagation of hot tears in 3D space during continuous cooling instead of testing them under isothermal conditions [86]. This can accurately reveal the intrinsic mechanisms of hot tearing. This technology can be applied to in situ measure the defect characteristics and hot tears including surface and interior defects, which can yield an accurate hot tearing rating. The 3D synchrotron X-ray micro tomography technique (Section 2.2.2) is a promising candidate but still need to be improved to overcome the current drawbacks pertaining to the characterisation of hot tears (Fig. 2.10).
- Ability to in situ capture the load development, thermal contraction behaviour, and stress/strain distribution during solidification. These data can be compared with the hot tearing susceptibility and can be used as an input for the hot tearing criteria. This part is easier to be achieved with reference to the existing design concepts (Section 2.2.1).
- The framework must be able to realise semi-solid isothermal tensile testing upon solidification, which can mimic the real mushy zone microstructure evolution during DC casting and determine the semi-solid mechanical properties reliably. The modified Instron mechanical testing machine (Fig. 2.2) combined with the reheating-cooling method is a promising choice, as mentioned in Section 2.1.2.
- Include different functional components, which can be easily assembled to meet different demands.

It is necessary to verify the influence trends of the alloying elements and process parameters from the ideal testing framework by using a trial DC casting machine and subsequent industrial DC casting practices.

6.3. *Modelling prospects*

Over the years, large amounts of data from different experimental setups and modelling tools have been obtained under different compositions and process parameters, including the as-cast structures, mushy zone mechanical properties, and hot tearing susceptibility. To further understand the mechanisms governing the associated relationships, a comprehensive database needs to be built and analysed by machine learning. Ultimately, such work will enable the efficient casting of aluminium alloys with a high susceptibility to hot tearing and the design of new aluminium alloys considering the hot tearing susceptibility. The database should consist of four parts. An overview of the database is shown in Fig. 6.2. The details are as follows.

1) Composition and processing dataset. It contains different alloying elements and various process parameters. The alloying elements include the major elements, minor elements, and grain refiners. The processing parameters are complex and contain various influencing factors, as shown in Fig. 6.2.
2) Property dataset. It mainly contains the information related to the thermal contraction behaviour, load behaviour upon solidification, semi-solid mechanical properties, distributions of multi-physical fields in castings, and mushy-zone permeability of different alloys. As summarised in Section 3, many relevant data are available and can be collected. One needs to distinguish their sources and measurement setups when employing these data. Great efforts need to be further made to step-wise feed this dataset

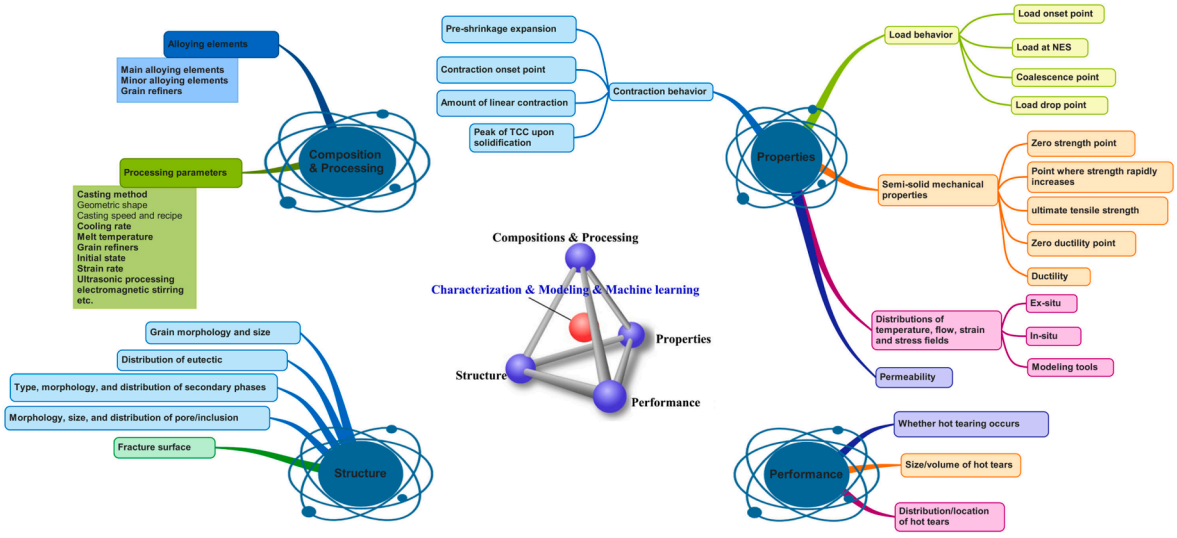

Fig. 6.2. An outline of the hot tearing database. It contains four databases: composition & Processing dataset, properties dataset, structure dataset, and performance dataset.

using the proposed standard testing method in Section 6.2. For the distributions of the multi-physical fields (temperature, flow, strain, stress fields) in castings, some existing experimental methods can ex situ measure them [93,94,176]. Modelling of these multi-physical fields can be done by finite element methods combined with the semi-solid constitutive equations [19,21]. Note that the mesoscopic strain and stress phenomena in castings during solidification are reflected by their macroscopic contraction and load behaviour.

3) Structure dataset. It includes the grain characteristics, distribution of the eutectics, features of the secondary phases, pore/inclusion characteristics, and fracture surfaces.
4) Performance dataset. It includes whether hot tearing occurs or not, the size/volume, and distribution/location of the hot tears.

At present, experimental methods are the main approach to obtain relevant data, some of which are used as an input to modelling tools to predict the distribution of the temperature, flow, stress, and strain fields as well as the sizes of pores and hot tears. It is recommended to analyse these existing large amounts of data using machine learning and feed the database with the help of the proposed standard testing framework and simulation. Several important aspects are worthy of noting. First, the database should include experimental and simulation data from different sources, e.g., alloy systems and processing data from different DC casting process parameters, structure and mechanical properties data, and image data from OM, SEM, TEM, X-ray tomography techniques and other sources. It is required to develop a fundamental concept of the database considering the very different data sources and identifying their common features. Due to the inconsistency of data in such a big database, data cleansing must be performed to pre-process the database by using intelligent machine learning classification/clustering algorithms. Moreover, it is indeed that some data are difficult to be measured (like semi-solid ductility) or simulated (like stress/strain). Some cutting-edge deep learning algorithms could be helpful to solve these questions and push the field to a new level. For example, it can be thought that the semi-solid strength could be closely related to its semi-solid ductility. Thus, a regression prediction model obtained from the semi-solid strength could be "grafted" to describe the semi-solid ductility via a transfer learning neural network [177,178] and a small amount of ductility data. Another example is to predict the stress, strain, and fluid-flow fields only based on the easily predicted temperature field in DC-cast ingots. A deep-learning framework combined with some existing physics-based constitutive or fluid-flow equations could handle this challenge [179]. Finally, the complex relationships in the big database should be analysed using machine learning. The machine-learning-derived correlations can be transformed into formulations and compared with the existing physics-based hot tearing models to verify the consistency. If a good correlation could be obtained, one could further apply machine learning to explore new hot tearing

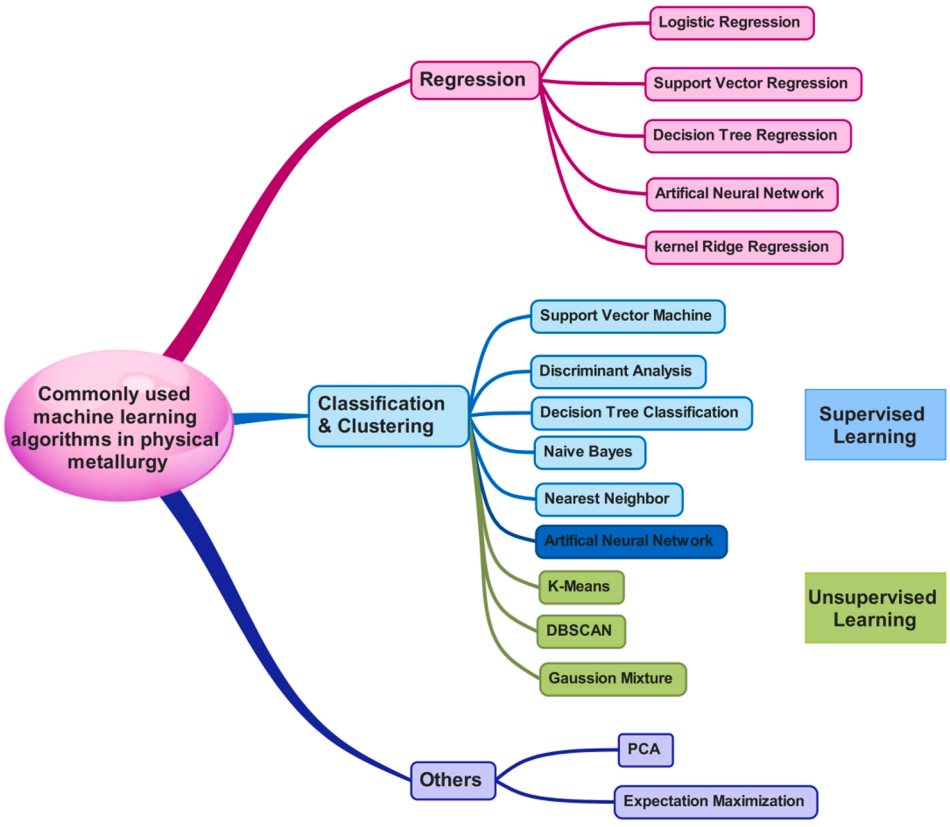

Fig. 6.3. Probably used machine learning algorithms in physical metallurgy. Note that the artificial neural network belongs to both supervised and unsupervised learnings depending on whether the labelled data are provided or not.

models.

Here, some commonly used machine learning algorithms in physical metallurgy are shown in Fig. 6.3. They can be classified as regression, classification/clustering, and other data-processing algorithms. For example, the classification/clustering algorithms can be used for data purification [156,180–182], whereas the regression algorithms [183–186] can be used for building the relationships among compositions/processing parameters, as-cast microstructures, semi-solid mechanical properties, and hot tearing susceptibility. Note that no single algorithm is appropriate for all situations, and selecting a suitable algorithm is essential to achieve a high prediction accuracy [187,188].

The thermomechanical simulation in a large-scale DC casting billet is computationally intensive. Often it takes considerable time to perform a calculation, which restricts a quick hot tearing prediction. To accelerate this timeframe, high-throughput computational approaches should be designed, which includes the integration with multi-scale simulation software, hot tearing big data, parallel computing techniques, machine learning, and computer hardware.

The current hot tearing prediction software for DC casting is rarely coupled with an as-cast microstructure simulation software. The microstructural features in a large-scale DC casting billet, like the distribution of the grain size and morphology, precipitation sequence, size, and morphology of the secondary phases, as well as macrosegregation phenomena are not included. Multi-scale simulation software is required to accurately predict the hot tearing susceptibilities. For example, the macro-scale average methods should be coupled with the micro-scale granular model to make accurate hot tearing predictions.

Finally, consistent modelling requires accurate thermophysical data. To date, only limited data are fairly well known, like latent heat of fusion, but many important parameters need to be accurately measured, especially the parameters related to the solid/liquid and solid/solid interfaces. Their temperature dependences are often ignored but could have a big influence on the final predictions under certain conditions.

7. Concluding remarks

In this review, research after 2004 on the hot tearing characterisation methods, semi-solid behaviour and properties, compositions and process conditions affecting hot tearing, and the developments in hot tearing criteria are evaluated.

With the progress of material characterisation techniques and the comprehensive understanding of the hot tearing phenomena, a series of hot tearing measurement devices and techniques were developed, focusing on rating the hot tearing susceptibility, observing the developments of micro-pores and hot tears, and measuring the semi-solid properties of aluminium alloys. After a critical evaluation, a set of standard hot tearing testing frameworks with various functional components is suggested to physically simulate DC casting. This will standardize data generation, collection, and comparison.

The semi-solid properties of materials are not only composition-dependent but also process parameter dependent. In addition to the semi-solid mechanical properties, the development of real-time macroscopic load/contraction or mesoscopic stress/strain measurements were evaluated. These properties are often regarded as important parameters for constructing constitutive equations and predicting hot tearing susceptibilities. These valuable property data should be collated into a database to be further analysed and exploited with the help of machine learning.

The correlations among the composition, processing parameters, as-cast microstructures, and hot tearing susceptibilities are summarised for both shape casting and DC casting. The differences in the same materials for different casting methods are highlighted.

The progress in the fundamental understanding of hot tearing will enable new hot tearing criteria to be formulated for quantitative predictions, which will be a milestone in the field of hot tearing research. With the development of a comprehensive hot tearing database and the help of state-of-the-art materials informatics, an omnipotent hot tearing criterion is promising to be obtained in the future.

Declaration of Competing Interest

The authors declare that they have no known competing financial interests or personal relationships that could have appeared to influence the work reported in this paper.

Acknowledgements

The Major State Research and Development Program of China (Grant No. 2016YFB0300801), the National Natural Science Foundation of China (51671017, 51971020), Beijing Laboratory of Metallic Materials and Processing for Modern Transportation, Beijing Municipal Natural Science Foundation (2202033), the Fundamental Research Funds for the Central Universities (No. FRF-IC-19-010, FRF-IC-19-015) are deeply appreciated for their financial support. Yue Li was supported by the China Scholarship Council and Research Council of Norway as a joint training Ph. D student in SINTEF/NTNU, Norway. The members Prof. M. X. Guo, Prof. D. Zhang, Prof. H. Cui, Dr. L.G. Hou, Dr. J.C. Liu, Dr. Q.L. Bai, Mr. Z. R. Zhang, Z. Y. Zhao, Z.L. Zhu, Y.B. Wang, B.Y. Liu, Mrs. Y. Kong from USTB are also appreciated for their supports of this paper.

References

[1] Olakanmi EO, Cochrane RF, Dalgarno KW. A review on selective laser sintering/melting (SLS/SLM) of aluminium alloy powders: processing, microstructure, and properties. Prog Mater Sci 2015;74:401–77.

[2] Lumley R. Fundamentals of aluminium metallurgy: recent advances. Woodhead Publishing; 2018.
[3] Liu G, Müller DB. Addressing sustainability in the aluminum industry: a critical review of life cycle assessments. J Clean Prod 2012;35:108–17.
[4] Mineral Commodity Summaries: Government Printing Office; 2000-2019.
[5] Mondolfo LF. Aluminum alloys: structure and properties. London, Sydney, Toronto, Welington, Durban, Boston: Elsevier; 2013.
[6] Vasudevan AK, Doherty RD. Aluminum alloys–contemporary research and applications: contemporary research and applications. Boston, San Diego, New York, Berkeley, London, Sydney, Tokyo, Toronto: Elsevier; 2012.
[7] Eskin DG. Physical metallurgy of direct chill casting of aluminum alloys. Boca Raton, London, New York: CRC Press; 2008.
[8] Sosro Subroto T. Connection between hot tearing and cold cracking in DC-casting of AA7050: Experiments and computer simulations. Netherland: Delft University of Technology; 2014.
[9] Aboulkhair NT, Simonelli M, Parry L, Ashcroft I, Tuck C, Hague R. 3D printing of Aluminium alloys: Additive Manufacturing of Aluminium alloys using selective laser melting. Prog Mater Sci 2019;106:100578.
[10] Pauly S, Wang P, Kühn U, Kosiba K. Experimental determination of cooling rates in selectively laser-melted eutectic Al-33Cu. Addit Manuf 2018;22:753–7.
[11] Opprecht M, Garandet J-P, Roux G, Flament C, Soulier M. A solution to the hot cracking problem for aluminium alloys manufactured by laser beam melting. Acta Mater 2020;197:40–53.
[12] Stopyra W, Gruber K, Smolina I, Kurzynowski T, Kuźnicka B. Laser powder bed fusion of AA7075 alloy: influence of process parameters on porosity and hot cracking. Addit Manuf 2020;35:101270.
[13] Zhou SY, Su Y, Wang H, Enz J, Ebel T, Yan M. Additive Manufacturingadditive manufacturing of 7xxx series Al-Zn-Mg-Cu alloy: cracking elimination by co-incorporation of Si and TiB2. Addit Manuf 2020;36:101458.
[14] Eskin DG, Suyitno Mooney JF, Katgerman L. Contraction of aluminum alloys during and after solidification. Metall Mater Trans A 2004;35:1325–35.
[15] Eskin DG, Suyitno Katgerman L. Mechanical properties in the semi-solid state and hot tearing of aluminium alloys. Prog Mater Sci 2004;49:629–711.
[16] Hu XG, Zhu Q, Atkinson HV, Lu HX, Zhang F, Dong HB, et al. A time-dependent power law viscosity model and its application in modelling semi-solid die casting of 319s alloy. Acta Mater 2017;124:410–20.
[17] Atkinson HV. Modelling the semisolid processing of metallic alloys. Prog Mater Sci 2005;50:341–412.
[18] van Haaften W, Kool W, Katgerman L. Tensile behaviour of semi-solid industrial aluminium alloys AA3104 and AA5182. Mater Sci Eng, A 2002;336:1–6.
[19] Phillion A. Hot tearing and constitutive behaviour of semi-solid aluminum alloys. Canada: University of British Columbia; 2007.
[20] Ludwig O, Drezet JM, Ménésès P, Martin CL, Suéry M. Rheological behavior of a commercial AA5182 aluminum alloy during solidification. Mater Sci Eng, A 2005;413–414:174–9.
[21] Ludwig O, Drezet J-M, Martin CL, Suéry M. Rheological behavior of Al-Cu alloys during solidification constitutive modeling, experimental identification, and numerical study. Metall Mater Trans A 2005;36:1525–35.
[22] Phillion ACS, Lee P. Predicting the constitutive behavior of semi-solids via a direct finite element simulation: application to AA5182. Modell Simul Mater Sci Eng 2009;17:055011.
[23] Eskin DG, Katgerman L. A quest for a new hot tearing criterion. Metall Mater Trans A 2007;38:1511–9.
[24] Jarry P, Rappaz M. Recent advances in the metallurgy of aluminium alloys. Part I: Solidification and casting. CR Phys 2018;19:672–87.
[25] Dantzig JA, Rappaz M. Solidification: -Revised & Expanded: EPFL press; 2016.
[26] Li Y, Bai QL, Liu JC, Li HX, Du Q, Zhang JS, et al. The influences of grain size and morphology on the hot tearing susceptibility, contraction, and load behaviors of AA7050 alloy inoculated with Al-5Ti-1B master alloy. Metall Mater Trans A 2016;47:4024–37.
[27] Suyitno Eskin DG, Katgerman L. Structure observations related to hot tearing of Al–Cu billets produced by direct-chill casting. Mater Sci Eng, A 2006;420:1–7.
[28] Du Q, Jacot A. A two-dimensional microsegregation model for the description of microstructure formation during solidification in multicomponent alloys: formulation and behaviour of the model. Acta Mater 2005;53:3479–93.
[29] Sweet L, Easton MA, Taylor JA, Grandfield JF, Davidson CJ, Lu L, et al. Hot tear susceptibility of Al-Mg-Si-Fe alloys with varying iron contents. Metall Mater Trans A 2013;44:5396–407.
[30] Novikov II. Hot-shortness of nonferrous metals and alloys. Moscow: Nauka; 1966.
[31] Li S, Apelian D. Hot tearing of aluminum alloys a critical literature review. Int J Metalcast 2011;5:23–40.
[32] Lin S. Study of hot tearing in wrought Aluminium alloys. Canada: University of Québec in Chicoutimi; 1999.
[33] Lin S, Aliravci C, Pekguleryuz M. Hot-tear susceptibility of aluminum wrought alloys and the effect of grain refining. Metall Mater Trans A 2007;38:1056–68.
[34] Giraud E, Suery M, Coret M. Mechanical behavior of AA6061 aluminum in the semisolid state obtained by partial melting and partial solidification. Metall Mater Trans A 2010;41:2257–68.
[35] Sheykh-jaberi F, Cockcroft SL, Maijer DM, Phillion AB. Comparison of the semi-solid constitutive behaviour of A356 and B206 aluminum foundry alloys. J Mater Process Technol 2019;266:37–45.
[36] Bolouri A, Liu K, Chen X-G. Effects of iron-rich intermetallics and grain structure on semisolid tensile properties of Al-Cu 206 cast alloys near solidus temperature. Metall Mater Trans A 2016;47:6466–80.
[37] Chen G, Jiang J, Du Z, Han F, Atkinson HV. Hot tensile behavior of an extruded Al–Zn–Mg–Cu alloy in the solid and in the semi-solid state. Mater Des 2014;54:1–5.
[38] Subroto T, Miroux A, Eskin DG, Ellingsen K, Marson A, M'Hamdi M, et al. Tensile mechanical behavior of as-cast AA7050 alloy in the super-solidus temperature range. In: 13th International conference on fracture. Beijing; 2013. p. 2528–36.
[39] Phillion AB, Thompson S, Cockcroft SL, Wells MA. Tensile properties of as-cast aluminum alloys AA3104, AA6111 and CA31218 at above solidus temperatures. Mater Sci Eng, A 2008;497:388–94.
[40] Phillion AB, Cockcroft SL, Lee PD. A new methodology for measurement of semi-solid constitutive behavior and its application to examination of as-cast porosity and hot tearing in aluminum alloys. Mater Sci Eng, A 2008;491:237–47.
[41] Fabregue D, Deschamps A, Suery M, Poole WJ. Rheological behavior of Al-Mg-Si-Cu alloys in the mushy state obtained by partial remelting and partial solidification at high cooling rate. Metall Mater Trans A 2006;37A:1459–67.
[42] Colley L, Wells M, Maijer D. Tensile properties of as-cast aluminum alloy AA5182 close to the solidus temperature. Mater Sci Eng, A 2004;386:140–8.
[43] Han Q, Hassan M, Saito K, Viswanathan S, Das S. The reheating-cooling method: a technique for measuring mechanical properties in the nonequilibrium mushy zones of alloys. Metall Mater Trans A 2005;36:2073–80.
[44] Twite MR, Spittle JA, Brown SG. The tensile properties of semi-solid aluminum alloys. Int J Form Processes 2004;7:233–60.
[45] Nagaumi H, Suvanchai P, Okane T, Umeda T. Mechanical properties of high strength Al-Mg-Si alloy during solidification. Mater Trans 2006;47:2918–24.
[46] Pongsugitwat S, Umeda T, Sricharoenchai P. Tensile properties during solidification of aluminium die casting alloys grade ADC5, ADC6 and ADC12. Adv Mater Res 2014;1025:208–14.
[47] Phillion AB, Lee PD, Maire E, Cockcroft SL. Quantitative assessment of deformation-induced damage in a semisolid aluminum alloy via X-ray microtomography. Metall Mater Trans A 2008;39:2459–69.
[48] Pekguleryuz M, Li X, Aliravci C. In-situ investigation of hot tearing in aluminum alloy AA1050 via acoustic emission and cooling curve analysis. Metall Mater Trans A 2009;40:1436–56.
[49] Cao G, Kou S. Hot cracking of binary Mg–Al alloy castings. Mater Sci Eng, A 2006;417:230–8.
[50] Dubey SN. Design and evaluation of an enhanced constrained rod casting mold for experimental characterization of hot tearing in aluminum casting alloys. Int J Cast Met Res 2017:1–16.
[51] Wang Z, Huang Y, Srinivasan A, Liu Z, Beckmann F, Kainer KU, et al. Hot tearing susceptibility of binary Mg–Y alloy castings. Mater Des 2013;47:90–100.
[52] Li S, Sadayappan K, Apelian D. characterization of hot tearing in Al cast alloys: methodology and procedures. Int J Cast Met Res 2011;24:88–95.
[53] Esfahani MRN, Niroumand B. Study of hot tearing of A206 aluminum alloy using Instrumented Constrained T-shaped Casting method. Mater Charact 2010;61:318–24.

[54] Sweet L, Taylor JA, Couper MJ, Easton MA. Hot tearing in Al-Mg-Si alloys with minor additions of Cu or Mn. Mater Sci Forum 2011;693:217–23.
[55] Ellingsen K, Du Q, M'Hamdi M, Gihleengen BE, Ledal R, Tveito KO, et al. Experimental study and numerical analysis of cracking during DC casting of large dimension 7075 aluminium billets. In: TMS annual meeting & exhibition. Cham: Springer; 2018. p. 895–900.
[56] Warrington D, McCartney DG. Development of a new hot-cracking test for aluminum alloys. Cast Metals 1989;2:134–43.
[57] Warrington D, McCartney DG. Hot-cracking in aluminum alloys 7050 and 7010 - a comparative study. Cast Metals 1991;3:202–8.
[58] Drezet J-M, Mireux B, Kurtuldu G, Magdysyuk O, Drakopoulos M. Measurement of mechanical coherency temperature and solid volume fraction in Al-Zn alloys using in situ X-ray diffraction during casting. Metall Mater Trans A 2015;46:4183–90.
[59] Li S, Sadayappan K, Apelian D. Role of grain refinement in the hot tearing of cast Al-Cu alloy. Metall Mater Trans B 2013;44:614–23.
[60] Clyne TW, Davies GJ. A quantitative solidification cracking test for castings and an evaluation of cracking in aluminum-magnesium alloys. British Foundryman 1975;68:238–44.
[61] Drezet J-M, Mireux B, Szaraz Z, Pirling T. In situ neutron diffraction during casting: determination of rigidity point in grain refined al-Cu alloys. Materials 2014;7:1165–72.
[62] Instone S, St John D, Grandfield J. New apparatus for characterising the tensile strength development and hot cracking in the mushy zone. Int J Cast Met Res 2000;12:441–56.
[63] Stangeland A, Mo A, M'Hamdi M, Viano D, Davidson C. Thermal strain in the mushy zone related to hot tearing. Metall Mater Trans A 2006;37:705–14.
[64] Easton MA, Wang H, Grandfield J, Davidson CJ, StJohn DH, Sweet LD, et al. Observation and prediction of the hot tear susceptibility of ternary Al-Si-Mg alloys. Metall Mater Trans A 2012;43:3227–38.
[65] Sweet L, Taylor J, Easton M, Couper M, Parson N. Chemical additions to reduce hot tearing in the cast house. Light Metals 2012: Springer International Publishing; 2012. p. 1133–8.
[66] Easton M, Wang H, Grandfield J, St John D, Sweet E. An analysis of the effect of grain refinement on the hot tearing of aluminium alloys. Mater Forum 2004;28:224–9.
[67] Mitchell J, Cockcroft S, Viano D, Davidson C, StJohn D. Determination of strain during hot tearing by image correlation. Metall Mater Trans A 2007;38:2503–12.
[68] Viano D, StJohn D, Grandfield J, Cáceres C. Hot tearing in aluminium-copper alloys. In: Grandfield JF, Eskin DG, editors. Essential Readings in Light Metals: Volume 3 Cast Shop for Aluminum Production. Cham: Springer International Publishing; 2016. p. 895–9.
[69] Mathier V, Vernede S, Jarry P, Rappaz M. Two-phase modeling of hot tearing in aluminum alloys: applications of a semicoupled method. Metall Mater Trans A 2009;40:943.
[70] Davidson C, Viano D, Lu L, StJohn D. Observation of crack initiation during hot tearing. Int J Cast Met Res 2006;19:59–65.
[71] Zhang L. Ultrasonic processing of aluminum alloys. Netherland: Delft University of Technology; 2013.
[72] Eskin DG, Zuidema J, Katgerman L. Linear solidification contraction of binary and commercial aluminium alloys. Int J Cast Met Res 2002;14:217–23.
[73] Zhang L, Eskin DG, Lalpoor M, Katgerman L. Factors affecting thermal contraction behavior of an AA7050 alloy. Mater Sci Eng, A 2010;527:3264–70.
[74] Stangeland A, Asbjørn M, Nielsen Ø, M'Hamdi M, Eskin DG. Development of thermal strain in the coherent mushy zone during solidification of aluminum alloys. Metall Mater Trans A 2004;35:2903–15.
[75] Stangeland A, Mo A, Eskin DG. Thermal strain in the mushy zone for aluminum alloys. Metall Mater Trans A 2006;37:2219–29.
[76] Bai QL, Li Y, Li HX, Du Q, Zhang JS, Zhuang LZ. Roles of alloy composition and grain refinement on hot tearing susceptibility of 7×××aluminum alloys. Metall Mater Trans A 2016;47:4080–91.
[77] Li Y, Zhang ZR, Zhao ZY, Li HX, Katgerman L, Zhang JS, et al. Effect of main elements (Zn, Mg, and Cu) on hot tearing susceptibility during direct-chill casting of 7xxx aluminum alloys. Metall Mater Trans A 2019;50:3603–16.
[78] Li Y, Gao X, Zhang ZR, Xiao WL, Li HX, Du Q, et al. Experimental and theoretical studies of the hot tearing behavior of Al-xZn-2Mg-2Cu alloys. Metall Mater Trans A 2017;48:4744–54.
[79] Pan Y, Zhang D, Liu H, Zhang Z, Li H, Zhuang L, et al. Reducing welding hot cracking of high-strength novel Al–Mg–Zn–Cu alloys based on the prediction of the T-shaped device. Sci Technol Weld Joining 2020;25:483–9.
[80] Farup I, Drezet J-M, Rappaz M. In situ observation of hot tearing formation in succinonitrile-acetone. Acta Mater 2001;49:1261–9.
[81] Ludwig O, Dimichiel M, Salvo L, Suéry M, Falus P. In-situ three-dimensional microstructural investigation of solidification of an Al-Cu alloy by ultrafast x-ray microtomography. Metall Mater Trans A 2005;36:1515–23.
[82] Phillion AB, Cockcroft SL, Lee PD. X-ray micro-tomographic observations of hot tear damage in an Al–Mg commercial alloy. Scripta Mater 2006;55:489–92.
[83] Terzi S, Salvo L, Suéry M, Limodin N, Adrien J, Maire E, et al. In situ X-ray tomography observation of inhomogeneous deformation in semi-solid aluminium alloys. Scripta Mater 2009;61:449–52.
[84] Suéry M, Terzi S, Mireux B, Salvo L, Adrien J, Maire E. Fast in situ X-Ray microtomography observations of solidification and semisolid deformation of Al-Cu alloys. JOM 2012;64:83–8.
[85] Puncreobutr C, Lee PD, Hamilton RW, Phillion AB. Quantitative 3D characterization of solidification structure and defect evolution in Al alloys. JOM 2012;64:89–95.
[86] Puncreobutr C, Lee PD, Hamilton RW, Cai B, Connolley T. Synchrotron tomographic characterization of damage evolution during aluminum alloy solidification. Metall Mater Trans A 2013;44:5389–95.
[87] Puncreobutr C, Lee PD, Kareh KM, Connolley T, Fife JL, Phillion AB. Influence of Fe-rich intermetallics on solidification defects in Al–Si–Cu alloys. Acta Mater 2014;68:42–51.
[88] Terzi S, Salvo L, Suery M, Dahle A, Boller E. Coarsening mechanisms in a dendritic Al–10% Cu alloy. Acta Mater 2010;58:20–30.
[89] Chiang P-J, Jiang R, Cunningham R, Parab N, Zhao C, Fezzaa K, et al. In situ characterization of hot cracking using dynamic X-ray radiography. Cham: Springer International Publishing; 2019. p. 77–85.
[90] Aucott L, Huang D, Dong H, Wen S, Marsden J, Rack A, et al. Initiation and growth kinetics of solidification cracking during welding of steel. Sci Rep 2017;7:40255.
[91] Maire E, Withers PJ. Quantitative X-ray tomography. Int Mater Rev 2014;59:1–43.
[92] Wu SC, Xiao TQ, Withers PJ. The imaging of failure in structural materials by synchrotron radiation X-ray microtomography. Eng Fract Mech 2017;182:127–56.
[93] Saito Y, Todoroki H, Kobayashi Y, Shiga N, Tanaka S-I. Hot-cracking mechanism in Al–Sn alloys from a viewpoint of measured residual stress distributions. Mater Trans 2018;59:908–16.
[94] D'Elia F, Ravindran C, Sediako D. Quantification of residual strain associated with reduction of hot tears by grain refinement in B206 aluminium alloy. Can Metall Q 2014;53:151–9.
[95] Drezet JM, Evans A, Pirling T, Pitié B. Stored elastic energy in aluminium alloy AA 6063 billets: residual stress measurements and thermomechanical modelling. Int J Cast Met Res 2012;25:110–6.
[96] Drezet JM, Phillion AB. As-cast residual stresses in an aluminum alloy AA6063 billet: neutron diffraction measurements and finite element modeling. Metall Mater Trans A 2010;41:3396–404.
[97] Charunetratsamee S, Poopat B, Jirarungsatean C. Feasibility Study of Acoustic Emission Monitoring of Hot Cracking in GTAW Weld. Key Eng Mater 2013;545:236–40.
[98] Homsawat P, Jirarungsatian C, Phung-On I. Correlation between acoustic emission and induced hydrogen of shield metal arc welding. New York, NY: Springer New York; 2015. p. 643–9.
[99] Strantza M, Aggelis DG, De Baere D, Guillaume P, Van Hemelrijck D. Evaluation of SHM system produced by additive manufacturing via acoustic emission and other NDT methods. Sensors 2015;15:26709–25.

[100] Taheri H, Shoaib MRBM, Koester LW, Bigelow TA, Collins PC, Bond LJ. Powder-based additive manufacturing-a review of types of defects, generation mechanisms, detection, property evaluation and metrology. Int J Additive Subtractive Mater Manuf 2017;1:172–209.
[101] Zhang LH, Yi XX, Hu QQ, Zhu B. Effect mechanism of ultrasonic field on hot tearing forming for semi-casting aluminum alloy ingot. Mater Mech Eng 2012;11:14.
[102] Nagaumi H, Xue GX, Zhang ZZ, Ma YL. Effect of contraction behaviors during solidification of 7xxx aluminum alloys on hot tearing susceptibility. Mater Sci Forum 2014;783–786:300–6.
[103] Li S, Sadayappan K, Apelian D. Effects of mold temperature and pouring temperature on the hot tearing of cast Al-Cu alloys. Metall Mater Trans B 2016;47:2979–90.
[104] Li Y. Effect of alloying elements on microstructure and hot tearing susceptibility in direct-chill casting of 7xxx aluminum alloys. Beijing: University of Science and Technology Beijing; 2019.
[105] Cao G, Kou S. Hot tearing of ternary Mg− Al− Ca alloy castings. Metall Mater Trans A 2006;37:3647–63.
[106] Song J, Wang Z, Huang Y, Srinivasan A, Beckmann F, Kainer KU, et al. Effect of Zn addition on hot tearing behaviour of Mg–0.5Ca–xZn alloys. Mater Des 2015;87:157–70.
[107] Nagaumi H, Umeda T. Prediction of internal cracking in a direct-chill cast, high strength, Al–Mg–Si alloy. J Light Met 2002;2:161–7.
[108] Nagaumi H, Suzuki S, Okane T, Umeda T. Effect of iron content on hot tearing of high-strength Al-Mg-Si alloy. Mater Trans 2006;47:2821–7.
[109] Easton M, Davidson C, St John D. Effect of alloy composition on the dendrite arm spacing of multicomponent aluminum alloys. Metall Mater Trans A 2010;41:1528–38.
[110] Suyitno Savran VI, Katgerman L, Eskin DG. Effects of alloy composition and casting speed on structure formation and hot tearing during direct-chill casting of Al-Cu alloys. Metall Mater Trans A 2004;35:3551–61.
[111] Bai QL, Liu JC, Li HX, Du Q, Katgerman L, Zhang JS, et al. A modified hot tearing criterion for direct chill casting of aluminium alloys. Mater Sci Technol 2016;32:846–54.
[112] Ju Y, Arnberg L. Measurement of grain bridging in some Al-Cu and Al-Sn alloys. Int J Cast Met Res 2003;16:522–30.
[113] Mathier V, Grasso P-D, Rappaz M. A new tensile test for aluminum alloys in the mushy state: experimental method and numerical modeling. Metall Mater Trans A 2008;39:1399–409.
[114] Spittle J, Cushway A. Influences of superheat and grain structure on hot-tearing susceptibilities of AI-Cu alloy castings. Metals Technology 1983;10:6–13.
[115] Li R, Wang M, Li Z, Cao P, Yuan T, Zhu H. Developing a high-strength Al-Mg-Si-Sc-Zr alloy for selective laser melting: crack-inhibiting and multiple strengthening mechanisms. Acta Mater 2020;193:83–98.
[116] Montero-Sistiaga ML, Mertens R, Vrancken B, Wang X, Van Hooreweder B, Kruth J-P, et al. Changing the alloy composition of Al7075 for better processability by selective laser melting. J Mater Process Technol 2016;238:437–45.
[117] Nadella R, Eskin DG, Katgerman L. Role of grain refining in hot cracking and macrosegregation in direct chill cast AA 7075 billets. Mater Sci Technol 2007;23:1327–35.
[118] Martin JH, Yahata BD, Hundley JM, Mayer JA, Schaedler TA, Pollock TM. 3D printing of high-strength aluminium alloys. Nature 2017;549:365–9.
[119] Zhou L, Pan H, Hyer H, Park S, Bai Y, McWilliams B, et al. Microstructure and tensile property of a novel AlZnMgScZr alloy additively manufactured by gas atomization and laser powder bed fusion. Scripta Mater 2019;158:24–8.
[120] Spierings AB, Dawson K, Voegtlin M, Palm F, Uggowitzer PJ. Microstructure and mechanical properties of as-processed scandium-modified aluminium using selective laser melting. CIRP Ann 2016;65:213–6.
[121] Jia Q, Rometsch P, Cao S, Zhang K, Wu X. Towards a high strength aluminium alloy development methodology for selective laser melting. Mater Des 2019;174:107775.
[122] Nie X, Zhang H, Zhu H, Hu Z, Ke L, Zeng X. Effect of Zr content on formability, microstructure and mechanical properties of selective laser melted Zr modified Al-4.24Cu-1.97Mg-0.56Mn alloys. J Alloys Compd 2018;764:977–86.
[123] Tan Q, Zhang J, Sun Q, Fan Z, Li G, Yin Y, et al. Inoculation treatment of an additively manufactured 2024 aluminium alloy with titanium nanoparticles. Acta Mater 2020;196:1–16.
[124] Oliveira JP, Santos TG, Miranda RM. Revisiting fundamental welding concepts to improve additive manufacturing: From theory to practice. Prog Mater Sci 2020;107:100590.
[125] Easton M, Grandfield JF, StJohn DH, Rinderer B. The effect of grain refinement and cooling rate on the hot tearing of wrought aluminium alloys. Mater Sci Forum 2006;519–521:1675–80.
[126] Greer A. Overview: Application of heterogeneous nucleation in grain-refining of metals. J Chem Phys 2016;145:211704.
[127] Easton MA, Qian M, Prasad A, StJohn DH. Recent advances in grain refinement of light metals and alloys. Curr Opin Solid State Mater Sci 2016;20:13–24.
[128] Du Q, Li Y. An extension of the Kampmann-Wagner numerical model towards as-cast grain size prediction of multicomponent aluminum alloys. Acta Mater 2014;71:380–9.
[129] Li YJ, Arnberg L. Solidification structures and phase selection of iron-bearing eutectic particles in a DC-cast AA5182 alloy. Acta Mater 2004;52:2673–81.
[130] Moriceau J. Thermal stresses in continuous DC casting of Al alloys discussion of hot tearing mechanisms. In: Essential readings in light metals. Springer International Publishing; 2016. p. 854–61.
[131] Commet B, Delaire P, Rabenberg J, Storm J. Measurement of the onset of hot cracking in DC cast billets. In: Grandfield JF, Eskin DG, editors. Essential readings in light metals: Volume 3 cast shop for aluminum production. Cham: Springer International Publishing; 2016. p. 900–6.
[132] Jamaly N, Phillion AB, Drezet J-M. Stress–strain predictions of semisolid Al-Mg-Mn alloys during direct chill casting: effects of microstructure and process variables. Metall Mater Trans B 2013;44:1287–95.
[133] Eskin DG, Savran VI, Katgerman L. Effects of melt temperature and casting speed on the structure and defect formation during direct-chill casting of an Al-Cu alloy. Metall Mater Trans A 2005;36:1965–76.
[134] Caron E, Wells MA. Film boiling and water film ejection in the secondary cooling zone of the direct-chill casting process. Metall Mater Trans B 2012;43:155–62.
[135] Sengupta JTB, Wells MA. The use of water cooling during the continuous casting of steel and aluminum alloys. Metall Mater Trans A 2005;36:187–204.
[136] Caron E, Wells MA. Secondary cooling in the direct-chill casting of magnesium alloy AZ31. Metall Mater Trans B 2009;40:585–95.
[137] Eskin DG, Zuidema J, Savran VI, Katgerman L. Structure formation and macrosegregation under different process conditions during DC casting. Mater Sci Eng, A 2004;384:232–44.
[138] Eskin GI, Eskin DG. Ultrasonic treatment of light alloy melts. London: CRC Press; 2014.
[139] Eskin DG. Ultrasonic processing of molten and solidifying aluminium alloys: overview and outlook. Mater Sci Technol 2017;33:636–45.
[140] Dong J, Zhao Z, Cui J, Yu F, Ban C. Effect of low-frequency electromagnetic casting on the castability, microstructure, and tensile properties of direct-chill cast Al-Zn-Mg-Cu alloy. Metall Mater Trans A 2004;35:2487–94.
[141] Zuo Y, Nagaumi H, Cui J. Study on the sump and temperature field during low frequency electromagnetic casting a superhigh strength Al–Zn–Mg–Cu alloy. J Mater Process Technol 2008;197:109–15.
[142] Zuo Y, Cui J, Zhao Z, Zhang H, Qin K. Effect of low frequency electromagnetic field on casting crack during DC casting superhigh strength aluminum alloy ingots. Mater Sci Eng, A 2005;406:286–92.
[143] Suyitno Kool WH, Katgerman L. Finite element method simulation of mushy zone behavior during direct-chill casting of an Al-4.5 pct Cu alloy. Metall Mater Trans A 2004;35:2917–26.
[144] Suyitno Kool W, Katgerman L. Integrated approach for prediction of hot tearing. Metall Mater Trans A 2009;40:2388–400.
[145] Suyitno Kool W, Katgerman L. Hot tearing criteria evaluation for direct-chill casting of an Al-4.5 pct Cu alloy. Metall Mater Trans A 2005;36:1537–46.
[146] Eskin DG, Katgerman L. Thermal contraction of AA5182 for prediction of ingot distortions. Key Eng Mater 2006;306:977–82.
[147] Mihanyar S, Mo A, M'Hamdi M, Ellingsen K. Modeling of de-cohesion and the initiation of hot tearing in coherent mushy zones of metallic alloys. Metall Mater Trans A 2011;42:1887–95.

[148] Sistaninia M, Phillion AB, Drezet J-M, Rappaz M. Simulation of semi-solid material mechanical behavior using a combined discrete/finite element method. Metall Mater Trans A 2011;42:239–48.
[149] Sistaninia M, Phillion AB, Drezet JM, Rappaz M. A 3-D coupled hydromechanical granular model for simulating the constitutive behavior of metallic alloys during solidification. Acta Mater 2012;60:6793–803.
[150] M'Hamdi M, Mo A, Fjær HG. TearSim: a two-phase model addressing hot tearing formation during aluminum direct chill casting. Metall Mater Trans A 2006;37:3069–83.
[151] Lalpoor M. Study of cold cracking during DC-casting of high strength aluminum alloys. Netherlands: Delft University of Technology; 2010.
[152] Phillion AB, Cockcroft SL, Lee PD. A three-phase simulation of the effect of microstructural features on semi-solid tensile deformation. Acta Mater 2008;56:4328–38.
[153] M'hamdi M, Benum S, Mortensen D, Fjaer H, Drezet J-M. The importance of viscoplastic strain rate in the formation of center cracks during the start-up phase of direct-chill cast aluminum extrusion ingots. Metall Mater Trans A. 2003;34:1941–52.
[154] Du Q, Eskin DG, Katgerman L. The effect of ramping casting speed and casting temperature on temperature distribution and melt flow patterns in the sump of a DC cast billet. Mater Sci Eng, A 2005;413–414:144–50.
[155] Du Q, Li Y. Prediction of as-cast grain size of inoculated aluminum alloys melt solidified under non-isothermal conditions. In: IOP conference series: materials science and engineering. IOP Publishing; 2015. p. 012015.
[156] Fujii S, Yokoi T, Fisher CA, Moriwake H, Yoshiya M. Quantitative prediction of grain boundary thermal conductivities from local atomic environments. Nat Commun 2020;11:1–10.
[157] Bapst V, Keck T, Grabska-Barwińska A, Donner C, Cubuk ED, Schoenholz S, et al. Unveiling the predictive power of static structure in glassy systems. Nat Phys 2020;16:448–54.
[158] Kou S. A criterion for cracking during solidification. Acta Mater 2015;88:366–74.
[159] Liu J, Kou S. Crack susceptibility of binary aluminum alloys during solidification. Acta Mater 2016;110:84–94.
[160] Liu J, Duarte HP, Kou S. Evidence of back diffusion reducing cracking during solidification. Acta Mater 2017;122:47–59.
[161] Drezet J-M, Rappaz M. Prediction of hot tears in DC-cast aluminum billets. In: Essential readings in light metals. Cham: Springer; 2016. p. 912–8.
[162] Liu J, Kou S. Susceptibility of ternary aluminum alloys to cracking during solidification. Acta Mater 2017;125:513–23.
[163] Kou S. A simple index for predicting the susceptibility to solidification cracking. Welding J 2015;94:374s–88s.
[164] Han J, Wang J, Zhang M, Niu K. Susceptibility of lithium containing aluminum alloys to cracking during solidification. Materialia 2018;5:100203.
[165] Liu K, Kou S. Susceptibility of magnesium alloys to solidification cracking. Sci Technol Weld Joining 2020;25:251–7.
[166] Sistaninia M, Phillion AB, Drezet JM, Rappaz M. Three-dimensional granular model of semi-solid metallic alloys undergoing solidification: fluid flow and localization of feeding. Acta Mater 2012;60:3902–11.
[167] Sistaninia M, Terzi S, Phillion AB, Drezet JM, Rappaz M. 3-D granular modeling and in situ X-ray tomographic imaging: a comparative study of hot tearing formation and semi-solid deformation in Al–Cu alloys. Acta Mater 2013;61:3831–41.
[168] Vernède S, Jarry P, Rappaz M. A granular model of equiaxed mushy zones: Formation of a coherent solid and localization of feeding. Acta Mater 2006;54:4023–34.
[169] Zareie Rajani HR, Phillion AB. 3D multi-scale multi-physics modelling of hot cracking in welding. Mater Des 2018;144:45–54.
[170] Sistaninia M, Drezet J-M, Phillion AB, Rappaz M. Prediction of hot tear formation in vertical DC casting of aluminum billets using a granular approach. JOM 2013;65:1131–7.
[171] Rappaz M. Modeling and characterization of grain structures and defects in solidification. Curr Opin Solid State Mater Sci 2016;20:37–45.
[172] Nguyen VP, Lloberas-Valls O, Stroeven M, Sluys LJ. Homogenization-based multiscale crack modelling: from micro-diffusive damage to macro-cracks. Comput Methods Appl Mech Eng 2011;200:1220–36.
[173] Talebi H, Silani M, Bordas SPA, Kerfriden P, Rabczuk T. A computational library for multiscale modeling of material failure. Comput Mech 2014;53:1047–71.
[174] Hun D-A, Guilleminot J, Yvonnet J, Bornert M. Stochastic multiscale modeling of crack propagation in random heterogeneous media. Int J Numer Meth Eng 2019;119:1325–44.
[175] Hsu Y-C, Yu C-H, Buehler MJ. Using deep learning to predict fracture patterns in crystalline solids. Matter 2020.
[176] Saito Y, Tanaka S-I. Internal crack propagation in a continuously cast austenitic stainless steel analyzed by actual residual stress tensor distributions. Metall Mater Trans B 2016;47:882–90.
[177] Wu S, Kondo Y, Kakimoto M-a, Yang B, Yamada H, Kuwajima I, et al. Machine-learning-assisted discovery of polymers with high thermal conductivity using a molecular design algorithm. npj Comput Mater 2019;5:1–11.
[178] Yamada H, Liu C, Wu S, Koyama Y, Ju S, Shiomi J, et al. Predicting materials properties with little data using shotgun transfer learning. ACS Cent Sci 2019;5:1717–30.
[179] Raissi M, Yazdani A, Karniadakis GE. Hidden fluid mechanics: learning velocity and pressure fields from flow visualizations. Science 2020;367:1026–30.
[180] Wu C, Marchese M, Wang Y, Krapivin M, Wang C, Li X, et al. Data preprocessing in SVM-based keywords extraction from scientific documents. In: Fourth International Conference on Innovative Computing, Information and Control (ICICIC), 2009. IEEE; 2009. p. 810–3.
[181] Shen J, Hao X, Liang Z, Liu Y, Wang W, Shao L. Real-time superpixel segmentation by DBSCAN clustering algorithm. IEEE Trans Image Process 2016;25:5933–42.
[182] Granik M, Mesyura V. Fake news detection using naive Bayes classifier. In: 2017 IEEE First Ukraine Conference on Electrical and Computer Engineering (UKRCON). IEEE; 2017. p. 900–3.
[183] Eriksson TA, Bülow H, Leven A. Applying neural networks in optical communication systems: possible pitfalls. IEEE Photonics Technol Lett 2017;29:2091–4.
[184] Chang X, Lin S-B, Zhou D-X. Distributed semi-supervised learning with kernel ridge regression. J Mach Learn Res 2017;18:1493–514.
[185] Chen W, Xie X, Peng J, Wang J, Duan Z, Hong H. GIS-based landslide susceptibility modelling: a comparative assessment of kernel logistic regression, Naïve-Bayes tree, and alternating decision tree models. Geomat Nat Haz Risk 2017;8:950–73.
[186] Santamaría-Bonfil G, Reyes-Ballesteros A, Gershenson C. Wind speed forecasting for wind farms: a method based on support vector regression. Renew Energy 2016;85:790–809.
[187] Liu Y, Zhao T, Ju W, Shi S. Materials discovery and design using machine learning. JMAT 2017;3:159–77.
[188] Feng S, Dong HB. Predicting solidification cracking susceptibility of stainless steels using machine learning. IOP Conf Series: Mater Sci Eng 2020;861:012073.
[189] Suyitno. Hot tearing and deformation in direct-chill casting of aluminum alloys. Netherland: Delft University of Technology; 2005.
[190] Drezet J-M, Chobaut N, Drakopoulos M, Pirling T. Hot tearing: after the Rappaz-Drezet-Gremaud criterion, where are we? TMS 2016 145th annual meeting. Nashville, Tennessee; 2016. p. 215–20.